SAPIENZA
UNIVERSITÀ DI ROMA

Sapienza University of Rome

Physics Department
PhD in Accelerator Physics

Thesis For The Degree Of Doctor Of Philosophy

Beam dynamics studies for advanced - compact RF photoinjector for PWFA

Advisor
Prof.ssa Enrica Chiadroni
Prof. Andrea Mostacci

Correlatore
Dott.ssa Anna Giribono

Candidate
Gilles Jacopo Silvi
1705959

Academic Year 2023-2024 (XXXVII cycle)

Ai miei genitori

Abstract

Advanced high-brightness RF photoinjectors play a crucial role in generating high peak current and low transverse emittance electron beams, which are essential for driving Plasma Wakefield Acceleration (PWFA) stages. The thesis work focused on the study of electron beam dynamics for advanced injectors in PWFA-driven applications. The main activity involved optimizing the injector of EuPRAXIA@SPARC_LAB and conducting a feasibility study for upgrading the injector using C-band technology. Starting with a two-bunches beam, named as comb beam, comprising a 200 pC driver and a 30 pC witness, directly generated at the cathode, the dynamics was optimized to meet the output parameters required for the subsequent plasma stage. This optimization was performed using simulation codes like ASTRA and a genetic algorithm called GIOTTO. The study addressed not only the optimization of longitudinal and transverse parameters to match the plasma requirements but also the optimization of the cathode distribution for the comb-like working point. Once the comb dynamics was optimized and the injector parameter table was finalized, my thesis work focused on studying the jitter, both RF and cathode distribution, of the machine to assess its stability and reproducibility. Due to a double velocity bunching compression scheme, this type of injector is highly sensitive to radiofrequency (RF) jitter. To stabilize the injector and improve the driver and witness bunches separation, a high-harmonic cavity (X-band) was inserted between the gun and the first accelerating section. This cavity proved to be essential for improving the working point, and its use has been finalized and included in the EuPRAXIA@SPARC_LAB Technical Design Report (TDR) that is in preparation. Looking ahead to a potential upgrade of the machine to achieve higher repetition rates (400 Hz), a feasibility study on the dynamics of a full C-band injector has been conducted. In addition to the advantage of high repetition rates, C-band technology allows for higher accelerating gradients in both the gun and accelerating structures while reducing the injector's overall length. Achieving these enhancements requires the optimization of both active and passive machine elements, including laser systems, the gun solenoid, and RF components. This study focuses on the possibility of using C-band technology for such advanced applications comparing the C-band injector's performance with the state-of-the-art S-band technology. Start-to-end beam dynamics simulations have been conducted to identify the optimal configuration for a C-band photoinjector. For this configuration, the nominal working point of 200+30 pC was studied, achieving the same output parameters as the S-band injector. Considering the more modest compression phase expected for the C-band injector, this solution provides improved stability. As in the previous case, a high-harmonic cavity was included to enhance the working point stability. In this scenario, the cavity's effects on dynamics were evaluated, including improved beam separation, emittance, and the peak current of the witness beam. Regarding my thesis, I also conducted beam dynamics studies for the final focusing section before the plasma stage in the SPARC_LAB linac. The final focusing study was carried out using two different configurations: a triplet of permanent magnet quadrupoles and a triplet of electromagnetic quadrupoles. The first system was tested with a 50 pC beam (witness-like beam for the SPARC_LAB comb), while the second was tested with a comb-like working point comprising a 200 pC driver and a 50 pC witness. During a six-month visiting period at the University of California, Los Angeles, I focused on the characterization of photocathodes at the PEGASUS laboratory, with particular emphasis on yttrium which offers advantages in visible laser operation, increasing per- pulse energy and avoiding high-harmonic conversions, useful for

high-repetition-rate applications. My research also involved developing a machine learning-based analysis method for the PEGASUS photogun to reconstruct the emittance and, consequently, determine the average transverse energy of a photocathode using solenoid scan data. This technique could be implemented in future applications for non-intercepting virtual diagnostic in the low energy region for PWFA working point.

Contents

Chapter 1

Introduction and motivations

The development of particle accelerators is driven by the increasing need to produce beams with higher energy and intensity. In recent decades, advancements in accelerator technology have led to the emergence of novel acceleration schemes, such as plasma-based acceleration, which promise to revolutionize the field. This innovative technology can significantly reduce both the size and cost of accelerators by several orders of magnitude compared to traditional methods. The two leading plasma-based acceleration schemes are particle-driven wakefield acceleration (PWFA, Fig. 1.1b) and laser wakefield acceleration (LWFA, Fig. 1.1a). Both of these methods rely on creating a wave or wave-like perturbation in the plasma electron density, initiated by either a laser pulse or a particle beam. The electric field generated in the wake of this perturbation can be harnessed for particle acceleration. In beam-driven acceleration, also known as PWFA, the wave is excited by the space charge forces following a high-energy particle beam. This process involves a dense beam of charged particles, known as the "driver", which travels through a plasma, creating a wake of electric fields strong enough to accelerate a trailing "witness" beam of particles to high energies. On the other hand, in laser wakefield acceleration (LWFA), a plasma wave is excited by the radiation pressure of a high-intensity laser pulse. As the laser pulse passes through the plasma, it drives a strong oscillation in the plasma electrons, forming a wake of electric fields. These fields can accelerate charged particles to high energies over very short distances, offering a compact and efficient alternative to conventional accelerators. Both PWFA and LWFA hold great promise for future applications in scientific research, medical technologies, and industrial processes. By offering the potential for compact and cost-effective accelerators, these technologies could enable a new generation of experiments and applications that were previously unattainable with conventional accelerator technology. In PWFA, the particle beams injected into the plasma stage are generated by a conventional RF linac driven by a photoinjector: ultrashort (few tens of fs), low emittance ($\approx$ mm-mrad), small energy spread($\approx \ll \%$) beams, i.e high brightness beams, are produced and sent to the plasma stage. These accelerators produce beams that are very short, with low emittance and energy spread, which translates to high brightness at the plasma entrance [1]. High-brightness photoinjectors serve as the electron sources for such advanced accelerators. This thesis explores the potential of RF photoinjectors to generate high-quality electron beams tailored to meet the stringent requirements of plasma applications. It will cover various aspects of beam generation, starting from the initial cathode generation, through the manipulation of the beam, and culminating in the final acceleration stages. Each phase of the process will be explored in detail to understand how these techniques

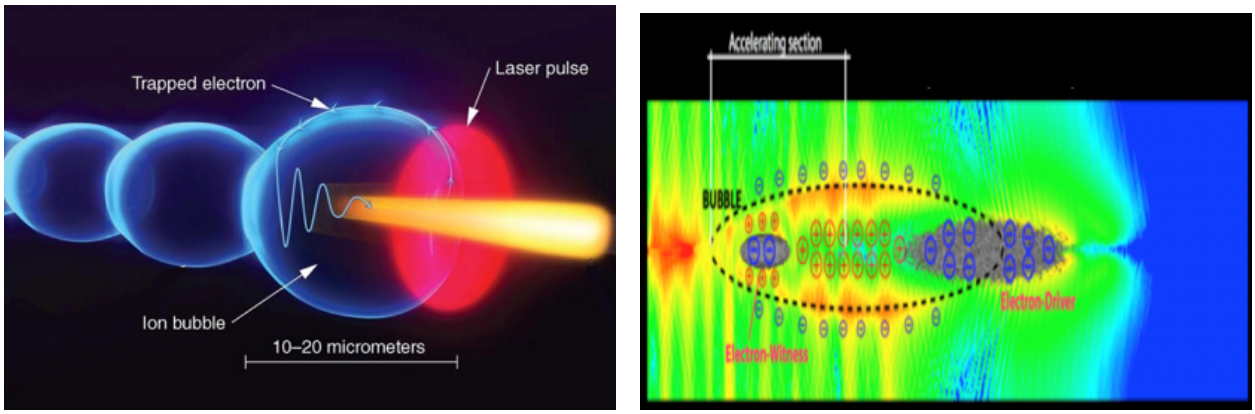

(a) Laser wakefield acceleration scheme **(b)** Particle driven wakefield acceleration scheme

Figure 1.1: Plasma acceleration schemes: (a)LWFA (b) PWFA.

contribute to achieving the desired beam qualities for PWFA applications. The focus will be on the operations to be performed and the beam dynamics simulation tools to be used to operate in high-bright conditions. In Chapter 2 I will describe the main component of an RF photoinjector and the main figure of merit; Chapters 3-5 describe the study I have performed in the framework of the project SPARC_LAB [2], EuPRAXIA@SPARC_LAB[3][4] and PEGASUS [5], where these techniques have been applied. Starting with the theory behind each application, step by step I will build a reproducible operational model for obtaining high-brightness electron beams. The discussion will also focus on how the various components of the injector interact on the electron beam and how the individual component can be optimized to achieve the desired beam parameters. Start-to-end beam dynamics simulations were conducted to optimize not only the beam line parameters but also the beam distribution at the cathode to obtain the parameters of interest for the applications that were covered during the PhD activities. Each application of high-brightness beams needs optimizations in terms of beamline elements and the electron beam itself is entirely different. Here I am going to define and delve into what are the techniques to produce, manipulate and optimize high-brightness electron beams for PWFA applications. Compact accelerators are transformative tools that hold the potential to revolutionize both scientific exploration and societal well-being. These groundbreaking devices, by their reduced size and cost, democratize access to advanced particle acceleration technologies, enabling institutions and regions previously excluded from such capabilities to contribute to and benefit from cutting-edge research and applications. A key innovation in this field is the transition in RF photoinjector technology from the state of the art S-band systems to higher-frequency C-band systems. RF photoinjectors, which are essential for generating high-brightness electron beams, have traditionally operated in the S-band range (3 GHz). While reliable and widely used, S-band systems are limited by their size and lower achievable accelerating gradients. The shift to C-band (6 GHz) and X-band (12 GHz) technologies represents a transformative step forward, enabling higher accelerating gradients—on the order of 40-60 MV/m—and significantly smaller structures. This transition is driven by the increasing demand for compact, high-performance accelerators in applications ranging from free-electron lasers (FELs) to ultrafast electron diffraction and medical imaging. Adopting C-band technology offers several key advantages in the context of RF photoinjectors. The smaller sizes inherent to higher-frequency systems reduce the overall dimensions of the injector, making it more compact and easier to integrate into laboratory-scale setups. Additionally,

the higher accelerating gradients achievable with the C-band system enable the production of high-brightness, low-emittance electron beams over shorter distances, which is critical for downstream applications requiring ultrashort electron bunches and precise beam dynamics. These advancements are particularly valuable in driving the performance of compact FELs, table-top ultrafast electron diffraction systems, and emerging plasma acceleration schemes. From a scientific perspective, these high-frequency RF photoinjectors unlock new possibilities for probing matter with unprecedented precision. Their ability to generate ultrashort, high-energy electron pulses enables time-resolved studies of dynamic processes at atomic and molecular scales, pushing the boundaries of ultrafast science and materials research. The societal impact of compact accelerators equipped with advanced RF photoinjectors is equally profound. In industrial applications, these systems support advanced material characterization and non-destructive testing, driving innovation in the aerospace, manufacturing, and energy sectors. Furthermore, compact accelerators with high-brightness beams play a crucial role in environmental monitoring and security, enabling technologies such as real-time imaging of hazardous materials and radiation detection. The transition from S-band to C-band RF photoinjector exemplifies how cutting-edge RF technology is reshaping the landscape of compact accelerators. By achieving higher performance in smaller, more efficient systems, this innovation bridges the gap between large-scale accelerator facilities and practical, deployable solutions. This paradigm shift not only empowers scientists and engineers with advanced tools for discovery and innovation but also expands the societal reach of accelerator technologies, fostering a future where high-impact applications are accessible to a broader global community.

Chapter 2

Electron source figure of merit

The brightness is the meaningful figure of merit of an electron beam. Brightness is a critical parameter in electron beam physics and various applications that rely on electron beams, such as electron microscopy, particle accelerators, and free-electron lasers. It quantifies how efficiently the beam's current is concentrated into a small area, providing insight into its spatial quality and intensity. In the study of electron beams, understanding how brightness and envelope dynamics interact is crucial for optimizing beam performance. The 5D electron beam brightness B is defined as:

$$B \propto \frac{I}{\epsilon_{nx}\epsilon_{ny}} \tag{2.1}$$

where I is the beam peak current, and ϵ_{nx} and ϵ_{ny} are the normalized transverse emittances in the x and y directions, respectively. The normalized transverse emittance ϵ_n is given by:

$$\epsilon_n = \epsilon_g \gamma \beta \tag{2.2}$$

where ϵ_g is the geometric emittance, γ is the Lorentz factor:

$$\gamma = \frac{1}{\sqrt{1 - \frac{v^2}{c^2}}} \tag{2.3}$$

and β is the normalized velocity :

$$\beta = \frac{v}{c} \tag{2.4}$$

The geometric emittance ϵ_g describes the beam's spatial and angular spreads:

$$\epsilon_g = \sqrt{\langle x^2 \rangle \langle x'^2 \rangle - \langle x x' \rangle^2} \tag{2.5}$$

In the six-dimensional phase space, emittance ϵ is defined as the area of the ellipse that contains all the particles. In the presence of linear forces, this emittance is conserved according to Liouville's theorem. The quantity we measure, however, is the geometrical emittance ϵ_g, which is the area of the ellipse in the trace space (x, x'). Analogous to Liouville's theorem, the geometrical emittance of a beam is conserved under Hamiltonian dynamics. For a monochromatic beam, this conservation is more easily maintained as chromatic effects are absent. The shape of the area in trace space can

be distorted by non-linear fields in the lattice. Thus, the RMS emittance ϵ_{RMS} is introduced:

$$\epsilon_{\text{RMS}}^2 = \langle x^2 \rangle \langle x'^2 \rangle - \langle x x' \rangle^2 \tag{2.6}$$

When the beam is subject to acceleration, it is more convenient to use the normalized RMS emittance ϵ_n, which incorporates the transverse momentum $p_x = p_z x' = m_0 c \beta \gamma x'$ instead of the divergence:

$$\epsilon_n^2 = \langle x^2 \rangle \langle \beta^2 \gamma^2 x'^2 \rangle - \langle x x' \beta \gamma \rangle^2 \tag{2.7}$$

where β and γ are relativistic factors. The introduction of normalized emittance is useful because divergences of particles $x' = p_x/p$ are reduced during acceleration as p_z increases. Consequently, while acceleration reduces the un-normalized emittance, it does not affect the normalized emittance. For non-monochromatic beams, in the absence of correlation between energy and transverse position, the formula can be written as follows:

$$\epsilon^2 = \langle \gamma^2 \rangle \sigma_e^2 \langle x^2 \rangle \langle x'^2 \rangle - \langle \beta \gamma \rangle^2 (\langle x^2 \rangle \langle x'^2 \rangle - \langle x x' \rangle) \tag{2.8}$$

where σ_e, the variation or distribution of the kinetic energies of the particles within the beam, is the energy spread factor. For a small energy spread within the beam, the normalized emittance is approximately $\epsilon_n = \beta \gamma \epsilon_{\text{RMS}}$ [6]. The beam's transverse size or envelope radius ρ evolution along the beamline is described by envelope equation. For a beam passing through a focusing system, the envelope equation is:

$$\frac{d^2 \rho}{dz^2} = \frac{K}{\rho} - \rho \frac{\beta}{\gamma} \tag{2.9}$$

where K is the focusing strength of the beamline elements, and ρ is the beam envelope radius. The Twiss parameters α_T, β_T, and γ_T are related to the beam's focusing and phase space distribution:

- $\beta_T(z)$: Describes the beam's transverse size and changes along the beamline.
- $\alpha_T(z)$: Represents the correlation between transverse position and angle.
- $\gamma_T(z)$: Related to the beam's emittance and focusing strength:

$$\gamma_T = \frac{1 + \alpha_T^2}{\beta_T}$$

The normalized emittance ϵ_n can be expressed as:

$$\epsilon_n = \beta_T \rho \sqrt{1 + \alpha_T^2} \tag{2.10}$$

To understand the relationship between emittance and brightness, we need to introduce the envelope equation. The envelope equation provides the beam's transverse size ρ, which directly impacts the beam's normalized emittance. Since the normalized emittance is related to the beam envelope by equation (2.10) and the brightness is defined as equation (2.1). We can see that a smaller ρ (indicating better focusing) results in lower emittance and higher brightness, assuming the current I remains constant. Thus, optimizing the beamline design to achieve desired β_T, α_T, and γ_T values through appropriate focusing and alignment helps in minimizing emittance. This, in turn, enhances

the beam's brightness, which is critical for high-performance accelerators, and other applications requiring precise control over electron beams. The integration of brightness and envelope equations highlights the importance of managing beam size and focusing to optimize beam performance. Understanding and controlling these factors allow for high brightness, essential for various scientific and industrial applications. Brightness optimization involves several strategies to enhance the performance of an electron beam. Minimizing emittance starts with improving the quality of the electron source, which directly impacts the emittance. Additionally, emittance exchange techniques, which involve altering beam parameters with specialized optics, can further reduce emittance. Maximizing current is essential but must be balanced with managing space charge effects to maintain high brightness. The design of focusing elements plays a critical role in improving brightness, as does optimizing beamline parameters to achieve ideal values for the Twiss parameters β and α. Managing beam dynamics includes employing techniques to control instabilities and ensure the beam remains focused and bright. Practically, high brightness is crucial for particle accelerators applications, where it enables high-performance experiments. Brightness is measured using diagnostics that evaluate both current and emittance, ensuring that the beam meets the required specifications for its intended use. Brightness can be improved by increasing the peak current, shortening the electron bunch length thanks to sophisticated compression configurations. The peak current of an electron beam, I_{peak}, is related to the total bunch charge Q, the bunch length σ_z, and the speed of light c.

$$I_{\text{peak}} = \frac{Q}{\sqrt{2\pi}\sigma_z/c}, \tag{2.11}$$

The RF photoinjector is capable of producing high-quality electron beams for advanced scientific applications.

2.1 RF photoinjectors

An RF photoinjector is a sophisticated device used to generate high-brightness electron beams for applications like FELs)[7][8], UED[9], plasma acceleration [10] and linear colliders. It consists of a laser-generated electron source followed by an electron beam optical system which preserves and matches the beam into a high-energy accelerator. A typical photoinjector consists of an RF gun, embedded with a photocathode and an emittance compensation solenoid, followed by accelerating structures (or booster linac). The beam is generated in the gun and boosted at the desired energy through the downstream booster linac. The main components of such a machine are: The laser system, a crucial component of the photoinjector, is responsible for generating the initial electron beam through the process of photoemission. The laser's characteristics, such as wavelength, pulse duration, and energy, directly impact the quality and performance of the electron beam produced. The primary purpose of the laser system in a photoinjector is to illuminate the photocathode, causing the emission of electrons via the photoelectric effect. The emitted electrons are then accelerated by the RF fields in the RF gun, forming the initial electron bunches that are subsequently injected into the accelerator. Key parameters of the laser system include:

1. **Wavelength**: The laser's wavelength must match the photocathode material's work function to efficiently generate electrons. Common wavelengths range from ultraviolet (UV) to visible light, depending on the photocathode material.

2. **Pulse Duration**: The duration of the laser pulses determines the initial temporal structure of the electron bunches. Shorter pulses generally lead to shorter electron bunches, which are desirable for applications requiring high temporal resolution.

3. **Energy and Power**: The laser pulse energy must be sufficient to produce the required number of electrons, while avoiding damage to the photocathode. Additionally, the power must be stable to ensure consistent electron beam generation.

The laser pulses must be synchronized with the RF fields in the photoinjector to ensure that the emitted electrons are captured and accelerated at the correct phase. This synchronization is critical for minimizing the energy spread and optimizing the beam's longitudinal properties. The spatial and temporal quality of the laser beam directly affects the resulting electron beam quality. Techniques such as pulse shaping and beam homogenization are employed to produce a uniform and well-defined laser spot on the photocathode. These techniques help in minimizing the emittance and improving the overall beam quality. In an RF injector, the photocathode is illuminated by a laser pulse, leading to the emission of electrons via the photoelectric effect. These emitted electrons are then captured and accelerated by the RF fields present in the injector, forming the initial electron bunches that are subsequently accelerated in the linac. The efficiency of this electron emission process depends on the photocathode material properties and the laser characteristics. The selection of the photocathode material is crucial and depends on factors such as quantum efficiency (QE), response time, and robustness. Common photocathode materials include:

1. **Metallic Photocathodes**: Metals like copper and magnesium are commonly used due to their durability and relatively low work function $\phi_w = 4.6eV$. However, they typically have lower QE, in the order of 10^{-4}-10^{-1} with respect to semiconductor or alkaline-based, requiring more powerful laser systems to generate sufficient electron beams. The response time for Cu and Mg cathodes is less than picoseconds. Therefore, metal photocathodes are often used for accelerator applications where only low average current and a fast response time is required, [11].

2. **Semiconductor Photocathodes**: Materials like cesium telluride (Cs_2Te) and gallium arsenide (GaAs) offer higher QE, 10%, allowing for efficient electron emission with lower laser power. These materials are more sensitive to contamination and require ultra-high vacuum conditions to maintain their performance.

3. **Alkali-based Photocathodes**: Alkali metals such as potassium, cesium, and sodium are used in photocathodes to achieve very high QE (4-15% @532 nm), especially in the ultraviolet (UV) range. These materials, while efficient, are highly reactive and require careful handling and vacuum conditions.

4. **Yttrium**: Yttrium is a transition metal that has a work function of $\phi_w \approx 3eV$, that permits to use visible laser pulses increasing energy per pulse that enables high repetition rate applications. Also, we avoid high harmonic conversion simplifying the system

Photoelectric emission from a metal can be effectively described using the Spicer model [12] (Fig 2.1). This model divides the emission process into three main steps: photon absorption, electron

transport to the surface, and escape through the barrier. Inside the cathode, the distribution of occupied energy levels is given by the Fermi-Dirac distribution. Near the cathode, the forces on

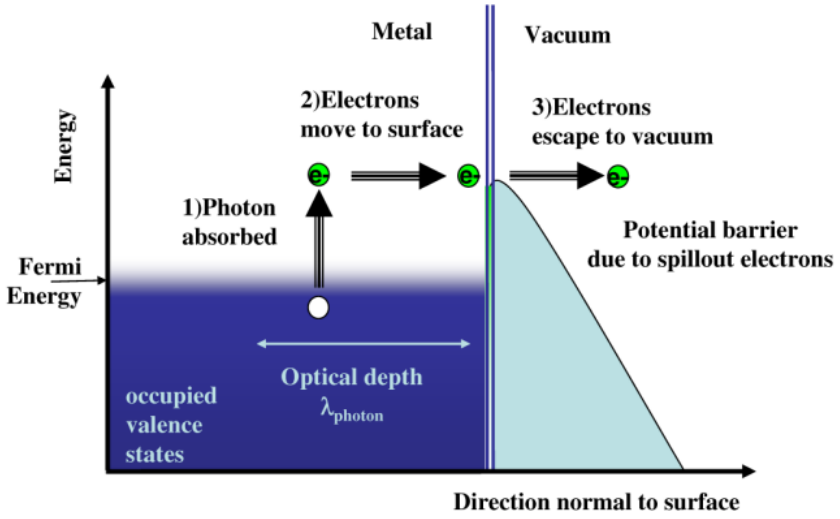

Figure 2.1: Three-step model. This model divides the emission process into three main steps: photon absorption, electron transport to the surface, and escape through the barrier. [13].

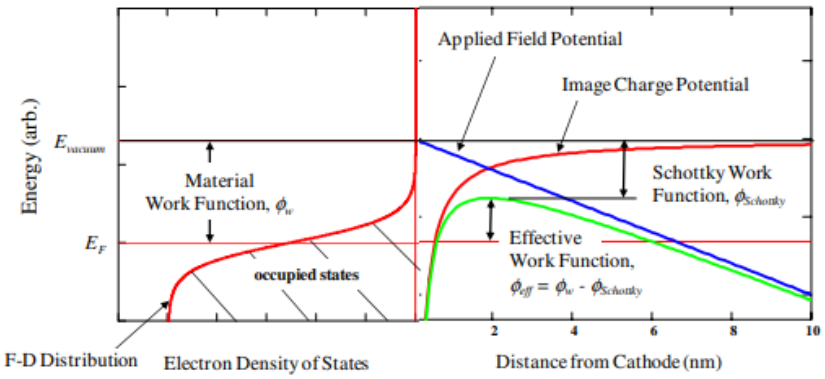

Figure 2.2: Electron potentials at the cathode [13]; the material's work function, the image potential due to the electron's opposite image on the metallic surface, and the external RF field.

an electron arise from three potentials: the material's work function, the image potential due to the electron's opposite image on the metallic surface, and the external RF field (Fig 2.2). The sum of the image and applied potentials forms a potential barrier that reduces the material's work function by the Schottky work function. When external forces are present, the effective work function is defined as the energy needed for an electron to escape from the material:

$$\phi_{eff} = \phi - \phi_{Schottky} \tag{2.12}$$

Photoemission is regarded as a quantum mechanical effect, but electrons do not tunnel through the barrier; they escape over it classically. An electron excited by a photon with energy $\hbar\omega$ loses energy by scattering. Assuming electron-electron scattering dominates, F_{e-e} is the probability that

an electron absorbing a photon escapes without scattering:

$$F_{e-e} = \int_0^\infty f(s)\, ds = \frac{1}{1 + \frac{\lambda_{\text{opt}}}{\lambda_{e-e}}} \tag{2.13}$$

where λ_{e-e} is the electron-electron scattering length and λ_{opt} is the optical skin depth. For the escape criterion, Fig 2.3:

$$p_{\text{tot}} = \sqrt{2m\,(E + \hbar\omega)} \tag{2.14}$$

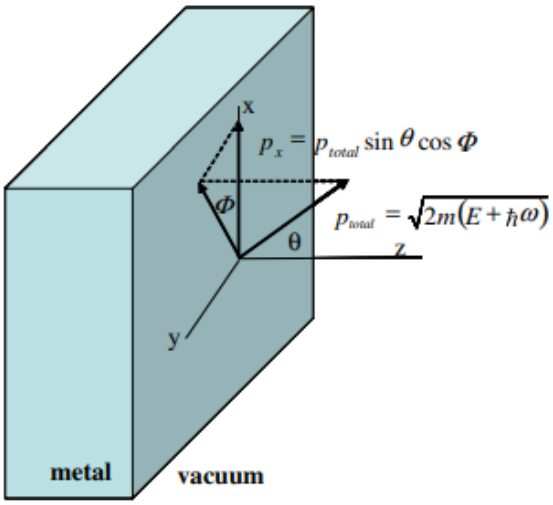

Figure 2.3: Graphical explanation of the escape criterion from a metal surface[13]

$$p_{normal} = \cos(\theta)\sqrt{2m(E + \hbar\omega)} \tag{2.15}$$

$$\frac{p_{normal}^2}{2m} > E_f + \phi_{eff} \tag{2.16}$$

$$\cos\theta = \frac{p_{normal}}{p_{tot}} = \frac{E_f + \phi_{eff}}{E + \hbar\omega} \tag{2.17}$$

According to the Spicer model [13], the cathode's QE can be represented mathematically as:

$$QE = \frac{(1 - R(\omega)) \left[\int_{E_f + \phi_{\text{eff}} - \hbar\omega}^{\infty} dE\, N(E + \hbar\omega) \left(1 - f_{\text{FD}}(E + \hbar\omega)\right) N(E) f_{\text{FD}}\right] \left[\int_1^{\cos\theta \max(E)} d(\cos\theta)\, F_{e-e}(E, \omega, \theta) \int_0^{2\pi} d\phi\right]}{\left[\int_{E_f}^{\infty} dE\, N(E + \hbar\omega) \left(1 - f_{\text{FD}}(E + \hbar\omega)\right) N(E) f_{\text{FD}}\right] \left[\int_1^0 d(\cos\theta) \int_0^{2\pi} d\phi\right]} \tag{2.18}$$

The cathode optical reflectivity is given by $R(\omega)$. The Fermi-Dirac function, $f_{\text{FD}}(E)$, represents the density of initial states, while $[1 - f_{\text{FD}}(E + \hbar\omega)]$ represents the density of final states. The product of these two functions determines the transition probability for an excited electron to escape. The probability that an excited electron reaches the surface without scattering is denoted by $F_{e-e}(E, \omega, \theta)$. This probability depends on the photon absorption length, λ_{opt}, and the electron-electron mean-free path, λ_{e-e}. All steps of the Spicer model are present in this mathematical relationship. Photon absorption appears with the reflectivity term $1 - R(\omega)$, representing the fraction of incident photons absorbed. For the second step, the relevant parameters are λ_{opt} and

λ_{e-e}. For copper, the most relevant scattering is electron-electron scattering. The third step involves integrals over the energy spectrum, azimuthal, and polar angles. The denominator represents the maximum number of electrons a photon can excite. For a metal, the QE is quite low due to two reasons: the photon's energy can reach only a limited number of occupied electron states, and the acceptance angle through which electrons can escape is small. Integrating the formula gives the following result:

$$QE = \frac{1 - R(\omega)}{1 + \frac{\lambda_{\text{opt}}}{\lambda_{e-e}}} \left(\frac{E_F + \hbar\omega}{2\hbar\omega} \left(1 - \sqrt{\frac{m}{m^*} \frac{E_F + \phi_{\text{eff}}}{E_F + \hbar\omega}} \right)^2 \right) \tag{2.19}$$

Using a similar 3-step approach, one can compute the variance of the transverse momentum, which determines the normalized photoelectric emittance.

$$p_x = \sqrt{2m(E + \hbar\omega)} \sin\theta \cos\phi \tag{2.20}$$

Calculating the mean square of the momentum:

$$\langle p_{\text{tot}}^2 \rangle = \frac{2m \int_{E_f + \phi_{\text{eff}} - \hbar\omega}^{E_f} dE \int_{\sqrt{\frac{E_f + \phi_{\text{eff}} - \hbar\omega}{E_f + \hbar\omega}}}^{1} d(\cos\theta) \int_0^{2\pi} d\phi \, (E_f + \hbar\omega) \sin^2\theta \cos^2\phi}{\int dE \int d\phi \int d(\cos\theta)} \tag{2.21}$$

Solving the integral gives:

$$\epsilon = \sigma_x \sqrt{\frac{\hbar\omega - \phi_{\text{eff}}}{3mc^2}} \tag{2.22}$$

To minimize intrinsic emittance, it is essential to reduce the energy difference, $\Delta = \hbar\omega - \phi_{\text{eff}}$, between the energy of the incident photons and the effective work function of the material. However, since quantum efficiency is proportional to Δ^2, achieving a low intrinsic emittance also leads to reduced quantum efficiency. Depending on the application, the choice of cathode must be driven not only by quantum efficiency but also by intrinsic emittance, which represents the ultimate achievable emittance. The electrons emitted by the photocathodes are accelerated in an RF gun. It operates at high frequencies, commonly in the S-band (2.856 GHz) L-band (1.3 GHz), or C-band (5.712 GHz), and generates an oscillating electric field that accelerates the electrons. The accelerating gradient E_z in the RF cavity is given by:

$$E_z(z,t) = E_0 \cos(\omega_{RF} t - kz + \phi)$$

where E_0 is the peak electric field, ω_{RF} is the RF angular frequency, k is the wave number, and ϕ is the phase offset. The high electric field, hundreds of MV/m, is necessary both for extracting the electron and for emittance preservation. Since the gun acts as a defocusing lens, it is equipped with a solenoid for emittance compensation. The solenoid magnet in an RF photoinjector is strategically placed near the exit of the RF cavity, typically close to the photocathode. Its primary purpose is to focus the electron beam and compensate for emittance growth due to space-charge effects as the electrons are emitted and initially accelerated. The beam's emittance initially increases rapidly due to space-charge effects as the electron bunch exits the photocathode. The solenoid field is tuned to produce a "waist" in the beam envelope, where the transverse beam size is minimized before the beam is injected into the acceleration structures following the Gun (Fig 2.4). The compensation

occurs when the beam's transverse phase space distribution (position vs. momentum) is linearized, meaning that the correlation between position and momentum is minimized at a specific point, often referred to as the emittance compensation point. The magnetic field produced by the solenoid is given by:

$$B_z(r,z) = \frac{\mu_0 n I}{2}\left(\frac{L}{\sqrt{(z-z_0)^2+L^2}}\right) \tag{2.23}$$

where:

- μ_0 is the permeability of free space,
- n is the number of turns per unit length of the solenoid,
- I is the current through the solenoid,
- L is the length of the solenoid, and
- z_0 is the position of the solenoid center along the beam axis.

To achieve optimal emittance compensation:

- The solenoid current I and its position relative to the photocathode are carefully adjusted.
- The focusing strength $K(z)$, which is proportional to $B_z(z)$, is tuned to match the natural expansion of the beam due to space charge, leading to a balanced focusing effect.

The solenoid must generate a uniform and symmetric magnetic field to avoid introducing additional emittance growth. Non-uniformities in the field can lead to beam distortions. After the initial acceleration,5-6 MeV, the electrons enter the booster section. The booster section has two primary

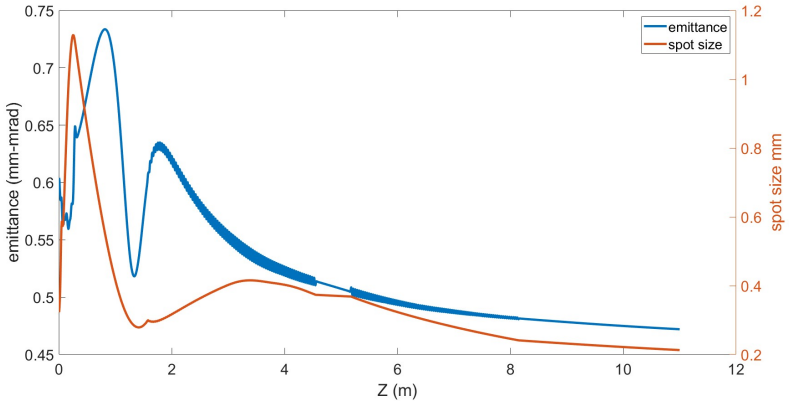

Figure 2.4: The evolution of the emittance and spot size along an injector: the solenoid creates a waist before the beam enters the accelerating structure (approximately 1.7 m from the cathode), and at the same point, the emittance exhibits a relative maximum.

purposes:

1. **Further Acceleration**: The booster section accelerates the electron beam to higher energies, typically hundreds of MeV, to achieve the emittance dominant regime.
2. **Beam Quality Preservation**: Applying the compression and compensation techniques improves the beam quality.

In particle accelerators, the beam evolves through different regimes depending on the interplay between space charge forces and emittance pressure. These regimes critically impact the beam dynamics, and quality, particularly during the transition from low-energy to high-energy states. The dominant factor in beam propagation can be understood through the laminarity parameter ρ_{SC}, which measures the relative influence of space charge forces against the emittance pressure. A space charge-dominated regime occurs when the collective repulsive forces between particles in the beam—due to their like charges—are significantly stronger than the internal "thermal" pressure exerted by the beam's emittance. These space charge forces cause the beam to expand and can lead to correlated emittance growth, which is reversible under proper conditions. In this regime, the beam exhibits quasi-laminar flow, meaning that particles follow smooth, non-intersecting trajectories, a behavior maintained as long as focusing and acceleration are carefully adjusted. The space charge effect is quantified using a dimensionless parameter, ρ_{SC}, defined as:

$$\rho_{SC} = \frac{2\hat{I}}{I_A}\frac{\sigma^2}{\gamma^2\epsilon_n^2} \tag{2.24}$$

where $\hat{I}$ is the peak current of the beam, I_A is the Alfvén current (17 kA for electrons), σ is the beam's root mean square (rms) size, γ is the relativistic Lorentz factor, and ϵ_n is the normalized emittance. A high value of ρ_{SC} (significantly greater than 1) indicates a space charge-dominated regime, where the collective forces due to particle density are dominant [14]. In the space charge dominated regime ($\rho_{SC} \gg 1$), space charge forces cause the beam to expand unless counteracted by external focusing elements. This quasi-laminar propagation requires fine-tuning of focusing magnets and accelerating structures to ensure that the beam remains well-behaved. If these conditions are met, the correlated emittance growth caused by space charge forces can be made reversible, preserving beam quality. Conversely, when $\rho_{SC} < 1$, the beam is in an emittance-dominated regime, where the thermal emittance pressure—the inherent spread in the beam's phase space—becomes the primary factor influencing the beam's behavior. In this case, space charge forces are weak, and particle trajectories can intersect, indicating a shift away from laminar flow towards a more thermal-like behavior. The transition from space charge dominance to emittance dominance is marked by threshold energy, known as the transition energy E_{tr}. At this point, the laminarity parameter ρ_{SC} is approximately 1, indicating that space charge forces and emittance pressure have comparable influence. The transition energy is given by:

$$\gamma_{\mathrm{tr}} = \sqrt{\frac{2\hat{I}}{I_A}\frac{\sigma^2}{\epsilon_n^2}} \tag{2.25}$$

where γ_{tr} is the Lorentz factor at the transition. For example [15], with a peak current $\hat{I} = 100$ A, a normalized emittance $\epsilon_n = 1\,\mu$m, and an rms beam size $\sigma = 300\,\mu$m, the transition energy for an electron beam is approximately 131 MeV. This energy threshold highlights the fact that low-energy beams are often space charge-dominated, while high-energy beams tend to be emittance-dominated. Since for the PWFA working point the typical current is in the order of the kAs (as you will see in the following chapters), the space charge effect strongly dominates the dynamics, so the control and optimization of the electron beam dynamics at this point is crucial. The space charge-dominated regime is typical of the initial stages of acceleration, particularly in injectors where the beam energy is low, and the particle density is high. In this phase, maintaining laminar

flow requires precise matching conditions to counteract the strong space charge forces. The design of the injector often involves the use of strong focusing elements to keep the beam's size under control and avoid excessive emittance growth. As the beam progresses into higher-energy regions, such as in the booster stage, the relativistic factors β and γ increase, which reduces the influence of space charge forces due to the dependence on $1/(\beta^3\gamma^3)$. Thus, the booster stage transitions into an emittance-dominated regime, where beam dynamics are less sensitive to collective forces, allowing for finer control over emittance growth and beam shaping. For advanced applications, such as FELs, maintaining high beam quality is crucial. These systems often operate with high peak currents (kiloampere range), which can reintroduce space charge effects even at high energies, particularly after the use of bunch compressors that increase the beam density. This necessitates a new energy threshold to be considered, requiring careful management of space charge effects at each stage of acceleration. To mitigate space charge-induced emittance growth in RF linacs, particularly in high-brightness photoinjectors, the goal is to ensure a smooth transition from a space charge-dominated regime to an emittance (thermal) dominated regime. The strategy involves damping emittance oscillations caused by space charge forces along the booster, ensuring that an emittance minimum is achieved precisely at the transition energy. For a stable transition, it is crucial to properly match the beam to the accelerating structures. This is often achieved by configuring the beam to exhibit a flow pattern similar to a Brillouin flow, where the internal forces in the beam are in balance. In such a configuration, space charge forces, beam emittance, and focusing elements are tuned to maintain equilibrium, minimizing emittance oscillations. This balance is essential because emittance oscillations—if not controlled—can degrade the beam quality. In RF booster, ponderomotive RF focusing plays a key role in controlling emittance growth. The ponderomotive force arises from the interaction of the particles with the oscillating RF fields within the accelerating cavities, providing a focusing effect that helps counteract space charge forces. This RF focusing is designed to control the transverse size of the beam, dampen space charge-induced emittance oscillations, and guide the beam smoothly toward the thermal regime. However, RF focusing may not always be strong enough to fully contain the beam, particularly in cases where high-brightness beams with significant space charge forces are involved. This limitation arises because the ponderomotive focusing force in standard RF structures might not be sufficient to fully counterbalance the expansive effects of space charge [16]. As a solution, a long solenoid can be placed around the accelerating structure to provide additional focusing strength. The magnetic field from the solenoid supplies continuous, uniform focusing, which helps maintain beam containment throughout acceleration. This approach allows for better control over the beam's transverse profile, ensuring that emittance oscillations are minimized and guiding the beam through the critical transition from space charge-dominated to emittance-dominated behavior. Achieving an emittance minimum at the transition energy is crucial because it marks the point where space charge effects begin to diminish, and the beam's behavior is predominantly influenced by its emittance. By ensuring that the emittance is at its lowest at this transition, the beam quality is preserved as it enters higher energy regimes, where emittance becomes the primary factor governing beam dynamics. This careful matching, combined with the use of appropriate focusing methods (RF or solenoid-based), is essential for maintaining the brightness and quality of the beam in applications that require precise control, FELs and high-energy colliders. Understanding this transition and how to control it is critical for designing accelerators that can achieve the precise beam properties required for applications like PWFA and advanced light sources.

2.2 Manipulation of high brightness beams, high current, and low emittance operations

Simulation codes are powerful and useful tools to study the dynamic of electron beams, more details are in Appendix A. We will now go on to discuss what are the techniques to be able to have beams of high brightness, high current, and low emittance going also to dwell on what simulative aspects must be taken into account. Electron bunches with durations in the picosecond range are produced in RF guns with peak currents of less than tens of Ampere and charge from tens to hundreds pC. To achieve peak currents in the kiloampere range at higher beam energies, hundreds of MeV, bunch compressors are used to compress these bunches to durations on the order of tens of femtoseconds. The main techniques that are used to compress electron beams are:

- ballistic compression (Fig 2.5) [17]: Ballistic compression is achieved by first imparting a chirp to an electron bunch in a chirper cavity at the zero-crossing point of the RF field. This process results in a linear energy spread within the bunch, where electrons at the head of the bunch are slower and those at the tail are faster. As the bunch drifts through a drift space, the slower electrons at the front gradually fall back towards the centroid, while the faster electrons at the rear catch up with it, leading to a compressed bunch. Ballistic compression is typically performed at low beam energies, specifically below few MeV, because the magnitude of the longitudinal dispersion parameter (R56) decreases quadratically with increasing beam energy, following the relation $1/\gamma^2$. This lower energy facilitates a more effective compression process by allowing a greater separation and subsequent re-alignment of electron velocities within the bunch.

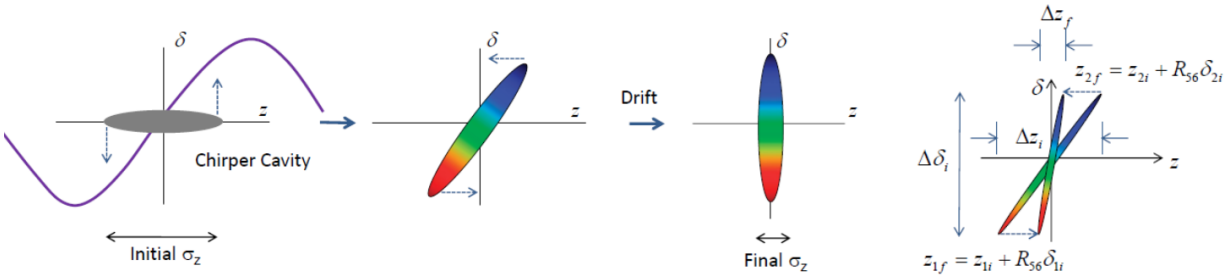

Figure 2.5: Ballistic compression scheme: as the bunch drifts through a drift space, the slower electrons at the front gradually fall back towards the centroid, while the faster electrons at the rear catch up with it, leading to a compressed bunch..

- chicane compressor (Fig 2.6): A chicane comprises four rectangular dipole magnets, each of length L. The first and second dipoles, as well as the third and fourth dipoles, are separated by a distance D. Notably, the distance between the second and third dipoles does not contribute to the longitudinal dispersion parameter (R56), which is crucial for manipulating the path length differences that lead to bunch compression.

- velocity bunching [18] [19] (Fig 2.7): It is a method for compressing an electron bunch by means of electromagnetic fields of an accelerating structures. It is a longitudinal phase space rotation based on a correlated time-velocity chirp of the electron bunch, (electrons on the tail faster than electrons in the head). This rotation occurs inside the longitudinal potential of a

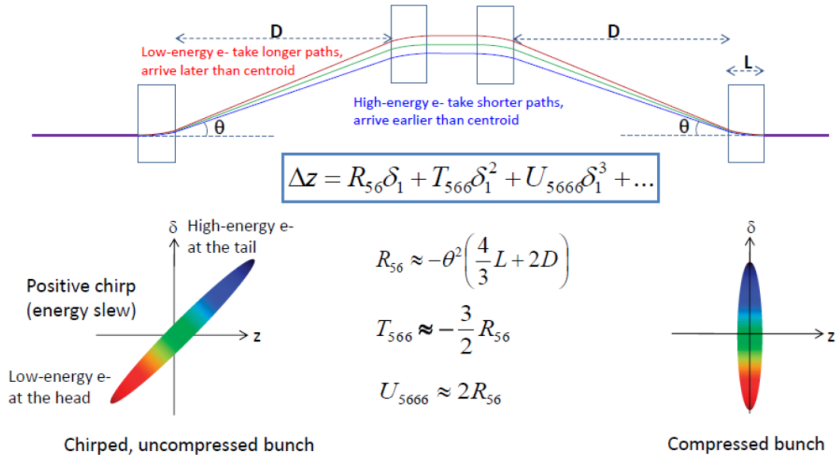

Figure 2.6: chiacane compression scheme comprises four rectangular dipole magnets.

traveling rf wave (longitudinal focusing) if the injected beam is slightly slower than the phase velocity of the rf wave so that when injected at the zero-crossing field phase it slips back to phases where the field is accelerating, being simultaneously chirped and compressed. Both compression and acceleration take place at the same time within the same accelerator section, the initial one following the gun. Again, if a beam, slower than the synchronous velocity, is injected into an RF wave at the zero-acceleration phase the beam slips back in phase up to the peak acceleration phase and it can be compressed as far as the extraction happens at the synchronous velocity. Compression factors ranging from 5 to 15 can be achieved [20].

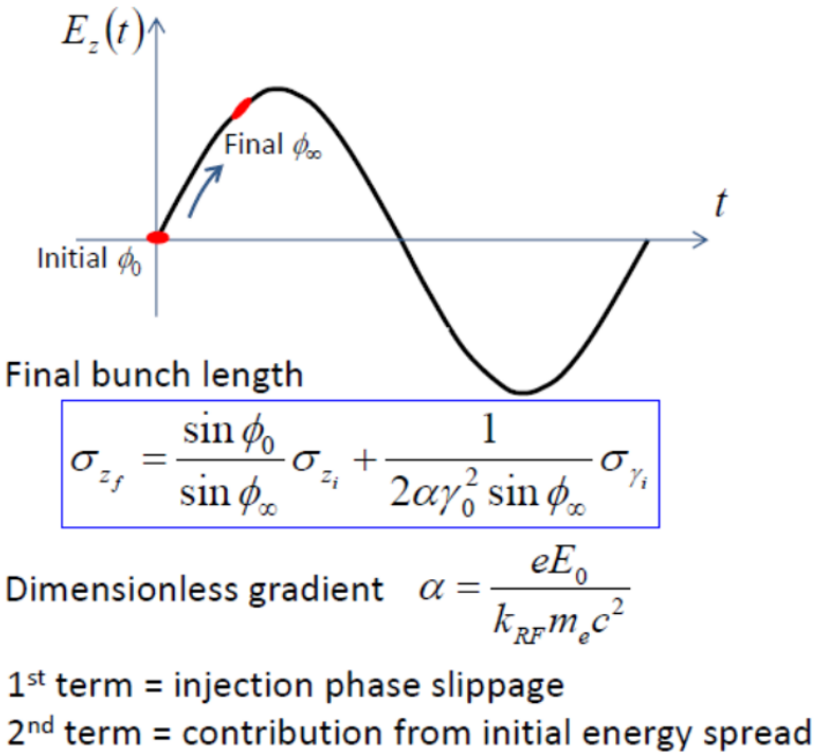

Figure 2.7: Velocity bunching scheme [18][19].It is a longitudinal phase space rotation based on a correlated time-velocity chirp. This rotation occurs inside the longitudinal potential of a traveling RF wave if the injected beam is slightly slower than the phase velocity of the rf wave.

As was pointed out earlier the energy of the electron beam is a discriminating parameter in using one technique over another. The most popular and effective device used to date is the magnetic compressor. However, the process of magnetic compression can often lead to unacceptable degradation of beam quality. This degradation is primarily due to significant emittance growth, which is caused by the effects of coherent synchrotron radiation (CSR) in the bending magnets. CSR can induce energy spread and transverse emittance growth, thereby compromising the overall performance of the compressed electron beam. Velocity bunching, on the other hand, can compress the beam at low energy and using rectilinear trajectories , thus allowing it to be integrated into emittance compensation processes. The compensating systems are the gun solenoid and a long solenoid that winds the accelerating structure where velocity bunching occurs (Fig 2.8). The ponderomotive RF focusing force for a traveling wave accelerating structure is too weak to keep the beam focused. The

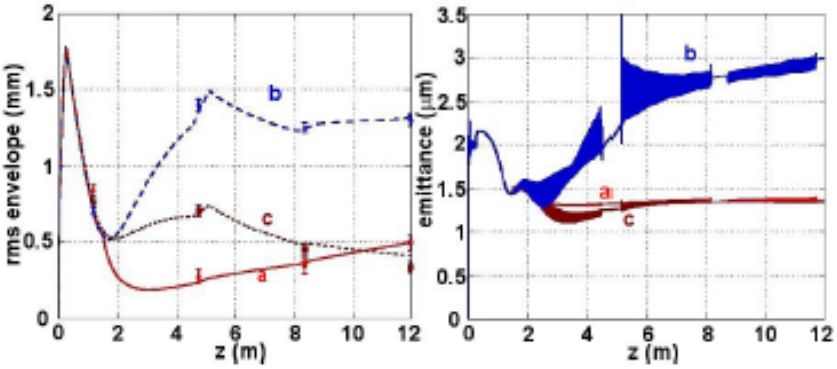

Figure 2.8: Example of SPARC_LAB measured envelopes and simulations (left plot). Emittance evolution along the linac, simulations (right plot). No compression (curves a), compression with long solenoids off (curves b), same compression with long solenoids set to 450 G (curves c).

velocity bunching compression scheme lends itself to be the best solution, with the limitations and issues that will be discussed below for use as a method for generic high-brightness electron beams for PWFA applications. As for the case of a Langmuir wave in a cold plasma, the longitudinal component of the RF field in a traveling wave structure can be approximated by:

$$E_z = -E_0 \sin(\omega t - kz + \phi_0) \tag{2.26}$$

where the wave number $k = \frac{\omega}{v_\phi}$, the phase velocity $v_\phi = \frac{c}{\sqrt{1-\beta_\phi^2}}$, and the adimensional wave amplitude $a \equiv \frac{eE_0}{mc\omega}$. The Hamiltonian of the interaction between the wave and the electron can be written as:

$$H = \gamma - \beta_\phi^2 \sqrt{\gamma_\phi - 1} - a\cos\psi \tag{2.27}$$

with $\gamma = 1 + \frac{T}{mc^2}$ and $\psi = kz - \omega t - \phi_0$ is the phase of the wave seen by the electron. Considering a wave with phase velocity slower than c so $k = k_0 + \Delta k = \frac{\omega}{v_\phi} + \Delta k$, with $\Delta k \ll k_0$, the resonant β and γ can be approximated by:

$$\beta_\phi \approx 1 - \frac{\Delta k}{k_0} = 1 - \frac{c\Delta k}{\omega} \tag{2.28}$$

and

$$\gamma_\phi \approx \sqrt{\frac{k_0}{2\Delta k}} = \sqrt{\frac{\omega}{2c\Delta k}}. \tag{2.29}$$

In Fig 2.9, a particle distribution at injection is depicted in a small phase space area located around $x = 0$ and $\gamma_0 = 3$, i.e., well below γ_r where the resonance γ satisfies the condition where the average velocity of the particle beam allows for optimal interaction with the accelerating electromagnetic field, maximizing the temporal compression (bunching) of the beam (i.e., particles initially slower than the wave) and close to the bottom of the cup-shaped bucket. This bunch of particles is accelerated by the wave while it slips back in phase: once at the resonant energy γ_r, it will reach a phase of about $x = -60°$. As depicted in the diagram, due to the nature of the phase lines, the bunch will have a phase spread (i.e., a bunch length since it is quite relativistic at this point) smaller than the initial. Everything happens in the same acceleration section at the gun exit, the

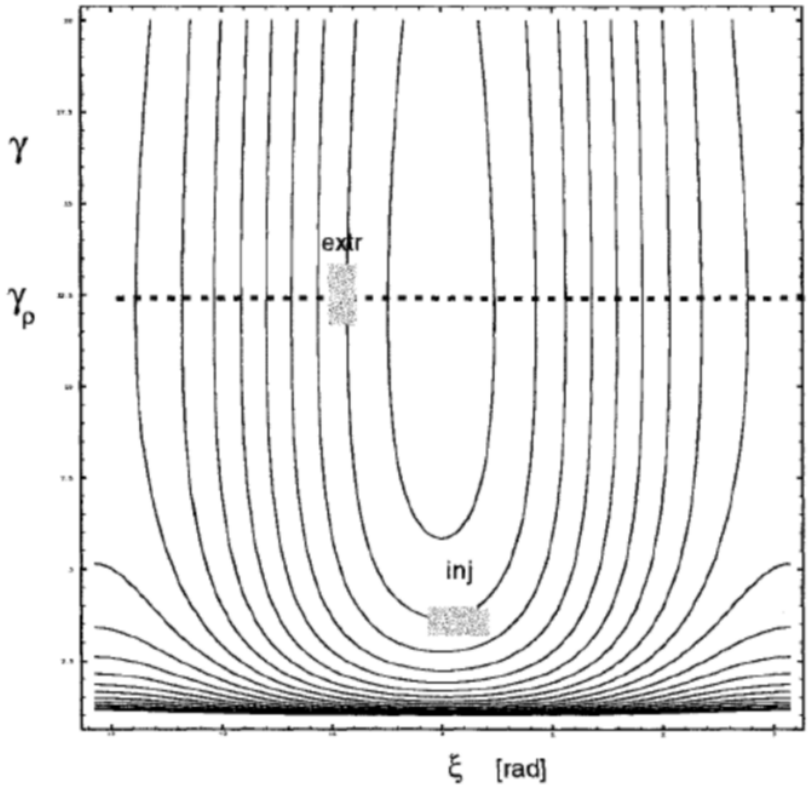

Figure 2.9: Velocity bunching mechanism [19].

laminarity of the electron beam must be preserved as close as possible to the Brillouin-like flow, i.e., satisfying the invariant envelope condition under compression and current increasing during acceleration. The beam has to be injected into the RF structure with a laminar envelope waist ($\gamma' = 0$), and the envelope has to be matched to the accelerating and focusing gradients to stay close to an equilibrium mode. To provide the necessary beam focusing to control the emittance oscillations, a long solenoid around the accelerating structure must be foreseen. The matching condition then becomes:

$$\sigma = \frac{1}{k}\sqrt{\frac{I_0}{4\gamma_0 I_A}(1 + \sqrt{1 + \frac{4\epsilon_n \gamma_0 k I_a}{I_0}})^2} \tag{2.30}$$

where $k = \frac{eB_{sol}}{mc}$, B_sol is the magnetic filed of the solenoids around the structures $I_a = 17kA$, ϵ_n = normalized emittance, γ_0 = energy at injection, I = current at injection. This is the exact equilibrium solution of the envelope equation:

$$\sigma'' + \frac{\gamma'}{\gamma}\sigma' + (\frac{k}{\gamma})^2\sigma = \frac{I}{2I_A\sigma\gamma^3} + \frac{\epsilon_n^2}{\gamma^2\sigma^3} \tag{2.31}$$

with $\gamma \approx 2E_{acc}$ [MV/m] and with linear approximation $I = \frac{I_0\gamma}{\gamma_0}$. To compress the beam, the accelerating phase of the traveling wave structure must be shifted from the maximum gain condition (on crest operations). Experimentally at SPARC_LAB [2], it was observed that appreciable beam compression is obtained by going to the -85° region. This condition is strongly dependent on the beam characteristics. The experiment with a 280 pC beam shows that moving away from the maximum gain zone, the beam energy goes from 130 MeV to 100 MeV with a spread in energy of 1%. The maximum compression of the beam is obtained by moving the phase up to -95° Fig (2.10). The evolution of the compression phase and beam length are shown in the figure. The ASTRA code

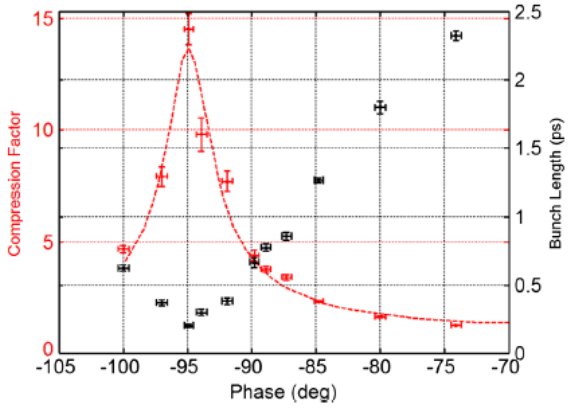

Figure 2.10: Example of SPARC_LAB measured rms bunch length (black) and corresponding compression factor (red) of a 280 pC beam versus the phase of the first traveling wave structure. Simulations are also shown with a dashed red line [20].

allows velocity bunching to be simulated very accurately, [21]. The autophase flag finds the phase of maximum gain and sets it to zero. Moving from this point, we can then explore all regions of the phase ranging from compression to overcompression. The case studies where ASTRA has been used will be presented in the following sections.

Chapter 3

EuPRAXIA@SPARC_LAB

EuPRAXIA@SPARC_LAB (Fig. 3.1) aims to be the first European research infrastructure to demonstrate the application of a plasma accelerator. This facility combines a high-brightness electron beam in the GeV range, produced by a state-of-the-art linac, with a powerful 0.5 PW-class laser system [3][4]. The EuPRAXIA@SPARC_LAB facility will be a cutting-edge research center dedicated to X-ray FELs with electrons accelerated by a plasma-based acceleration system, the parameters of the radiation are in Tab 3.1. This system utilizes a sophisticated "particle-driven

Radiation Parameter	**Unit**	**Value**
Radiation Wavelength	nm	3-4
Photons per Pulse	$\times 10^{12}$	0.1-0.25
Photon Bandwidth	%	0.1
Undulator Area Length	m	30
ρ(1D/3D)	$\times 10^{-3}$	2
Photonbrightness per shot	$\left(\frac{s}{\text{mm}^2\text{mrad}^2\,\text{bw}(0.1\%)}\right)$	$1 - 2 \times 10^{28}$

Table 3.1: Radiation parameters for PWFA configurations.

configuration" to achieve highly efficient particle acceleration. In this setup, an ultra-relativistic electron beam, known as the "driver" beam, passes through a plasma medium. This interaction generates a plasma wake, characterized by a fluctuating charge density. This plasma wake is crucial as it creates an electric field that accelerates a secondary electron beam, referred to as the "witness beam," to high energies. The electrons needed for this process are produced using a technique known as the "comb technique." This method involves an RF injector system, which comprises several advanced components. These components work in concert to generate and accelerate electron bunches with the desired characteristics. In the typical operating scenario, the system is designed to handle a witness beam with a charge of 30 picocoulombs (pC) and a driver beam with a charge of 200 pC. These beams are longitudinally compressed within the first two accelerating structures, which operate in the "velocity-bunching" regime. This specific regime is essential as it allows for the compression and acceleration of electron beams, optimizing their transverse and longitudinal properties to achieve the desired performance in plasma acceleration Tab 3.2. Once the beam is injected into the plasma, its initial parameters degrade if not matched with the optimal conditions. Therefore, the beam must be injected with high quality to achieve the desired parameters presented in the previous table. This highlights the critical role of the injector in ensuring optimal beam

Electron Beam Parameter	Unit	PWFA
Electron Energy	GeV	1-1.2
Bunch Charge	pC	30-50
Peak Current	kA	∼2
RMS Energy Spread	%	<1
RMS Bunch Length	μm	3-6
RMS norm. Emittance	μm	1
Slice Energy Spread	%	≤0.05
Slice norm. Emittance	mm-mrad	0.5
Energy jitter	%	<1

Table 3.2: Electron beam parameters from the plasma stage.

quality. Optimizing the emittance of the witness beam—a critical parameter that measures the spread of the beam in phase space—is fundamental for ensuring beam quality. This optimization process is achieved through several approaches, including the application of additional magnetic fields around the RF gun and the velocity-bunching S-band structures. Additionally, the laser pulse at the cathode is meticulously shaped to enhance the characteristics of the emitted electron bunches, optimizing spot sizes, charge and bunch separation to produce well know parameters. A significant aspect of the study involves examining the beam dynamics with the introduction of an X-band RF cavity placed after the gun. This X-band RF cavity is proposed as a tool to shape the beam current distribution and to stabilize the beam by mitigating the effects of RF jitter. RF jitter can cause fluctuations and instabilities in the beam, impacting the overall performance of the acceleration system. This chapter provides a detailed discussion of the beam dynamics studies conducted with the addition of the X-band RF cavity and other optimizations. The insights gained from these studies are crucial for improving beam quality and stability, ultimately contributing to the advancement of the X-ray FEL capabilities at EuPRAXIA@SPARC_LAB. These improvements not only enhance the performance of the accelerator but also advance scientific and technological progress in the field of particle accelerators. This chapter presents also references to studies conducted at the SPARC_LAB test facility, which served as a training ground for testing and refining various techniques central to optimizing the EuPRAXIA@SPARC_LAB photoinjector.

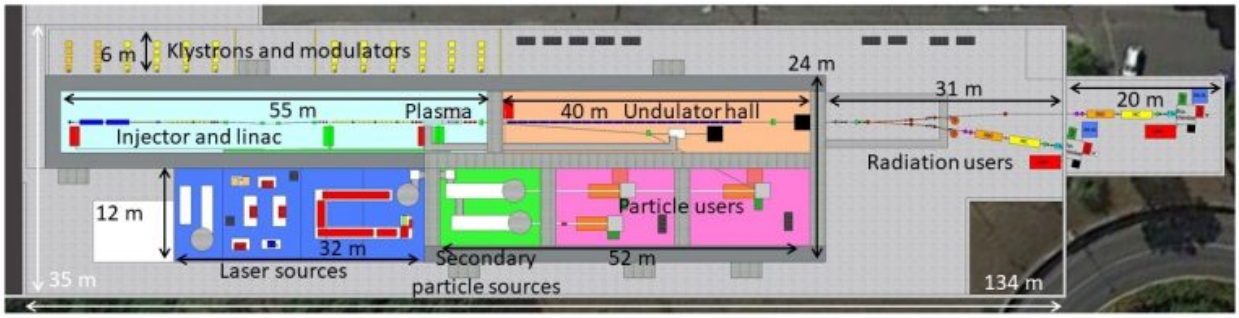

Figure 3.1: EuPRAXIA@SPARC_LAB layout [3].The EuPRAXIA@SPARC_LAB project, intended to put forward LNF as host of the EuPRAXIA European Facility, will be able to accommodate any machine configuration resulting from the EuPRAXIA Design Study. In order to achieve this goal and to meet the EuPRAXIA requirements, some important preparatory actions must be taken at LNF. Provide LNF with a new infrastructure with the size of about 155 m x 35 m, as the one required to host the EuPRAXIA facility.

3.1 The high-brightness EuPRAXIA@SPARC_LAB injector

The EuPRAXIA@SPARC_LAB facility is set to utilize an advanced RF gun, specifically a 1.6-cell model based on the well-known BNL/SLAC/UCLA design. This gun incorporates a range of innovative modifications that were first implemented in the ELI-NP gun [22] and have since been integrated into the newly developed gun for the SPARC photo-injector. Compared to its original design, this updated version offers numerous enhancements, as detailed in Tab 3.3. One of the significant improvements is the iris profile, which has been meticulously designed with an elliptical shape and a larger aperture. This design choice serves multiple purposes: it reduces the peak surface electric field, increases the frequency separation between the two resonant modes (the operational π-mode and the non-operational 0-mode), and enhances the pumping efficiency within the half-cell [23]. Such advancements lead to improved performance and stability of the RF gun. Fig 3.2(b) and 3.2(c) provide visualizations of the magnetic field in the coupler region when the cathode peak field is at 120 MV/m, alongside the longitudinal accelerating field profile. The input coupling coefficient (β) is intentionally set at 3 to reduce the filling time, enabling efficient operation with shorter RF pulses, which is crucial for high-rep rate applications. The photo-cathode, an essential component,

Gun Parameter	**Unit**	**Value**
Resonant frequency	GHz	2.856
$\frac{E_{\text{cath}}}{\sqrt{P_{\text{diss}}}}$	MV/(m·MW$^{0.5}$)	37.5
RF input power	MW	14
Cathode peak field	MV/m	120
Rep. rate	Hz	50
Quality factor		14600
Coupling coefficient		3
RF pulse length	μs	1.0
Mode separation	MHz	41.3
$\frac{E_{\text{surf}}}{E_{\text{cath}}}$		0.9
Pulsed heating	deg C	<30
Average diss. power	W	400
Working temperature	deg	30

Table 3.3: Parameters of the gun

is strategically positioned on the flange that seals the half-cell. The requirement for a short response time of the cathode is critical for enabling precise electron beam shaping through laser pulse manipulation. This requirement limits the choice of cathode materials to metals with response times in the range of a few tens of femtoseconds [24]. Based on extensive research and experimental results obtained worldwide from various laboratories, the most promising candidate metals for serving as sources for electron beams are copper (Cu), magnesium (Mg), and yttrium (Y). These metals have shown great potential due to their favorable properties. A crucial parameter influencing the selection and operation of the photo-cathode is its QE at the drive laser wavelength. Measurements of the QE for these metals under similar conditions with UV laser irradiation at 266 nm have yielded values of approximately 4×10^{-5} for copper, 5×10^{-4} for magnesium, and about 2×10^{-4} for yttrium. These measurements indicate their effectiveness and suitability for specific applications. In the initial phase of the EuPRAXIA@SPARC_LAB project, a copper cathode will be used due to its reliable perfor-

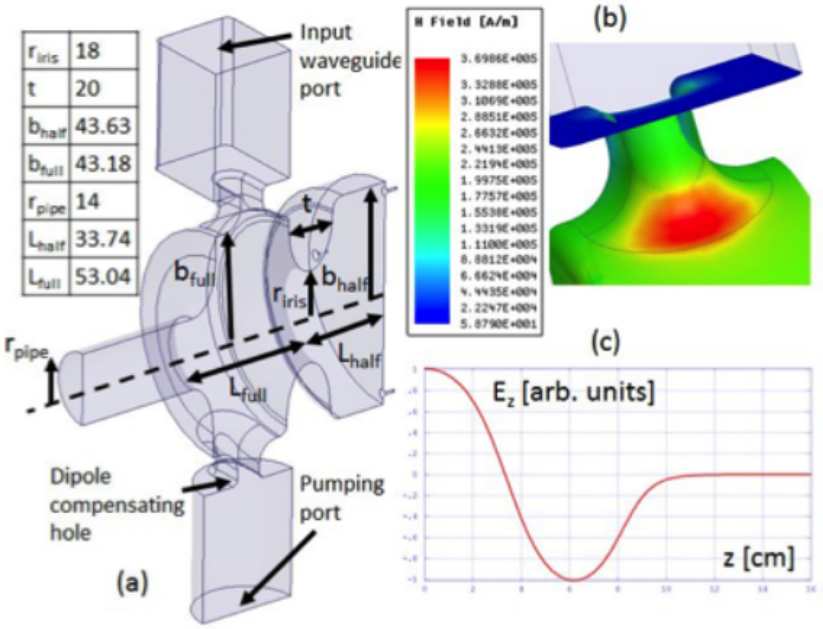

Figure 3.2: EuPRAXIA@SPARC_LAB gun layout with specification of the magnetic field in the coupler region when the cathode peak field is at 120 MV/m. [3].

mance and established track record in similar applications. Copper's properties make it a strong candidate for facilitating the successful implementation of this state-of-the-art RF gun technology. The gun is equipped with a solenoid, which together with the design of the gun itself is necessary to compensate the emittance and final parameters of the injector. The EuPRAXIA@SPARC_LAB

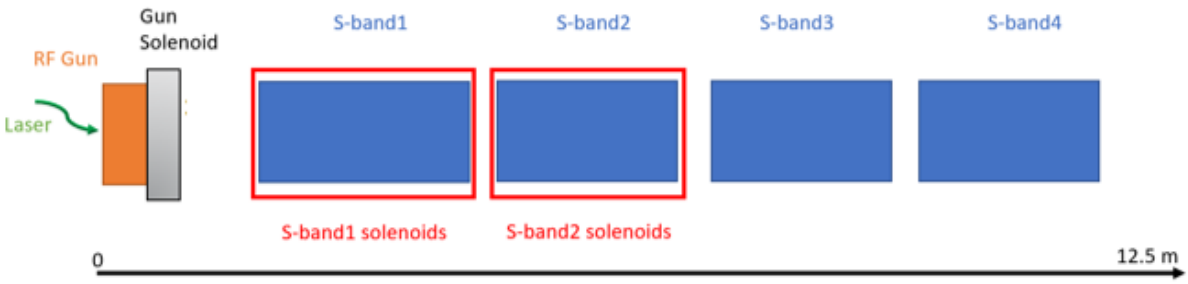

Figure 3.3: EuPRAXIA@SPARC_LAB injector layout. The gun is equipped with a solenoid, which together with the design of the gun itself is necessary to compensate for the emittance and final parameters of the injector. The gun is followed by four S-band TW accelerating structures, which play a crucial role in accelerating and manipulating the electron beam

photo-injector is now fully equipped with four S-band accelerating structures, which play a crucial role in accelerating and manipulating the electron beam through the velocity bunching compression scheme, also known as RF compression (Fig 3.3). This technique effectively compresses the electron bunches, enhancing their brightness and quality. However, the compression process can lead to emittance growth, which must be carefully controlled. To address this, an additional magnetic field is strategically shaped around the accelerating structures using two solenoids positioned around the first two structures. These solenoids are essential for emittance compensation, ensuring that the beam maintains its quality during compression. Simulations indicate that achieving compression factors greater than three requires precise tuning of the coils that compose the solenoids enclosing

the structures. This need for precision has been experimentally verified at SPARC_LAB, where careful adjustments have demonstrated the importance of fine-tuning in optimizing beam compression. The accelerating structures of the EuPRAXIA@SPARC_LAB S-band injector are designed as traveling wave (TW), constant gradient (CG) systems with a $2\pi/3$ phase advance per cell. The first 3 meters long while the others 2 meters long and operate at a frequency of 2.856 GHz. Among the most critical parameters of these devices is the maximum achievable accelerating gradient, which determines the injector's performance. To reach the required nominal energy of approximately 150 MeV, the average accelerating field across the four SLAC-type sections must be finely controlled to achieve gradients of 21 MV/m, 21 MV/m, 30 MV/m, and 35 MV/m, respectively. These gradients ensure that the electron beam reaches its target energy efficiently, supporting the high standards of experimentation and research at EuPRAXIA@SPARC_LAB. The EuPRAXIA@SPARC_LAB linac is not the subject of study in this thesis, but its main features will be described below to give more context to what will be described next. The X-band (12 GHz) RF linac is designed to increase the electron beam energy to a maximum final value of 500 MeV. This is achieved through X-band RF sections that provide accelerating gradients exceeding 50 MV/m. The RF system is meticulously engineered to produce ultra-short, high-quality electron beams, ensuring superior performance and precision for advanced scientific experiments. The main challenge of EuPRAXIA@SPARC_LAB is to produce a high-brightness plasma-accelerated beam capable of inducing Self Amplified Spontaneous Emission (SASE) in an FEL undulator. To achieve this goal, EuPRAXIA@SPARC_LAB will be designed to maintain a high-brightness beam at the plasma injection stage and ensure the preservation of beam quality during plasma acceleration. This includes carefully controlling the energy spread, which is particularly challenging with plasma-accelerated beams, by setting a positive energy chirp on the witness bunch, its longitudinal phase space is rotated during acceleration, resulting in an ultra-low energy spread that is even lower than the spread at the plasma entrance [25]. The facility's design and technological innovations will focus on overcoming these difficulties to enable successful SASE generation.

3.1.1 Comb beam for PWFA

The PWFA working point relies on the so-called comb configuration. Comb beams are composed of two or more high-brightness electron beams, lasting 10s of fs, separated by a ps-scale time distance. This longitudinally modulated beam is used to drive plasma acceleration modules. In particle-driven plasma Wakefield acceleration, the high-gradient Wakefield is driven by an intense beam of high-energy charged particles (drivers) passing through the plasma. A second, appropriately phased accelerating beam (witness), with a lower charge (tens of pC) than the driver beam (hundreds of pC), is then accelerated from the wake. Control of the dynamics of the witness is critical to achieving the optimal transverse and longitudinal matching required at the plasma entrance to avoid emittance growth during acceleration in the plasma module. PWFA is a technique for accelerating particles using electric fields generated within a plasma. The principles of PWFA are:

- Plasma creation:

  -Ionization: A plasma is created by ionizing a gas, removing electrons from its atoms, and leaving positively charged ions and free electrons.

  -Conditions: The plasma must be dense enough to support the creation of strong wake fields.

- Driving the wakefield:

  -Beam driven: an electron beam, is injected into the plasma. This beam is known as the "driving beam."

  -Creation of trails: As the electron beam passes through the plasma, it pushes free electrons away due to its electric field, creating a trail of positively charged ions behind it. This displacement creates a region of strong electric fields (GV/m), known as the wake field.

- Acceleration of the witness beam:

  -Witness beam: A second beam of particles, known as the "witness beam," follows the propulsion beam into the plasma.

  -Acceleration: The witness beam is trapped in the wakefield and experiences the strong electric fields, which accelerate particles to high energies over short distances, from a few to tens of cm depending on the final beam energy. We analyze the following envelope equation to reach the matching condition for the plasma:

$$\beta_x'' + 2K_{est}^2\beta_x = \frac{2}{\beta_x} + \frac{\beta_x'^2}{2\beta_x}. \tag{3.1}$$

  By simplifying, we denote $\beta_x = \beta$ to rewrite the equation as:

$$\beta'' + 2K_{est}^2\beta = \frac{2}{\beta} + \frac{\beta'^2}{\beta}. \tag{3.2}$$

  This equation is nonlinear due to the terms $\frac{2}{\beta}$ and $\frac{\beta'^2}{\beta}$. Rearranging gives us:

$$\beta'' + 2K_{est}^2\beta - \frac{\beta'^2}{\beta} - \frac{2}{\beta} = 0. \tag{3.3}$$

  Setting $\beta'' = 0$ and $\beta' = 0$ (stationary conditions) leads to the algebraic equation:

$$2K_{est}^2\beta = \frac{2}{\beta}. \tag{3.4}$$

  Multiplying through by β gives:

$$2K_{est}^2\beta^2 = 2 \implies K_{est}^2\beta^2 = 1 \implies \beta^2 = \frac{1}{K_{est}^2} \implies \beta = \pm\frac{1}{K_{est}}. \tag{3.5}$$

  Matching conditions are essential for ensuring the stability and optimal performance of plasma accelerators. These conditions aim to align the beam parameters (size, divergence, and energy) with the plasma channel properties. Proper matching conditions are crucial for minimizing beam losses and optimizing energy transfer in plasma accelerators. If the matching conditions are not met, it can lead to beam instability, increased emittance, and ultimately degrade the accelerator's performance. The equation

$$k^2\sigma_x^2 = e\langle xE\rangle \tag{3.6}$$

  expresses the transverse dynamic equilibrium of the beam in the plasma. Here:

- k represents the transverse focusing parameter of the beam.
- σ_x is the transverse size of the beam.
- e is the elementary charge of the beam particles (electrons).
- $\langle xE \rangle$ is the average value of the transverse component of the product of position x and electric field E, corresponding to the average focusing force exerted on the beam.

The Gauss's law for an electric field in a plasma region with electron density n_e is:

$$\nabla \cdot \mathbf{E} = \frac{\rho}{\epsilon_0} \tag{3.7}$$

where:

- ρ is the charge density of the plasma, which depends on the charge of the beam creating a charge separation region in the plasma.
- ϵ_0 is the vacuum permittivity.

For a radially symmetric beam distributed along the longitudinal direction (z), we can write this equation in cylindrical coordinates, considering the radial component E_r of the electric field. In this case, Gauss's law becomes:

$$\frac{1}{r}\frac{d}{dr}(rE_r) = \frac{\rho(r)}{\epsilon_0} \tag{3.8}$$

When a beam of particles moves through the plasma, it separates the electrons from the ions, creating a charge distribution that tends to focus the beam itself. The effective charge density $\rho(r)$ will therefore be proportional to the electron density of the plasma n_e and the elementary charge e:

$$\rho(r) = n_p e \tag{3.9}$$

This charge creates a radially focusing electric field that acts on each particle of the beam. Substituting $\rho(r) = n_p e$ into Gauss's law yields:

$$\frac{1}{r}\frac{d}{dr}(rE_r) + \frac{dEz}{dz} = \frac{n_p e}{\epsilon_0} \tag{3.10}$$

Integrating with respect to r, we find the radial electric field $E_r(r)$:

$$E_r(r) = \frac{n_p e}{2\epsilon_0} r \tag{3.11}$$

This expression shows that the electric field increases linearly with the distance r from the center of the beam, which is typical of a harmonic field in a uniform charge distribution. In the plane $y = 0$:

$$E_x = \frac{n_p e}{2\epsilon_0} x \tag{3.12}$$

Substituting equation 3.11 into equation 3.6 and considering

$$\langle x^2 \rangle = \sigma_x^2 \tag{3.13}$$

we obtain:

$$k^2 = \frac{n_p e^2}{2\epsilon_0} \tag{3.14}$$

$$k_{ext}^2 = \frac{k^2}{\gamma m_0 c^2} \tag{3.15}$$

Substituting equation 3.14 into equation 3.15 and recalling that

$$K_p = \frac{\omega_p}{c} = \sqrt{\frac{n_e e^2}{\epsilon_0 m_e c^2}} \tag{3.16}$$

we will have:

$$k_{ext}^2 = \frac{K_p^2}{2\gamma} \implies k_{ext} = \frac{K_p}{\sqrt{2\gamma}} \tag{3.17}$$

From equation 3.5, we find:

$$\beta_x = \frac{\sqrt{2\gamma}}{K_p} \tag{3.18}$$

In summary, matching conditions in plasma accelerators are crucial for maintaining beam stability and optimizing performance [26]. Understanding the mathematical and physical implications of these conditions allows for better design and operation of plasma-based acceleration systems.

We will focus now on the generation of sub-picoseconds, high-brightness electron bunch trains via laser comb technique for PWFA applications [27]. A comb laser beam is characterized by two or more short pulses, each lasting a few hundred femtoseconds, spaced by a few picoseconds. Such a beam can be generated using a birefringent crystal, such as α-BBO [28], which splits the input pulse into two orthogonally polarized pulses with a time separation proportional to the crystal length. By incorporating additional birefringent crystals, it is possible to generate multi-peak light beams with multiple time-separated pulses. Another technique,[29], involves the use of a split and delay lines with a polarizing beamsplitter and remote-controlled delay lines, that allow a fine-tuning of the intensity and the separation of the pulses. The two beams are generated at the cathode, with the witness beam being the first to be extracted. The dynamics of the beams within the injector must be such that the second beam generated, the driver, reaches the plasma section first. The velocity bunching technique is used to make the two beams switch positions and compress them. As can be seen (Fig 3.4), moving from the region of beam compression to the region of overcompression (phase shift greater than 90 deg), the driver beam overtakes the witness and goes to the head of the comb beam (Fig 3.5). In this way using the same photogun it is possible to drive a plasma section. The emittance compensation technique is as discussed above. At this juncture, however, they play an even greater role given the strongly interacting regime of the two beams, starting from the generation at the cathode where space charge forces play a key role all the way to the crossing region of the beams. The section on the SPARC_LAB facility will describe the layout of the machine and the parameters of the comb beams used.

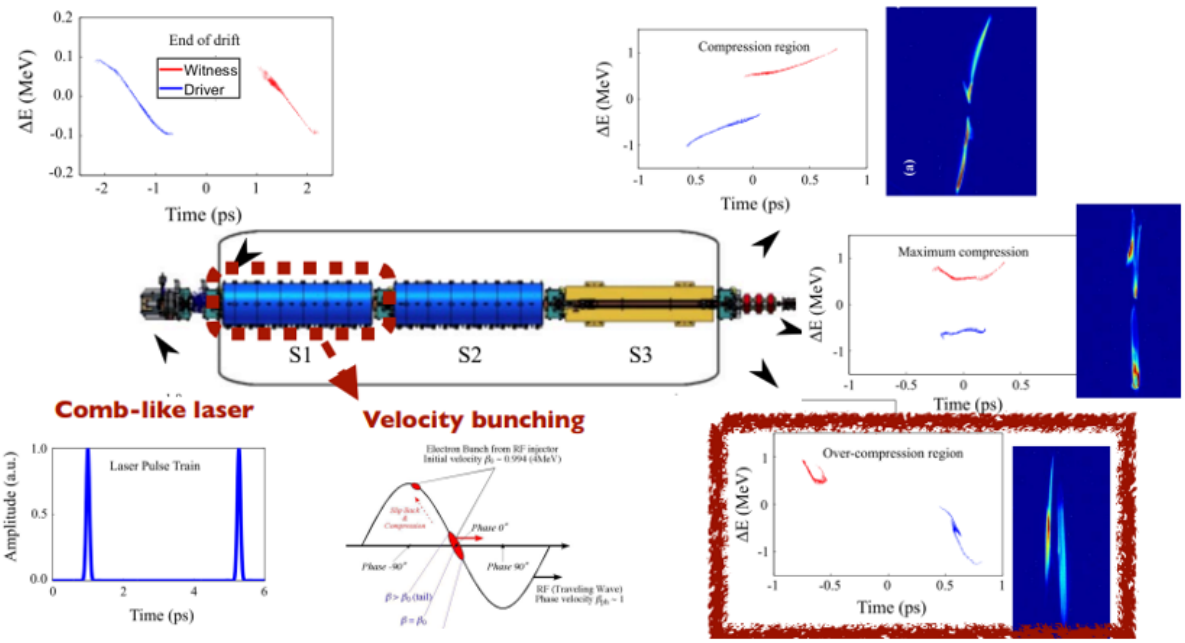

Figure 3.4: Generation and manipulation via velocity bunching technique of comb beam @SPARC_LAB. In the injector, we have three structures, the first two in S-band and the last one in C-band. The first S-band structure is working in the velocity bunching regime.

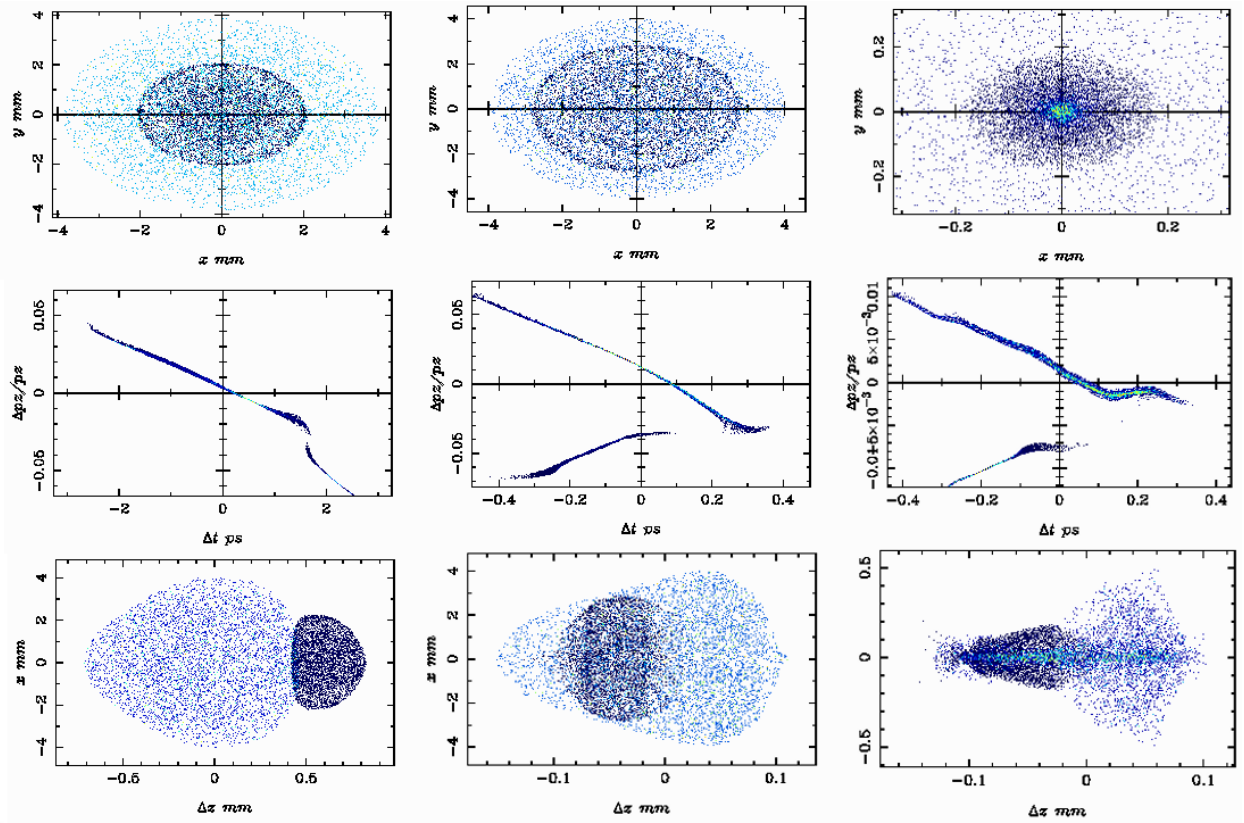

Figure 3.5: Evolution of spot size (first row), longitudinal phase space (second row) and footprint (third row) of a comb beam along the SPARC_LAB injector. The simulation has been done with ASTRA simulation code

3.2 Beam dynamics optimization of the EuPRAXIA@SPARC_LAB S-band photo injector

In this section, I applied the techniques described in the previous section and tested at SPARC_LAB test facility to optimize the EuPRAXIA@SPARC_LAB photo injector dynamics and obtain the beam parameters dictated by this machine, taking into account all the problems in terms of matching in the plasma stage and stability pointed out for the SPARC_LAB linac [30]. As mentioned in the introduction of the section the challenge of this user facility will be to produce high-brightness electron beams that will be accelerated in a plasma accelerator section and sent into an undulator. The optimization of the comb beam dynamics is fully realized in the injector. All parameters of interest in order to inject these beams into the plasma section are optimized in the machine injector, Gun + 4 TW accelerating sections. The X-band linac will be responsible for increasing the energy up to 500 MeV . The parameters that will be the subject of the optimization study of the dynamics of the injector find the emittance, beam length, spot, peak current and among the most important the separation between the centroids of the two beams. The latter can be controlled and optimized only in the first stages of the machine (because of velocity bunching regime), since once the two beams reach the end of the injector at an energy of about 150 MeV their dynamics is frozen and it is no longer possible to separate them further. Comprehensive beam dynamics studies were conducted using a comb-like electron beam, as detailed in Table 3.4. Controlling the dynamics of the

Table 3.4: Cathode's Beam Parameters

Cathode's Beam Parameters	**Witness**	**Driver**
Spot Size	0.175 mm	0.35 mm
Bunch Length	290 fs	290 fs
Charge	30 pC	200 pC
Bunch Separation	4.67 ps	–

witness beam is crucial for achieving optimal transverse and longitudinal matching at the plasma entrance. The witness dynamics precision is necessary to prevent emittance growth, which can degrade beam quality during acceleration within the plasma module. I conducted extensive beam dynamics studies to establish a precise reference working point for the EuPRAXIA@SPARC_LAB photo-injector [31]. These studies ensure that the complex requirements of plasma acceleration are met, allowing for improved performance and efficiency of the accelerator. To date, the TStep code [32] has served as the primary simulation tool, providing insights into the intricate interactions within the accelerator. However, to enhance our analytical capabilities and further optimize beam performance, this section explores the integration of the ASTRA code into our existing toolset. This integration aims to leverage the ASTRA code's compatibility with the GIOTTO algorithm [33], enabling more detailed simulations and better-informed adjustments to the beam dynamics. The beam parameters at the injector exit are summarized in Table 3.5. In this section, we describe the benchmarking simulations conducted to align the ASTRA and TStep codes effectively. This process began by using the cathode distribution parameters detailed in Tab 3.4. The ASTRA input file was carefully adjusted, focusing on the phases, gradients, and magnetic fields of all beamline components to replicate the working point achieved with TStep. The results of the benchmark-

Table 3.5: Reference Injector Exit Parameters

Injector Exit Parameters	Witness	Driver
Spot Size	0.118 mm	0.127 mm
Bunch Length	5 μm	62 μm
Emittance	0.55 μm	1.5 μm
Energy	124 MeV	126 MeV
Energy Spread	0.18 %	0.55 %
Bunch Separation	0.5 ps	–
Peak Current	1.8 kA	–

ing process are illustrated in the following plots. In Fig 3.6 there are the beam's peak currents

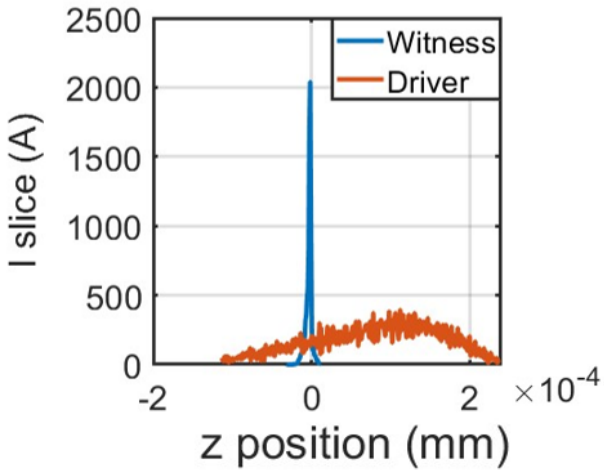

Figure 3.6: ASTRA peak current is higher (2kA) than the one in Table 3.5.

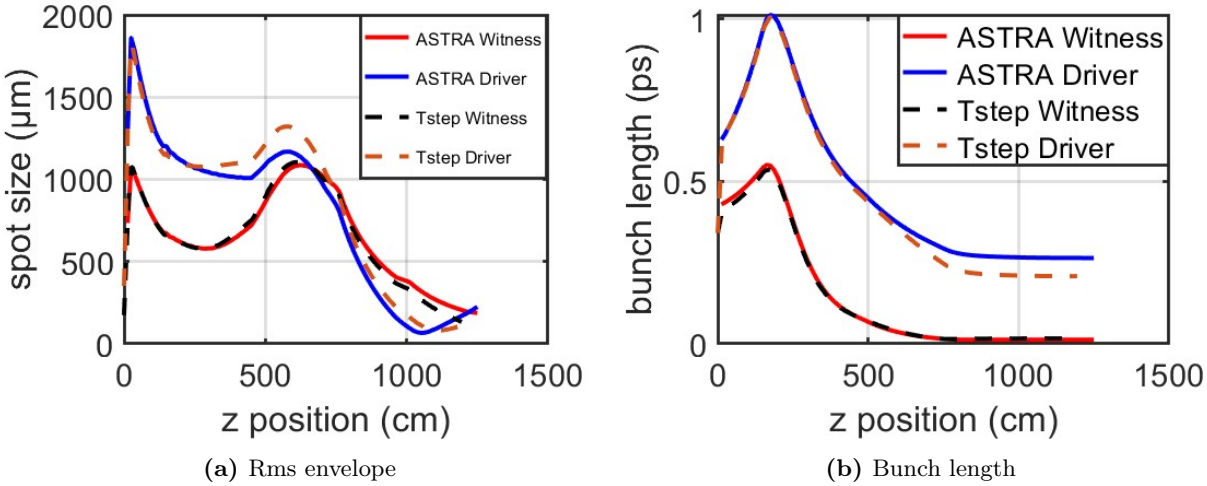

(a) Rms envelope

(b) Bunch length

Figure 3.7: ASTRA and TStep comparison; (a)ASTRA vs TStep Beams rms envelope, in this configuration the witness transverse dynamics is the same for the two codes. The driver is over-focused in the second velocity bunching structure. (b) ASTRA vs TStep bunch length, witness longitudinal dynamics is the same, the driver shows a different behavior after the second velocity bunching structure.

where the witness one is higher, 2 KAs respect to the 1,6 KAs obtained with TStep. As shown

also in Figures 3.7 (a)and 3.7(b), the simulations reveal differences in the behavior of the comb beam between the two codes. These differences arise from variations in how each code handles charge extraction from the cathode, space charge effects, and the reference particle settings for the comb beam. One of the primary distinctions lies in ASTRA's use of an adaptive longitudinal grid mesh along the photo-injector, which TStep does not incorporate. Due to this adaptive grid, we adjusted the initial beam length at the cathode in the two codes to achieve consistent final results. Consequently, the beam length in ASTRA was set approximately 20% shorter than in TStep. Another challenge encountered was defining a unique RF phase for the elements in both codes. This difficulty arises because each code employs a different statistical approach to setting the reference particle distribution. The beam dynamics in the velocity bunching regime are particularly sensitive to variations on the order of 0.1 degrees (Fig 3.8), which necessitated careful alignment between the two simulation frameworks. After several iterations and fine-tuning, we achieved the following

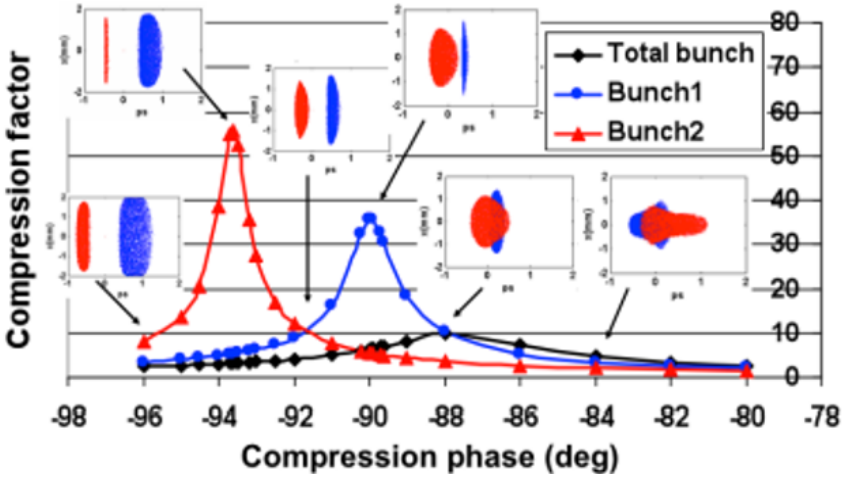

Figure 3.8: VB sensitivity on RF compression phase variation [34]. The blue and red curves represent the compression of the single beams, and the black one is the compression curve of the comb.

parameters 3.6. However, the bunch separation was less than optimal, 0.27 ps instead of the desired

Parameter	Witness Beam	Driver Beam
Emittance (mm-mrad)	1.00	1.46
Energy (MeV)	128	130
Energy Spread (%)	0.12	0.47

Table 3.6: Beam parameters after fine-tuning.

0.5 ps. The required separation between the beams is closely related to the plasma density used in the accelerator. Specifically, for the EuPRAXIA@SPARC_LAB project, with a plasma density of 10^{16} cm^{-3}, the separation between the electron beams must correspond to half of the plasma wavelength. This results in a required beam separation of 0.5 ps with the plasma density reported in Fig 3.9. Achieving this precise separation is critical for the effective interaction between the drive and witness beams within the plasma, ensuring optimal acceleration conditions. This machine setup, while not perfect, provided a valuable starting point for further optimization using the GIOTTO algorithm. The subsequent optimization steps aim to refine these parameters further and enhance the overall performance of the system. GIOTTO is an advanced software tool designed

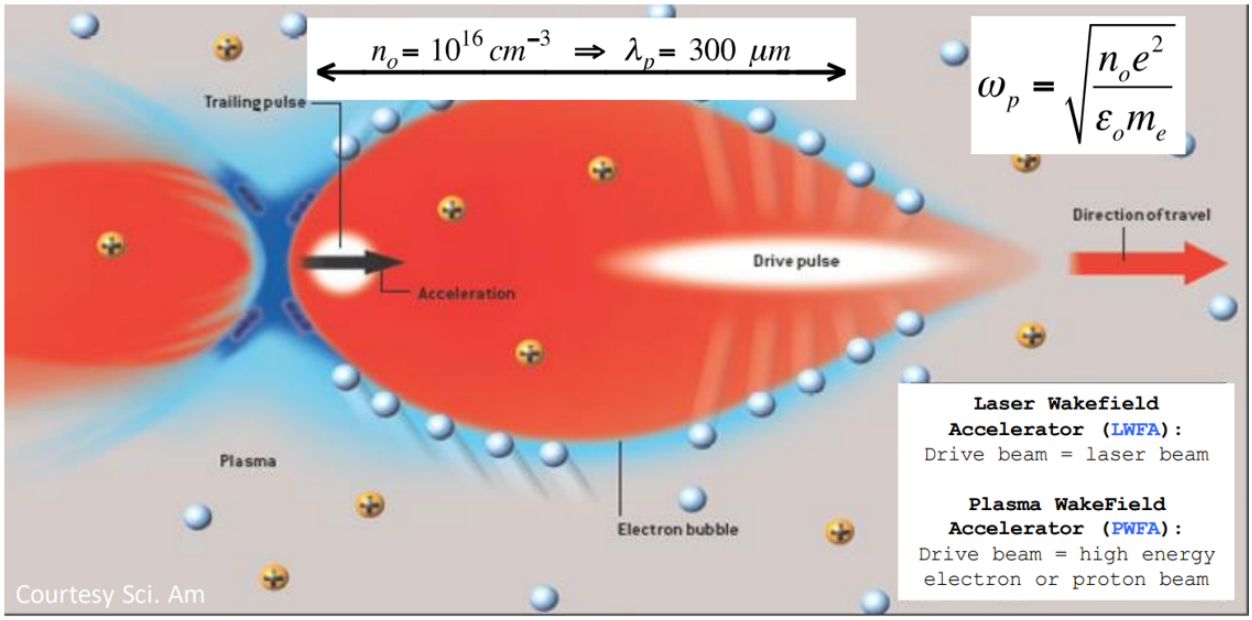

Figure 3.9: Conceptual drawing of a plasma wakefield accelerator. Considering the plasma density in the figure the matching condition for the plasma stage in terms of the driver-witness separation is guided by the plasma wavelength and must be half this parameter [35].

to optimize the performance of accelerator beamlines using a Genetic Algorithm (GA). Genetic Algorithms are a powerful computational method inspired by the process of natural selection, and they are particularly well-suited for tackling optimization problems where parameters are highly interdependent and nonlinearly correlated. These conditions are common in accelerator physics, especially when dealing with complex systems influenced by significant space charge effects, such as those found in high-brightness electron beam photo-injectors or when implementing the Velocity Bunching compression technique [33]. The GIOTTO software operates synergistically with the ASTRA simulation code, taking the configuration generated by ASTRA as an initial condition. This initial configuration serves as a baseline for further refinement. In this study, the ASTRA-generated setup, which includes a detailed arrangement of phases, gradients, and magnetic fields of the beamline elements, is fed into GIOTTO. GIOTTO then conducts a comprehensive parametric scan, adjusting key variables within the beamline elements and optimizing pulse shaping at the cathode to enhance beam quality and performance. The optimization process in GIOTTO is iterative and continues until the target values specified in its input file are achieved. These target parameters, which define the desired outcomes for the beamline performance, are summarized in Tab 3.5. The optimization focuses on improving the beam's transverse and longitudinal properties, minimizing emittance, and achieving the desired energy and energy spread. Upon completion of the optimization process, the results are documented in the GIOTTO output file. These results, presented in Tab 3.7, show that the final beam parameters have been brought into close alignment with the target parameters outlined in Tab 3.5. This alignment demonstrates the effectiveness of the optimization process and the capability of GIOTTO to fine-tune complex beam dynamics systems. Furthermore, the longitudinal and transverse bunch dynamics have been accurately modeled along the entire injector length (Fig 3.10 and Fig 3.11). The optimization conducted by GIOTTO involves not only refining the initial bunch distribution but also making significant improvements to the space charge routine. Moreover, the parameters of the beamline elements are adjusted based

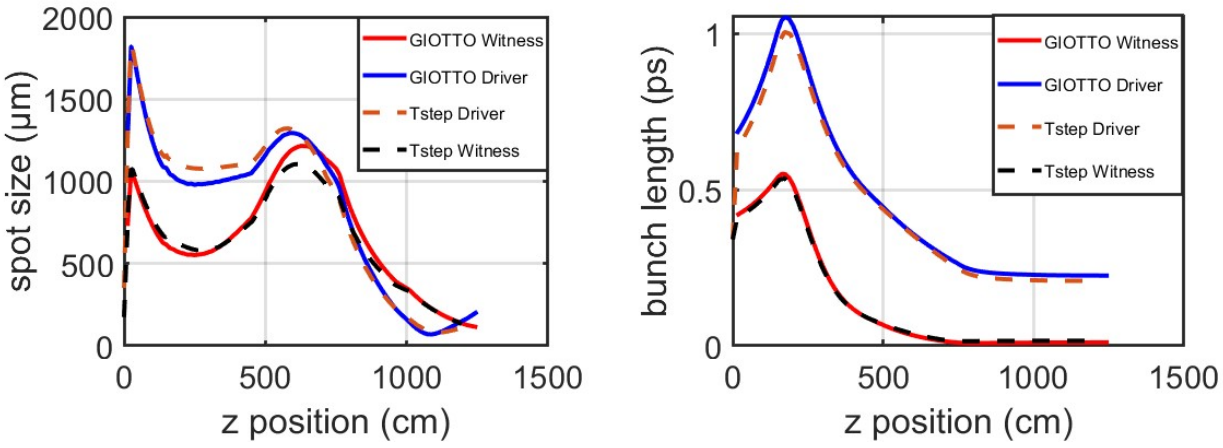

(a) Rms envelope **(b)** Bunch length

Figure 3.10: Beams parameters after GIOTTO optimization; (a) rms envelopes are now comparable with reference ones (Tstep), (b) bunch length achieves the desired value at injector exit.

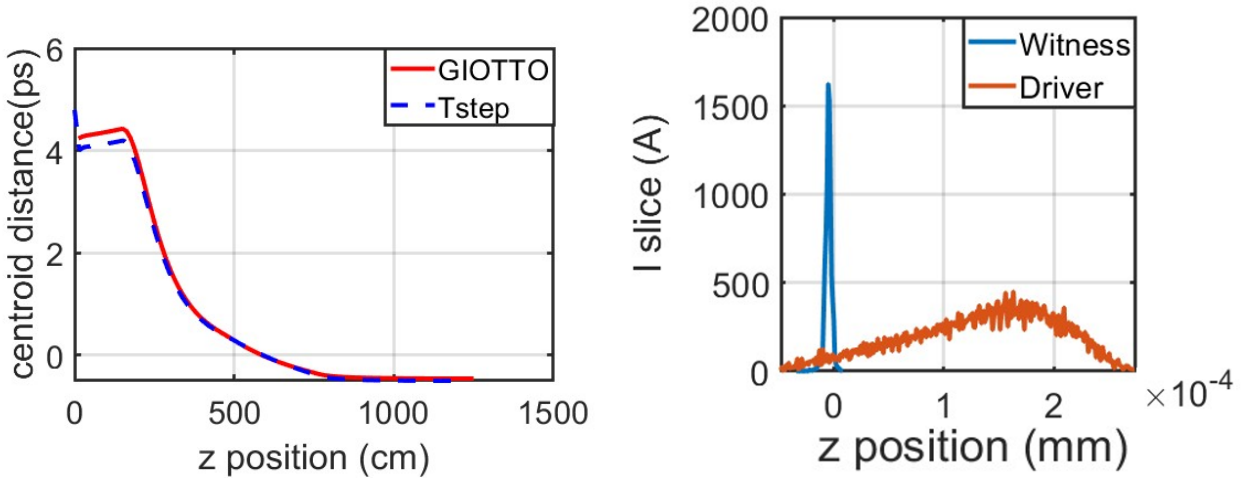

(a) centroid distance **(b)** peak current

Figure 3.11: Beams parameters after GIOTTO optimization;(a) witness peak current 1.6 kA that means ultra-short high brightness witness beams (b)time separation of the two bunches is 0.5 ps as required from the plasma $\sim 0.5ps$.

Table 3.7: Injector Exit Parameters Optimized with GIOTTO

Injector Exit Parameters	Witness	Driver
Spot Size	0.123 mm	0.174 mm
Bunch Length	3.2 μm	67.5 μm
Emittance	0.49 μm	1.69 μm
Energy	125.54 MeV	127.52 MeV
Energy Spread	0.33 %	0.61 %
Bunch Separation	0.46 ps	–
Peak Current	1.6 kA	–

on insights gained from the benchmark simulations. This ensures that the final setup not only meets but exceeds the performance criteria established at the outset, resulting in an optimized

machine configuration. Overall, GIOTTO's integration with ASTRA exemplifies how cutting-edge computational tools can be leveraged to solve challenging problems in accelerator physics, paving the way for advancements in beamline design and operation. The use of the techniques described in Chapter Two coupled with simulative codes enabled the optimization of the comb beam dynamics for the EuPRAXIA@SPARC_LAB injector. Fig 3.12 shows an example of a comb beam evolving along the injector. This optimized comb beam was subsequently transported into the X-band accelerating sections and injected into the plasma stage. The importance of this study was to define a solid working point by comparing the results obtained from two well-known simulation codes in the accelerator physics landscape. In addition, the generated beam was used for numerical stability studies for the beam-driven working point of EuPRAXIA@SPARC_LAB. The numerical scans are conducted within the framework of a start-to-end simulation. The input bunch used for these simulations is derived from previous comprehensive numerical analyses of the RF photoinjector system, carried out using the TStep, Elegant, and ASTRA codes. These simulations are based on the most recent layout of the EuPRAXIA@SPARC_LAB facility [36]. In this study, the numerical scans are executed across four distinct working points to evaluate performance under varying conditions. The plasma channel, which plays a crucial role in the acceleration process, is modeled using the hybrid fluid-kinetic code Architect [37]. The plasma channel profile is designed with an injection ramp followed by a flat top. The injection ramp is characterized by a squared cosine shape, which increases from zero up to the nominal flat top density over a distance of 1 cm. To optimize performance, the nominal plasma density is varied within a specified range of 0.9×10^{16} cm^{-3} to 1.4×10^{16} cm^{-3}. This density range is systematically scanned to identify the optimal conditions for achieving the best acceleration performance. More details can be found in the reference paper [38].

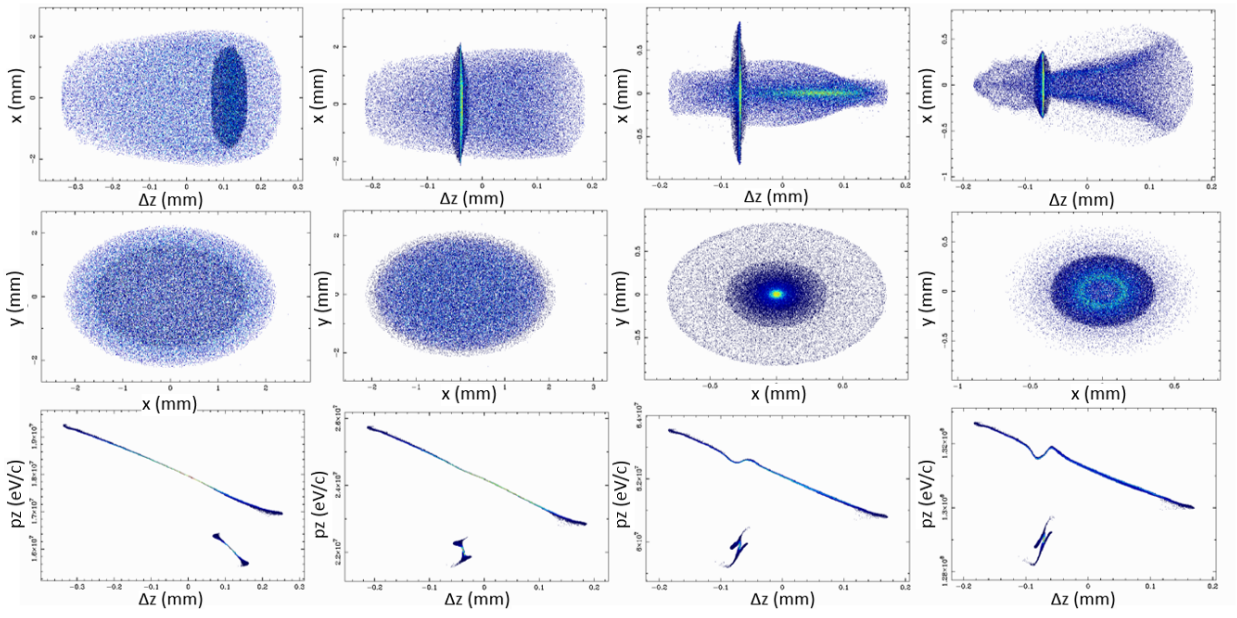

Figure 3.12: Evolution of spot size (first row), longitudinal phase space (second row), and footprint (third row) of a comb beam along the EuPRAXIA@SPARC_LAB injector. The simulation has been done with ASTRA simulation code.

3.3 Injector jitters and Witness Energy Gain in Plasma Wakefield Acceleration

Jitter in a linear accelerator refers to undesirable temporal variations that can have many causes and significant negative effects on the accelerator's performance. Accurate measurement and mitigation of jitter are essential to ensuring the efficiency and precision of linear accelerators. The types of jitter include:

- Phase jitter: Variations in the phase of the RF fields that accelerate the particles.
- Amplitude jitter: Variations in the amplitude of the RF fields.
- Timing jitter: Variations in the synchronization times between different components of the accelerator.

Jitter can originate from several sources, including:

- Instability of RF sources: RF sources such as magnetrons or klystrons can have intrinsic instabilities that cause phase and amplitude jitter.
- Mechanical vibrations: Vibrations can come from factors such as cooling systems and affect the position of the accelerating structures.
- Power supply fluctuations: Power supply variations can impact electronic devices' performance and RF sources.

Jitter can significantly impact the performance of accelerators in several ways. It causes beam dispersion, as particles fail to arrive at the target simultaneously, leading to a loss of beam focus. Temporal variations in the accelerating fields due to jitter can reduce the average energy of accelerated particles, thereby lowering the efficiency of energy transfer from RF sources to the beam. To measure jitter effectively, i.e. ps scale RF phase and 0.1% RF voltage jitters, various instruments and techniques are employed. High-speed oscilloscopes, i.e. GHz bandwidth, GS/s sampling rate, and ps rise time, enable the visualization and measurement of temporal variations in RF signals, while spectrum analyzers provide insights into fluctuations in signal frequency and amplitude. High-resolution, the ability to capture and reconstruct fine details of a signal with high precision in amplitude and timing, sampling techniques are also used to collect detailed temporal data on jitter. Mitigating jitter requires a multifaceted approach. Stabilizing RF sources through improved design or feedback circuits helps maintain phase and amplitude stability. Mechanical vibrations can be reduced with isolation systems, and advanced thermal control systems ensure stable temperatures in critical components. The use of low-noise electronic components and shielding techniques minimizes electronic noise in control circuits, while finely regulated power supplies reduce power fluctuations. Research and development in linear accelerators continue to address jitter reduction through advanced control techniques, including sophisticated algorithms for RF signal stabilization, and optimizing the accelerator configurations to be less sensitive to jitter. In PWFA, the precise control of the distance between the driver and witness beams is critical for maximizing the energy gain of the witness particles. This control can be affected by timing jitter, particularly from RF systems used in the acceleration process. Let's explore the correlation between the driver-witness

distance jitter and the energy gain of the witness particles. In PWFA, a high-energy driver beam travels through a plasma, creating a wakefield - a disturbance that can accelerate a trailing witness beam. The energy gain of the witness beam depends significantly on its position relative to the plasma wave generated by the driver beam. Distance jitter refers to the fluctuations in the spatial separation between the driver and witness beams due to timing variations. In RF-based acceleration systems, these variations can be introduced by:

- **RF Timing Jitter**: Inconsistencies in the RF phase and amplitude, which affect the synchronization of the laser arrival time and the rf system.
- **Laser Jitter**: In systems where lasers are used to generate the beam, fluctuations in the laser timing can also introduce jitter.

The energy gain of the witness beam is maximized when it is optimally phased with the plasma wave, typically at the peak of the wakefield. Timing jitter affects this phasing, leading to:

- **Phase Slippage**: If the witness beam arrives too early or too late relative to the optimal phase, it experiences reduced acceleration forces.
- **Energy Spread**: Variations in the phasing can lead to energy spread within the witness beam, reducing beam quality and focus.
- **Non-linear Effects**: Significant jitter can introduce non-linear interactions between the witness beam and the plasma wave, causing instability in the acceleration process.

The energy gain ΔE of the witness beam can be expressed as a function of its phase ϕ relative to the driver-induced wakefield:

$$\Delta E = qE_0 \cdot \sin(\phi)d, \tag{3.19}$$

where E_0 is the peak amplitude of the longitudinal electric field of the wake and d is the distance traveled by the witness particle in the accelerating region of the wake. Variations in ϕ due to timing jitter affect the energy gain according to the sine function, leading to sinusoidal energy variations. If the timing jitter is characterized by a Gaussian distribution, the resulting energy spread can be modeled statistically. The standard deviation of the energy spread σ_E can be related to the timing jitter σ_t and the frequency of the plasma wave f:

$$\sigma_E = qdE_0 \cdot \cos(\phi) \cdot 2\pi f \cdot \sigma_t \tag{3.20}$$

This expression shows how even small timing fluctuations can lead to significant variations in the energy spread, especially if the witness beam is not optimally phased. The mitigation techniques are:

1. **Improved RF Synchronization**: Enhancing the precision of RF systems can reduce timing jitter, ensuring better synchronization between the driver and witness beams.
2. **Feedback Systems**: Real-time feedback and correction systems can adjust the timing of the beams based on measurements of their relative position, minimizing jitter effects.

3. **Advanced photo-cathode Laser Systems**: For PWFA, using more stable laser sources for the driver and witness generation with less than tens of fs timing jitter can improve synchronization. With the actual technology, the driver witness time of arrival jitter at the cathode is 20-30 fs.

The correlation between driver-witness distance jitter and witness energy gain in PWFA is critical for optimizing beam performance [39][40]. The optimal distance between the driver and the witness $d\_\text{driver-witness} = \frac{\lambda_p}{2}$ is where the witness beam resides in the strongest acceleration zone of the wakefield. The optimal position produces a narrow energy spread because particles in the witness beam experience uniform fields, off-phase position causes non-uniform acceleration, leading to an energy spread within the beam and potentially compromising focus and usability. By understanding and controlling timing jitter, we can enhance the energy gain and quality of witness beams, leading to more efficient and precise particle acceleration. Studies have been carried out at SPARC_LAB to characterize both numerically and experimentally the time-jitter effects. In addition to the jitter introduced earlier, the comb-beam-based work point introduces other sources of jitter, such as timing errors between the driver and witness beams, fluctuations in the phase of the plasma wakefield, and misalignment of the beam focusing optics. These variations can lead to discrepancies in the acceleration gradient, adversely affecting the efficiency and stability of the plasma wakefield acceleration process. Moreover, the phase stability of the comb beam, which is critical for optimal synchronization, can introduce further uncertainties in the positioning of the witness beam relative to the accelerating wakefield, ultimately impacting the beam quality and energy spread. Compression with velocity bunching links the jitter in the beam's position to the RF system's timing jitter, affecting the longitudinal beam dynamics. The beam arrival timing jitter (ATJ) is influenced mainly by two factors: changes in the laser arrival time at the photocathode and instabilities in the RF system's timing. Other contributions, like fluctuations in the magnetic fields, are negligible. Therefore, the primary ATJ sources are the laser photocathode and the two S-band klystrons, named K1 and K2. K1 feeds the gun, while K2 feeds the first two sections, S1 (used for beam compression) and S2. The sum of all contributions gives the variation in beam arrival time:

$$\Delta t_{\text{linac}} \approx \sum_{i=1}^{3} c_i \Delta t_i \tag{3.21}$$

where $i = 1$ refers to the laser photocathode, $i = 2$ refers to K1, and $i = 3$ refers to K2. After the linac exit, the coefficient c_3 related to the S1 fields is much larger than c_1 and c_2, making it the leading contribution to the beam arrival timing jitter [41]. The ATJ in the relative distance between the driver and witness results in jitter in the witness energy when accelerated in plasma. The driver excites a wakefield with a slope that depends on the plasma density. Since the witness jitters in position along the wakefield, it will experience a different accelerating gradient, resulting in varying energy gains. The experimental setup at the SPARC LAB test facility is depicted in Fig 3.13. The witness beam is accelerated using a plasma accelerator, which consists of a discharge capillary that is 3 cm long and 1 mm in diameter, filled with hydrogen. The plasma within this capillary has a measured density of $n_e \approx 10^{15} - 10^{16}\,\text{cm}^{-3}$. For beam diagnostics, electro-optical sampling is performed before the plasma accelerator, while a magnetic spectrometer is used after the plasma [43]. This setup allows for detailed longitudinal characterization of the beam, facilitated by two

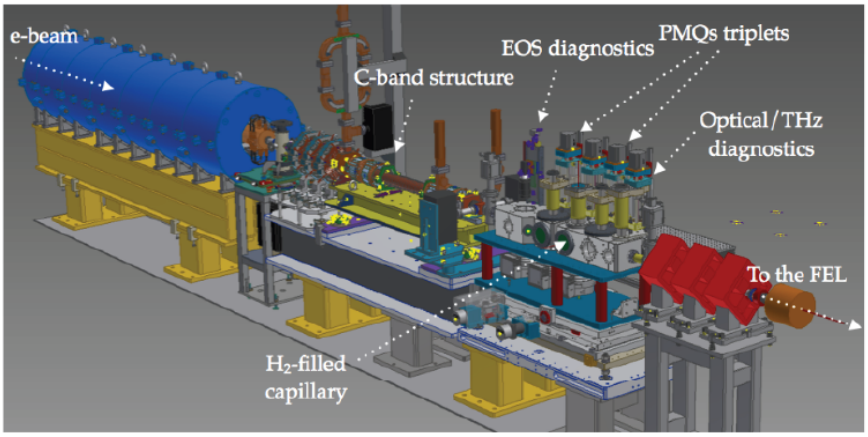

Figure 3.13: Layout of the experimental setup [42]. For the beam diagnostics,electro-optical sampling is performed before the plasma accelerator, while a magnetic spectrometer is used after the plasma.

Ce:YAG (Cerium-Doped Yttrium Aluminum Garnet) scintillator screens. In this setup, the plasma is stabilized using a laser pulse. Consequently, any timing jitter observed in the beam bunches is primarily due to RF system instabilities [44]. The electro-optical sampling allowed to measurement of a jitter in the order of a few tens of femtoseconds. The results showed a linear correlation between the relative jitter in the distance driver witness and the witness energy jitter (Fig 3.14). The SPARC

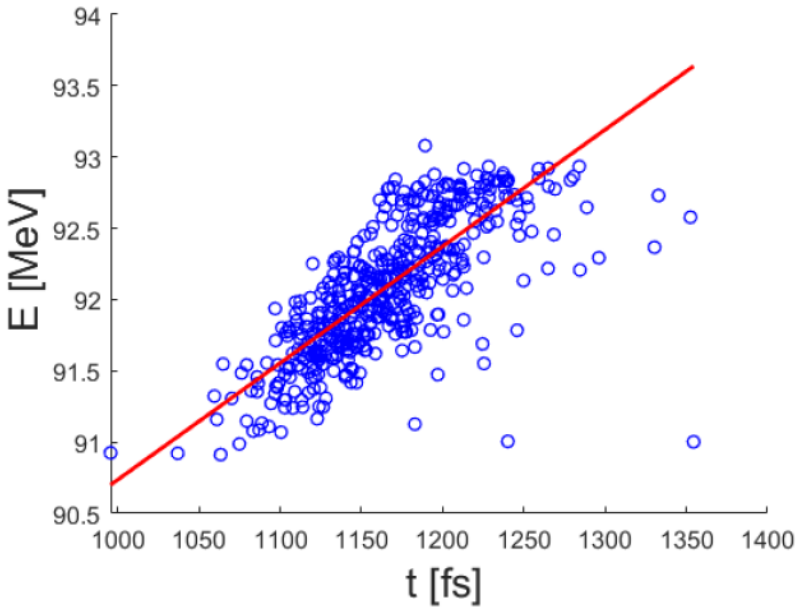

Figure 3.14: Measurement with the corresponding linear fit of the correlation between the distance driver-witness and the witness energy after the plasma [40].

test facility has been used as a reference and a testing ground for the optimizations implemented in the photoinjector of EuPRAXIA@SPARC_LAB. To complement the study on the generation and optimization of a high-brightness comb beam for the EuPRAXIA@SPARC_LAB injector, a systematic study on machine jitter and how the high-brightness parameters of interest are affected. The study also revealed which jitters most affect the stability of the comb beam. This study focuses on a comprehensive analysis of injector jitter, a key factor that influences machine stability, particularly in relation to Radio Frequency and laser jitters. The stability and reproducibility of the

electron beam are primarily governed by the RF generation system, which drives the accelerating structures and determines the timing and energy of the beam. Given the critical importance of this system, a significant portion of PhD study is devoted to investigating the sensitivity of the entire RF injector chain to jitter. The investigation begins with an assessment of jitter in the cathode beam parameters, such as variations in charge, spot size, and bunch separation. These parameters are crucial, as they directly affect the initial conditions of the electron beam as it enters the accelerator. Variations in these parameters can lead to beam instabilities, which may manifest as energy spread, emittance growth, or temporal mismatches at later stages in the accelerator. An X-band High Harmonic Cavity (HHC) is employed to counteract these potential instabilities and enhance beam stability [45][46][47]. The HHC is designed to pre-correct the longitudinal phase space of the electron bunch before it undergoes further acceleration. This correction process involves compressing and flattening the charge distribution along the length of the bunch, thereby reducing the longitudinal emittance and enabling more precise control of the beam's temporal structure. The implementation of the HHC allows for fine-tuning of both the longitudinal and transverse beam parameters at the photoinjector exit. This is critical for ensuring that the beam meets the stringent requirements for downstream acceleration, particularly in plasma-based stages, where even minor deviations can lead to significant performance degradation. Overall, the findings from this study are expected to provide valuable insights into the optimization of RF injector systems, contributing to the development of more stable and reproducible electron beams for the EuPRAXIA@SPARC_LAB facility.

3.3.1 Jitter compensation and working point improvement with a High harmonic X-band cavity

Beam stability is an important aspect of particle accelerator operations, crucial for maintaining precision in particle physics experiments. Enhancing this stability can lead to significant improvements in overall accelerator performance. The beam's stability could be enhanced by integrating a HHC. This device is specifically designed to pre-correct the bunch's Longitudinal Phase Space (LPS), optimizing the charge distribution to be both shorter and flatter. This optimized LPS allows for precise manipulation of the beam, enabling it to achieve the desired transverse and longitudinal parameters. A proposed solution to implement this correction involves the use of an X-band (11.99424 GHz) SW RF structure. This structure is strategically placed between the electron gun and the first accelerating structure, serving as an intermediary to manipulate the LPS. The mechanism of low-energy linearization in the velocity bunching regime differs significantly from the high-energy linearization systems typically employed before compression by a magnetic chicane (MBC). In the VB regime, linearization is achieved through careful manipulation of the RF phase to decelerate portions of the bunch, leading to compression as the bunch passes through the RF structure. This process is intrinsically linked to the initial beam energy and space charge effects, which play a much more significant role at lower energies. In contrast, high-energy linearization systems, such as those used prior to MBC, rely on higher harmonic RF cavities to correct nonlinearities in the lLPS that are introduced during the acceleration process. These systems operate at energies where space charge forces are negligible, allowing for a more straightforward application of linearization techniques that focus on fine-tuning the energy-time correlation without the complications introduced by strong space charge effects. As a result, the VB regime's approach to linearization requires different considerations and strategies compared to those used in MBC-based compression schemes.

The main differences are:

1. **Mechanism of Compression:**

- **Magnetic Bunch Compression (MBC):** MBC relies on a magnetic chicane, where the electron beam passes through a series of dipole magnets that create a path length difference between electrons of different energies. Higher-energy electrons travel a shorter path, catching up with lower-energy ones, effectively compressing the bunch longitudinally. MBC is typically used at higher beam energies.

- **Velocity Bunching (VB):** VB, on the other hand, is an RF-based technique where the beam is injected into an accelerating structure at a phase that initially decelerates the tail of the bunch while accelerating the head. This causes the bunch to compress as the tail catches up with the head within the RF field. VB is more effective at lower energies.

2. **Space Charge Effects:**

- **MBC:** In MBC, space charge forces are generally negligible due to the high energy of the beam. At high energies, the relativistic factor reduces the impact of these forces, allowing the bunch to be compressed without significant emittance growth or other distortions.

- **VB:** In VB, space charge forces play a significant role, especially at lower energies. These forces can counteract the bunch compression and lead to emittance growth if not properly controlled. The interaction between space charge forces and the RF field must be carefully managed to avoid compromising beam quality.

3. **LPS Distortion:**

- **MBC:** MBC primarily focuses on linearizing the energy-time correlation in the beam, ensuring that the bunch compresses uniformly without introducing significant distortions to the longitudinal phase space (LPS). The linearization in MBC is typically achieved using higher-harmonic cavities, which correct nonlinearities introduced by the RF structures and also during the magnetic compression with the chicane.

- **VB:** In VB, the situation is more complex. While there is an aspect of linearization, the process inherently distorts the LPS due to the combination of deceleration and space charge effects. The degree of linearization in VB is not solely determined by harmonic correction but is also influenced by the extent of deceleration applied to the bunch. As the X-band phase is adjusted, the degree of deceleration affects the compression, with greater deceleration leading to more effective compression but also more significant LPS distortion.

4. **Trade-offs in Deceleration and Emittance Compensation:**

- In VB, there is a delicate balance between achieving maximum bunch compression and maintaining low emittance. Greater deceleration in the VB stage results in better compression but at the cost of emittance compensation. This is because increased deceleration enhances the space charge forces and the distortion of the LPS, making it harder to preserve the emittance of the beam. Consequently, operators must carefully tune the X-band phase and the degree of deceleration to achieve the desired compression while minimizing emittance degradation.

Velocity bunching plays a crucial role in dynamically shifting the peak current to the tail of the distribution, effectively compressing the electron beam in the longitudinal direction. However, it can also introduce phase space distortions that may lead to beam quality degradation if not properly managed. This is where the X-band cavity becomes useful. Positioned strategically within the injector, the X-band cavity serves to center the peak current by applying a corrective force to the beam's longitudinal phase space. Downstream of the drift, the bunch enters a short, 11 cm, X-band cavity that decelerates it by 1.27 MeV. This deceleration to lower energy has several important effects [45]:

1. It enhances longitudinal space charge effects, even as longitudinal laminarity decreases, facilitating faster compression.
2. It shifts the current spike toward the tail of the bunch resulting in a more uniform charge distribution at the end of compression.
3. It provides a pre-compression phase before the velocity bunching compression.
4. It enlarges the envelope, because of the deceleration, thereby relaxing transverse space charge effects.
5. It applies a pre-correction to the radio frequency curvature of the accelerating structures.
6. The deceleration, energy reduction, leads to greater bunch slippage with respect to the RF phase, which is crucial for the voltage breakdown technique.

In essence, the velocity bunching mechanism works in tandem with the X-band cavity to maintain a well-formed current profile. The X-band cavity's role in refining the longitudinal dynamics ensures that the beam remains stable, at least with the same stability as the solution without the HHC and optimized in terms of transverse and longitudinal parameters for downstream processes, particularly in high-precision applications, like PWFA, where even minor instabilities can lead to significant performance losses. The X-band RF cavity characteristics are reported in Tab 3.8 Fig 3.15 and Fig 3.16. Taking into account the relevance of jitters in RF photoinjectors, a comprehensive sensitivity

Table 3.8: X-Band Parameters

X-Band Parameter	**Value**
Resonant Frequency	11.9942 GHz
Electric Field (E_{acc})	20 MV/m
Peak Electric Field (E_{peak})	38 MV/m
Number of Cells	7
Length	11 cm
Radius	4 cm

jitter study has been conducted for all RF injector components, comparing the beam stability results both with and without the inclusion of the X-band cavity. Given that the velocity bunching regime is highly sensitive to RF phase fluctuations (Fig 3.8), the X-band cavity is proposed to stabilize the electron beam against these RF jitters. In this initial part of the study, RF jitters were simulated

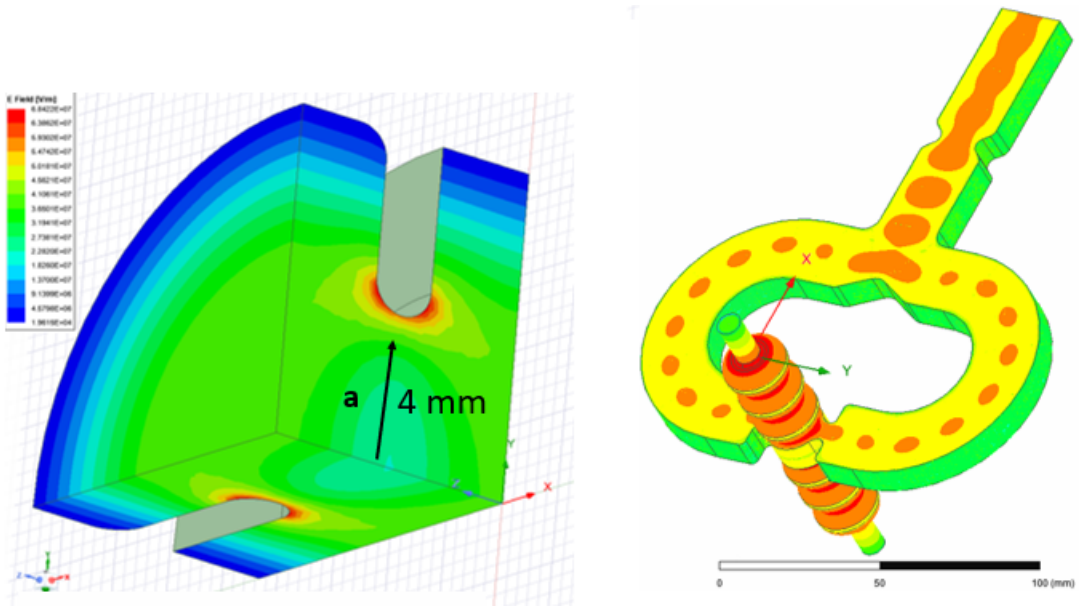

(a) One-quarter structure **(b)** Power splitter

Figure 3.15: Electric field rendering of One-quarter structure (a) and the full cavity with the power splitter (b).

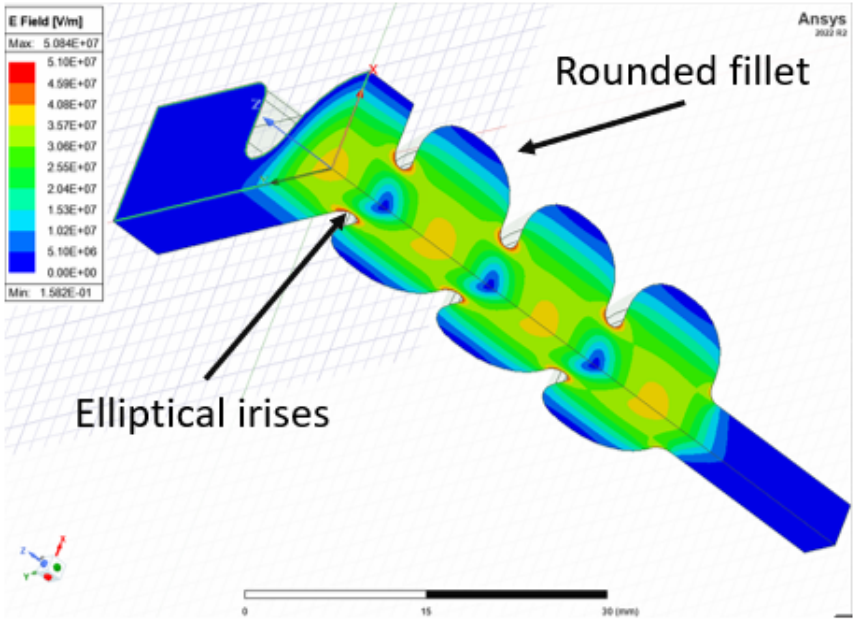

Figure 3.16: Ansys simulation of the X-band linearizer cavity

with a root mean square value of 30 fs for both the S-band and X-band phases (0.03 and 0.12 degrees), reflecting measurements taken at SPARC_LAB. The simulation results demonstrate that the X-band cavity effectively mitigates RF jitter-induced degradations in beam quality except for the witness bunch length (Fig. 3.18 and Fig. 3.19). Furthermore, the presence of the X-band cavity centers the witness peak current (Fig. 3.17a). As pointed out in Fig 3.17b, the temporal distance between the driver and the witness is also improved by removing the overlap between the driver's tail and the witness. Further analysis was performed by introducing additional sources of jitter, as summarized in Tab. 3.9. The stability of the beam under these compounded conditions was then

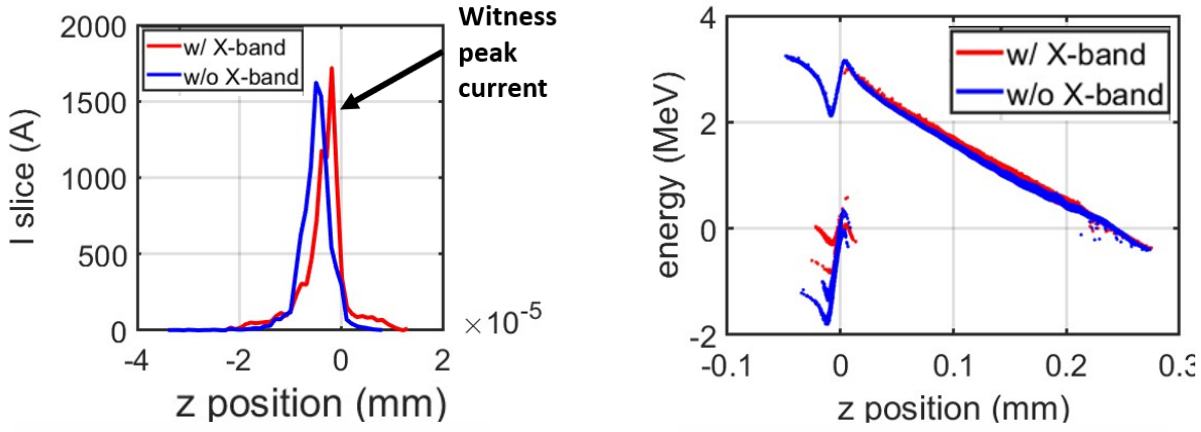

(a) Witness peak current w/ and w/o X-band HHC **(b)** LPS of the comb beam w/ and w/o the X-band HHC

Figure 3.17: symmetrization of current distribution (a) and improvement of the driver-witness bunch separation at the end of the injector (b).

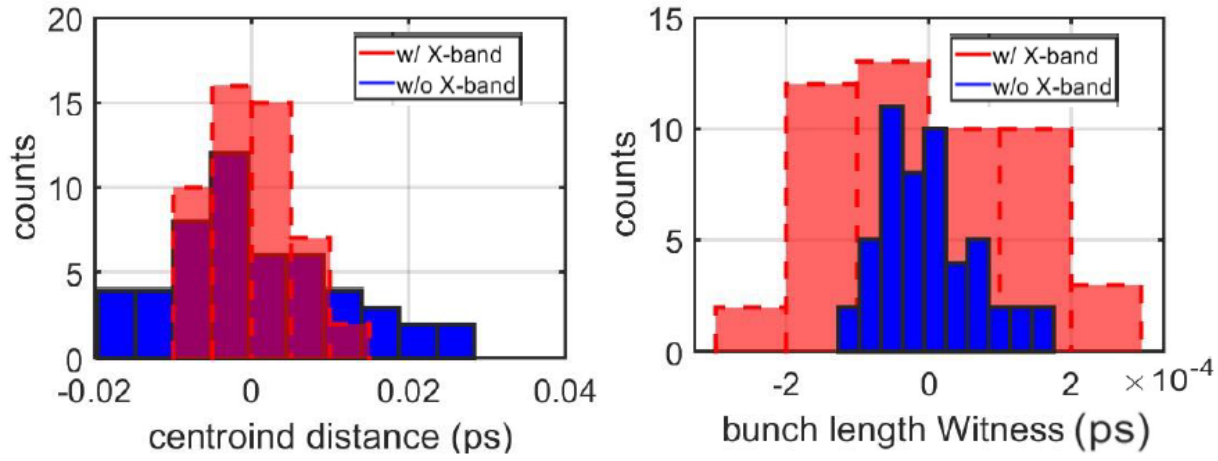

Figure 3.18: centroid distance (left) and witness bunch length (right) considering only RF phase jitters

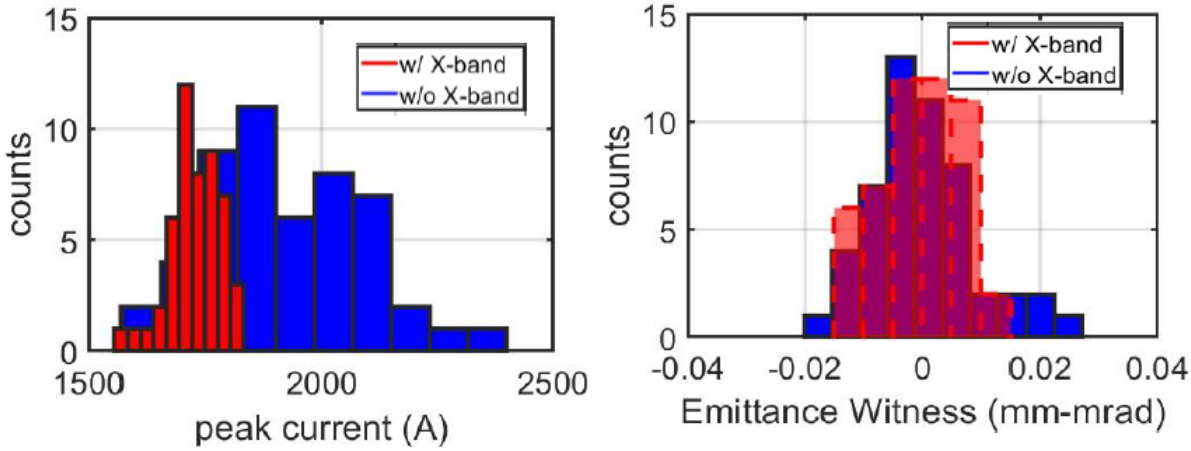

Figure 3.19: witness peak current (left) and witness emittance (right) considering only RF phase jitters

assessed, with results presented in Tab. 3.10. Specifically, the X-band cavity reduces the witness emittance jitter while maintaining the same separation jitter. Also the witness peak current jitter is worst. The comparative analysis (Fig. 3.18 and Fig. 3.19), highlights the differences in beam

Table 3.9: jitters value.

total charge	spot size	time of arrival @cathode	rf phase	voltage
2% of the total	1% of the total	30 fs rms	30 fs rms	0.1% of the total

Table 3.10: jitter analysis results. Jitters values are taken from Table 3.9 both Rf and all jitters

beam parameters	w/ X-band all jitter	w/ X-band Rf jitter	w/o X-band all jitter
witness emittance (mm-mrad)	0.672 ± 0.031	0.676 ± 0.013	0.5710 ± 0.091
witness bunch length (ps)	0.0137 ± 7e-4	0.0140 ±2e-4	0.0180 ± 7e-4
witness peak current (A)	1733 ± 230	1728± 56	1923 ± 173
bunch separation (ps)	0.5337 ± 0.0117	0.5462 ± 0.0048	0.5011 ± 0.0115

stability when considering only RF jitters versus the combined effects of all jitters (Fig. 3.20) listed in Tab. 3.9. This preliminary study wanted to emphasize the different contributions of jitter in this configuration before forwarding to a one-to-one comparison of the two configurations, with and without HHC. Up to now, the simulations have shown that the injector stability with and without

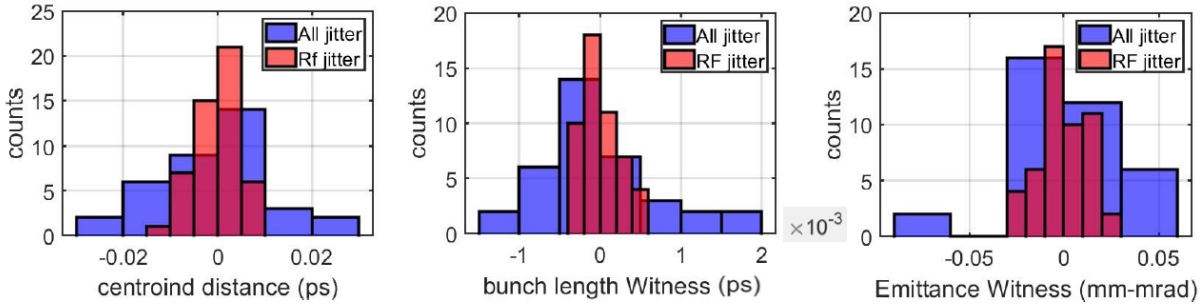

Figure 3.20: Comparison between only RF jitters and all jitters summarized in the table. Histograms show, in order, the comparison of bunch separation, witness bunch length emittance, and witness emittance

the HHC is approximately the same Tab. 3.10 first and last column. The next step of the study was to identify the most significant source of jitter and to evaluate a strategy to effectively improve the stability of the working point. The idea was to investigate which specific jitters in the machine parameters most significantly influenced beam stability. A systematic analysis was conducted, where each type of jitter was individually isolated and studied to assess its impact on the beam's stability. This individual analysis was then compared against the cumulative effect of all jitters combined. The goal was to identify the most critical sources of instability and to determine how much each jitter contributes to the overall degradation of beam stability (Fig. 3.21, 3.22, 3.23, 3.24). By comparing the different contributions of the jitter and combining them in various ways with the total jitter contribution, it was found that the most relevant parameter for beam stability is the jitter on the field amplitude of both X and S-band Fig. 3.24 (it was set to 0.1%), the contribution of the amplitude jitter on the bunch separation jitter shown in Tab. 3.10 has been estimated to be 5 fs.

The relevance of this jitter has been introduced in Section 2.3.2. This jitter critically influences the energy gain of the witness beam, as it determines the beam's position within the plasma bubble at any given moment. For stable acceleration within the plasma region, this separation jitter must be minimized to a value on the order of a few femtoseconds. Any deviation from this optimal timing can lead to significant fluctuations in the witness beam's energy gain, thereby compromising the overall stability and efficiency of the acceleration process. Assuming the approximation of constant beam

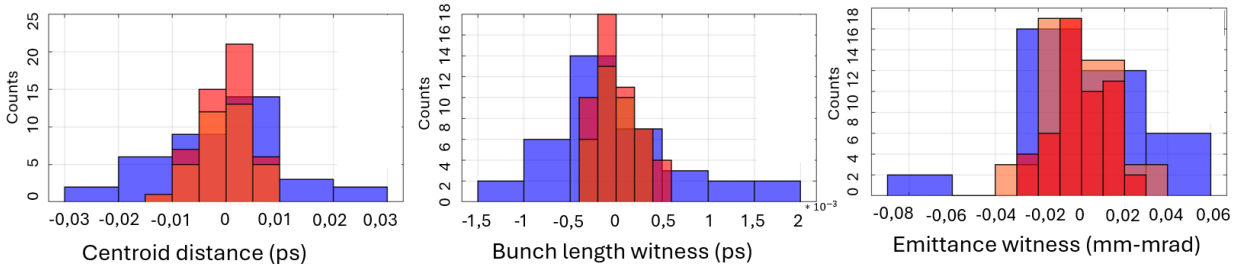

Figure 3.21: Comparison between only RF jitters (red), charge and RF (orange), and all jitters (blue) with the HHC. Histograms show the comparison of bunch separation, witness bunch length, and witness emittance

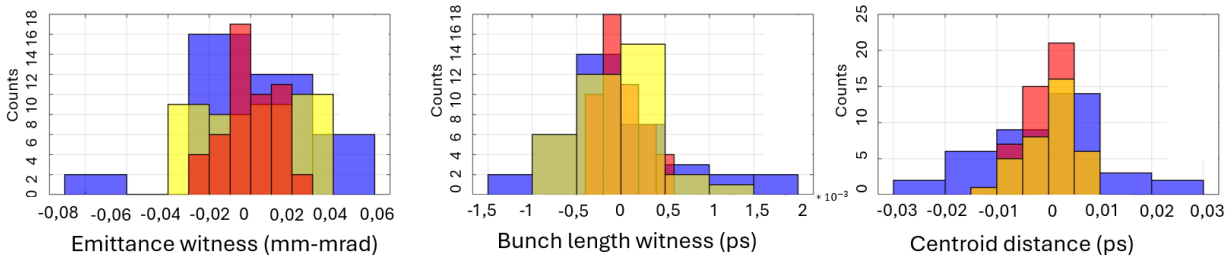

Figure 3.22: Comparison between only RF jitter (red), spot size and Rf (yellow), and all jitters (blue) with the HHC. Histograms show the comparison of witness emittance, witness bunch length, and bunch separation.

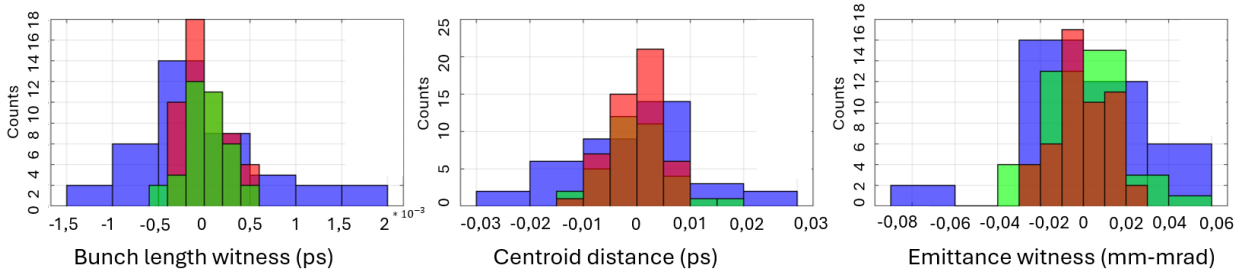

Figure 3.23: Comparison between only RF jitters (red), Time of arrival (green), and all jitters (blue) with the HHC. Histograms compare the witness bunch length of bunch separation and witness emittance.

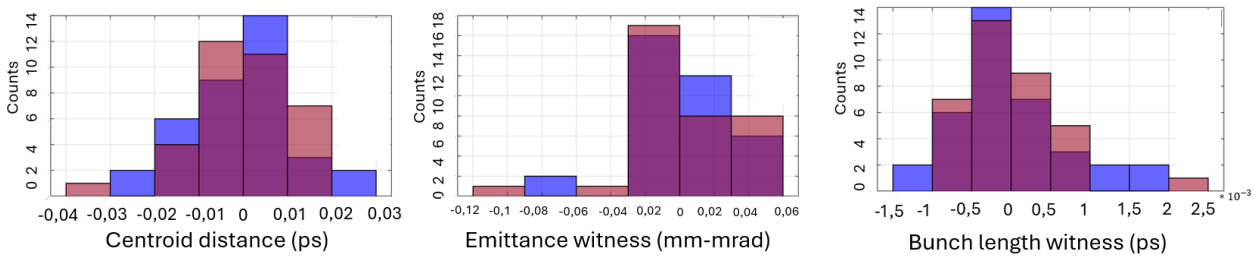

Figure 3.24: Comparison between only RF voltage (red) and all jitters (blue) summarized in the table with the HHC. Histograms show the comparison of bunch separation, witness emittance, and witness bunch length

loading in the plasma, we can derive a straightforward expression that describes the dependency of energy jitter on fluctuations in plasma density and bunch separation jitter. We consider a scenario involving a total blow-out with an immobile ion background under a one-dimensional approximation,

where no current flows inside the plasma bubble. In this context, Gauss's law simplifies to [38]:

$$\frac{\partial E_z}{\partial z} = \frac{e n_p}{\epsilon_0}, \tag{3.22}$$

where E_z represents the longitudinal electric field,n_p the plasma density and ϵ_0 the dielectric constant in vacuum . This electric field is influenced by both the blow-out region and the beam-loading effect induced by the witness beam, which slightly alters the shape of the plasma bubble. Nevertheless, equation (3.22) remains valid before and after the witness beam, implying that the slope of the electric field is constant outside the witness region. We assume ideal beam loading compensation, meaning that the electric field is flat within the witness region. Let z_0 denote the position of the zero-crossing of the electric field with respect to the driver beam and Δz the separation between the driver and witness beams. Under these conditions, the accelerating gradient is given by:

$$E_z \approx \frac{e n_p}{\epsilon_0}(\Delta z - z_0). \tag{3.23}$$

Next, we consider small perturbations in plasma density and bunch separation and evaluate their effects on the accelerating gradient experienced by the witness beam, leading to the following expression for the relative variation of the electric field:

$$\delta E_z = \frac{e}{\epsilon_0}(\Delta z - z_0)\delta n_p - \frac{e n_p}{\epsilon_0}\frac{\partial z_0}{\partial n_p} + \frac{e n_p}{\epsilon_0}\delta z. \tag{3.24}$$

For simplicity, we neglect the dependency of the zero-crossing position on plasma density. We further assume that, under realistic working conditions, the witness beam is positioned near the trailing edge of the plasma bubble, such that $\Delta z - z_0 \approx \lambda_p/2$. The resulting expression for relative beam energy jitter becomes:

$$\frac{\delta E}{E - E_0} = \frac{\delta E_z}{E_z} = \frac{\delta n_p}{n_p} + \frac{2\delta z}{\lambda_p}, \tag{3.25}$$

where E is the final energy and E_0 is the initial energy. For our setup, where $E = 2E_0$, this simplifies to [38]:

$$\frac{\delta E}{E} = \frac{\delta n_p}{2n_p} + \frac{\delta z}{\lambda_p}. \tag{3.26}$$

Utilizing this equation, and assuming no correlation between δn_p and δz, we can derive a stability requirement for the relative energy jitter of $< 1\%$, as specified in Tab. 3.2. For a working point with the characteristics of the EuPRAXIA setup, this implies that the plasma density fluctuation should be $\delta n_p \approx 10^{14}\,\mathrm{cm}^{-3}$ and the bunch separation jitter $\delta z \approx 1.5\,\mu\mathrm{m}$. This corresponds to a temporal jitter between the driver and witness beams of approximately δt of a few fs. However, given the current state of the injector, linac, and plasma density jitter, a 1% energy jitter is considered acceptable to maintain enough FEL performance. Recently, the LNF was awarded a regional grant for consolidating the SPARC_LAB facility under the SABINA project [48]. The Low-Level Radio Frequency (LLRF) system will undergo a comprehensive upgrade with digital systems provided by Instrumentation Technologies, Solkan, Slovenia (Libera LLRF). This upgrade will address several known limitations of the current system, including front-end noise floor issues, temperature stabilization to minimize drifts, and the capability for arbitrary pulse shapes. Identical systems have already been purchased and successfully commissioned for both LNF and external projects by the

LNF RF group; the measured amplitude and phase jitters are <0.02% and <0.01 degrees, respectively. The beam dynamics simulations I performed have set an upper limit on the maximum jitter of the RF stations at 0.02 degrees RMS for the S-band and 0.08 degrees RMS for the X-band HHC as shown in the previous analysis (Tab 3.10), a jitter larger than those values brings a driver-witness temporal distance jitter larger than 10 fs. Taking into account beam dynamics requirements and

Table 3.11: The final jitter values used in the simulations are based on actual measurements taken@SPARC_LAB.

total charge	spot size	RF phase S/X	voltage S/X
2%	1% mm	0.02/0.08 deg	0.02% rms

currently available measurement techniques, the final jitters simulated are listed in Tab 3.11. The Tab 3.12 summarizes all the contributions from various jitter sources combined, with the worst-case result being a driver-witness distance jitter of 3.9 fs (in agreement with analytical treatment), an improvement with respect to the case without the HHC, of 4.5 fs (Tab 3.13 Fig 3.25). Anyway, the design criteria Tab 3.2 specify an energy jitter of less than 1%, consistent with the simulations performed. This level of temporal jitter translates to a relative energy jitter of 0.5–1%. The final analysis highlights the benefits of the injector layout with the HHC. By considering the beam dynamics requirements in terms of machine jitter, we achieve two key advantages: a significantly clearer temporal separation between bunches (not achievable without this cavity and essential for the plasma requirement) and mitigation of this jitter, relevant for stable acceleration process in the plasma stage, while the introduction of an HHC get worse the working point in terms of emittance and witness bunch length jitters. From this analysis, it emerges that the high-harmonic cavity plays a crucial role in improving the working point by enhancing the achievable separation of comb beams, thereby achieving greater beam separation at the injector exit. Moreover, including this structure does compromise the stability of the working point in terms of other jitter taken into account but in a range considered acceptable. In conclusion, considering the advantages of increasing the driver-witness separation by reducing also this jitter, makes the HHC an essential element of the beamline. Working point with lower plasma density are already being studied, which allow for a greater separation and therefore operate on a more stable point of the overcompression curve.

Jitters (witness bunch)	**ϵ(mm-mrad)**	**Bunch separation(ps)**	**Bunch Length (ps)**
phase HHC, gradients S/HHC, charge	0.6611 ± 0.0190	0.5467 ± 0.0018	$0.0136 \pm 9.65 \times 10^{-5}$
phase HHC, gradients S/HHC	0.6619 ± 0.0132	0.5462 ± 0.0022	$0.0136 \pm 1.12 \times 10^{-4}$
All (no time of arrival)	0.6683 ± 0.0222	0.5460 ± 0.0037	$0.0138 \pm 3.8 \times 10^{-4}$
phases, gradients S/HHC	0.6693 ± 0.0165	0.5448 ± 0.0030	$0.0137 \pm 1.42 \times 10^{-4}$
phase HHC, gradients S/HHC, charge, spot	0.6698 ± 0.0220	0.5463 ± 0.0025	$0.0138 \pm 4.29 \times 10^{-4}$
All	0.6602 ± 0.0194	0.5469 ± 0.0039	$0.0132 \pm 3.5 \times 10^{-4}$
phase and gradient HHC	0.6576 ± 0.0042	0.5464 ± 0.0012	$0.0136 \pm 1.83 \times 10^{-5}$
phase, gradient S, spot, charge	0.6611 ± 0.0212	0.5458 ± 0.0029	$0.0136 \pm 3.5 \times 10^{-4}$

Table 3.12: Considering all the jitter sources and the different contributions of the beamline elements, the worst-case scenario results in a 3.9 fs bunch separation jitter. The jitters simulated are the ones in Tab 3.11.

Table 3.13: S-band injector jitter without the HHC.The jitters simulated are the ones in Tab 3.11.

injector	witness emittance	bunch separation	witness bunch length
S-band no HHC	0,5732 ± 0,0027 (mm-mrad)	0,46 ± 0,0045 (ps)	0,0185 ± 3,0e-4 (ps)

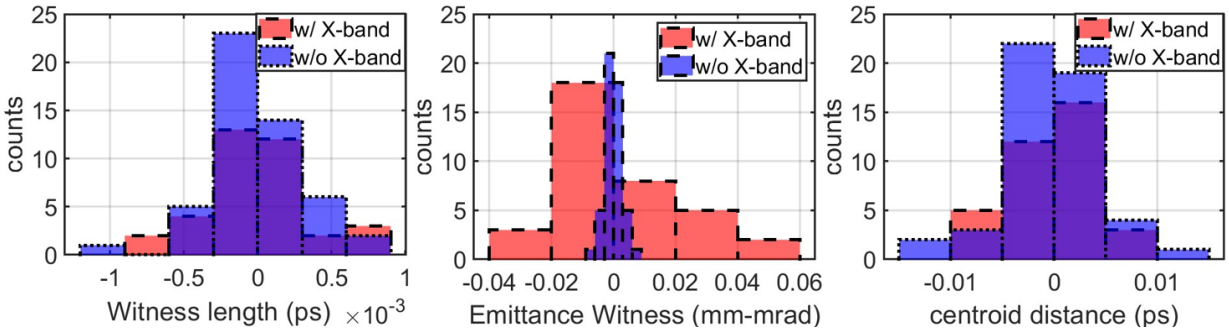

Figure 3.25: Comparison of the injector jitters w/ and w/o the HHC. The bunch separation jitter as mentioned in the text is improved on the contrary emittance and witness length jitter more.

3.4 Comb beam @SPARC_LAB and final focusing study

SPARC_LAB (Sources for Plasma Accelerators and Radiation Compton with Laser And Beam, Fig 3.26) is a test facility operating at the Frascati National Laboratories of INFN (LNF-INFN), dedicated to advanced radiation sources and innovative acceleration techniques. In recent years, the primary focus has been on plasma-based acceleration experiments, aiming to provide large accelerating fields—up to several GV/m—for high-quality electron beams with small energy spreads and normalized emittances[49]. These efforts culminated in the first demonstration of FEL lasing from a plasma-accelerated electron beam[50]. The R&D on plasma is further motivated by the EuPRAXIA Preparatory Phase project, which envisions the creation of the first-ever plasma beam-driven facility at LNF as part of the EuPRAXIA@SPARC_LAB test user facility. Additionally, recent regional and national funding aimed at enhancing the general capabilities of the SPARC_LAB test facility has facilitated upgrades to the accelerator and the addition of two new radiation sources for external users: one utilizing undulators to generate light in the THz range, [51] and the other based on betatron radiation in the soft X-rays from a plasma stage [52]. In this section, I will focus on photoinjector analysis and how high-brightness beams are generated for PWFA applications. Some techniques have been introduced in the previous paragraphs, now we will go into more detail in the physical discussion of the phenomena underlying beam generation (comb-like) for PWFA. SPARC_LAB is based on the combination of the high-brightness ($\approx 10^{15}$ A m^{-2} rad^{-2}) SPARC photo-injector [53] with the high-intensity ($\approx 10^{19}$ W/cm^2) FLAME laser [54]. The integration of these two systems has paved the way for exploring numerous plasma acceleration techniques, such as self-injection, external-injection, laser-driven, and beam-driven methods. This setup has also supported a broad array of interdisciplinary and cutting-edge research activities utilizing innovative radiation sources. These sources include FEL operating in both Self Amplified Spontaneous Emission and seeded configurations, as well as high peak power THz radiation, available in both broadband and narrow-band frequencies [55]. The SPARC photo-injector starts with a S-band (f_{RF} = 2.856 GHz) 1.6 cell RF-gun [56] providing 120 MV/m electric fields. Electrons are ex-

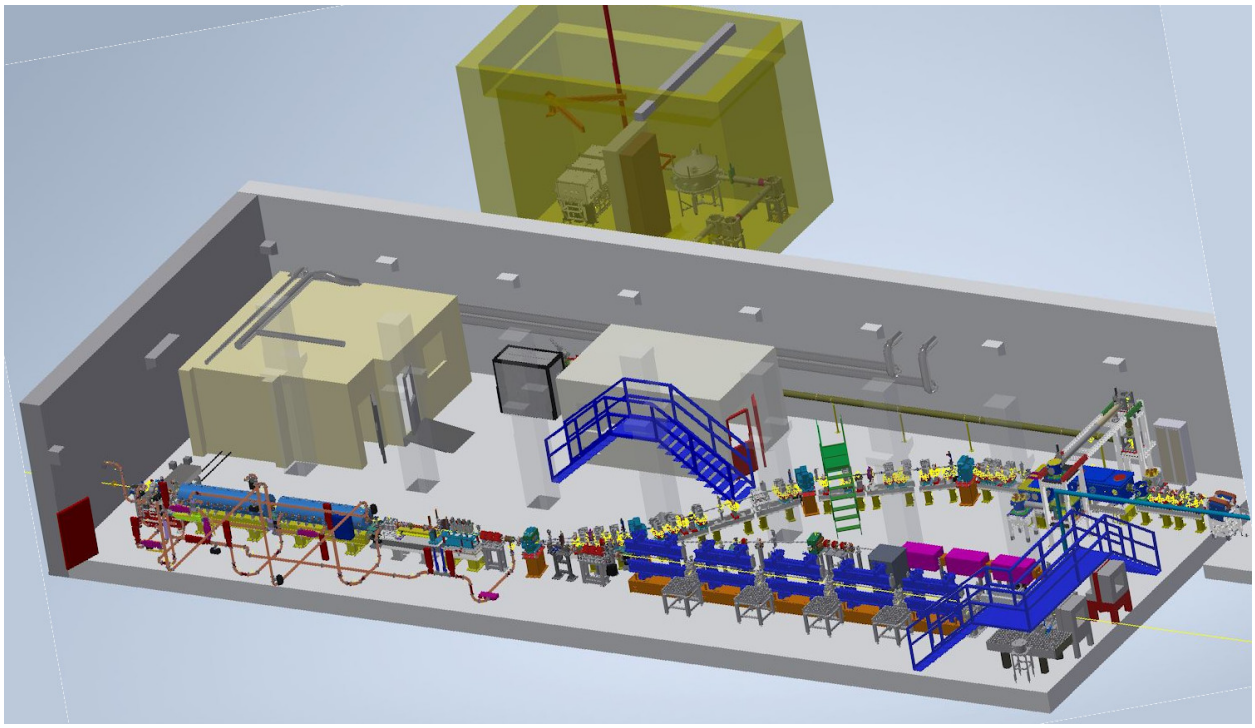

Figure 3.26: Layout of the SPARC_LAB test facility.

tracted from a copper (Cu) cathode using a UV laser ($\lambda_L = 266$ nm), whose shape and duration (0.1-10 ps) can be tailored according to the specific experimental activity. The electrons are accelerated up to 5.6 MeV in the gun and then injected into the linac consisting of two TW S-band structures and a TW one operating at C-band ($f_{RF} = 5.71$ GHz). The maximum achievable beam energy is approximately 180 MeV. The first TW section is also used as an RF-compressor by means of VB [19] Fig 3.27. Solenoid coils embedding the first two sections can provide additional magnetic focusing during the VB process and control of emittance and envelope oscillations [57]. The beam dynamics studies that have been conducted at SPARC_LAB concern the optimization of working points of interest for PWFA experiments. Among the most influential parameters for being able to inject an electron beam into a plasma accelerating section is the transverse dimension of the beam. The witness bunch must be much shorter than the plasma wavelength λ_p, and, for its optimal acceleration, it must be transversely matched to the plasma in terms of the Twiss β-function. In the blow-out regime, the equilibrium solution is [58]:

$$\beta_{\text{eq}} = \sqrt{\frac{\gamma}{2\pi r_e n_p}}, \tag{3.27}$$

with r_e being the classical electron radius and γ being the relativistic Lorentz factor. The condition expressed is difficult to fulfill especially for low energy beams. For instance, with $n_p \approx 10^{16}\,\text{cm}^{-3}$ and $\gamma \approx 200$, it is $\beta_{\text{eq}} \approx 1\,\text{mm}$ that corresponds to:

$$\sigma_r = \sqrt{\beta_{\text{eq}} \epsilon_n / \gamma} \approx 2\,\mu\text{m} \tag{3.28}$$

when assuming $\epsilon_n \approx 1\,\mu$m as normalized emittance. The focusing system at the SPARC_LAB linac before the plasma accelerating section consisted of a system of three permanent quadrupoles (PMQ)

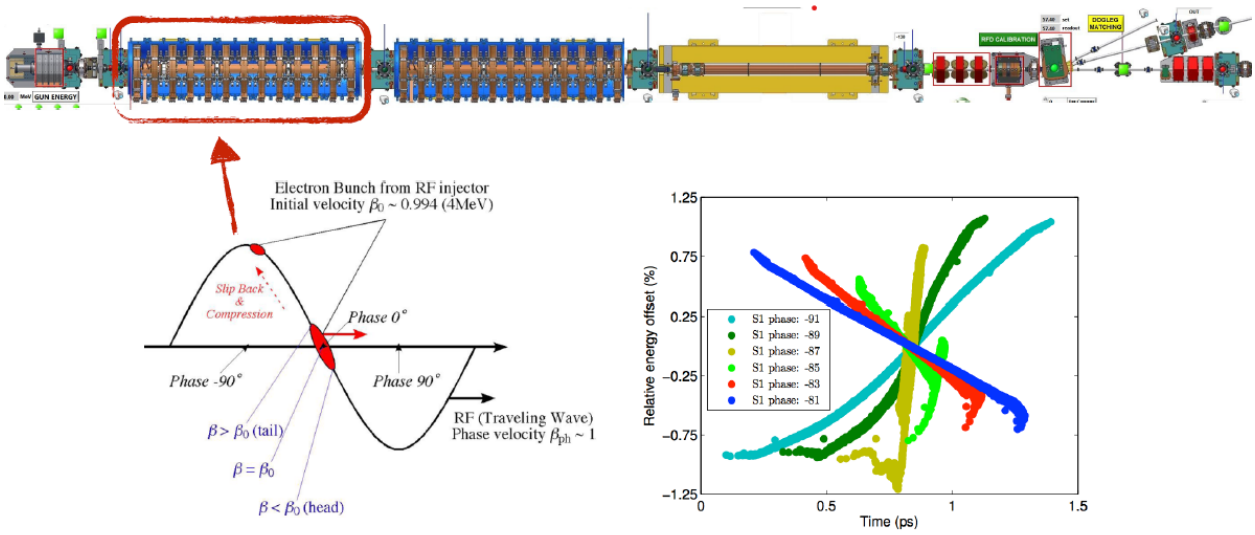

Figure 3.27: Layout of the SPARC_LAB injector, with reference to the first accelerating section operating in the velocity bunching regime.

with a focal length of about 10 cm [58] (Fig 3.28, Fig 3.29). The measurements achieved so far at SPARC_LAB for the beam-driven plasma acceleration experiment demonstrated the following limitations: Non-optimal transverse matching at the plasma entrance of the witness bunch; limited acceleration, 200 MV/m, due to the need to operate at lower plasma density and avoid transverse energy spread growth. These issues have been identified in the minimum achievable spot size at the plasma entrance which is approximately 2-3 times larger than the required one. For this reason, an upgrade has been proposed for this triplet system with the following specifications:

- 500 T/m
- bore radius 3 mm
- 16 sectors

The previous system consisted of 12-sector permanent quadrupoles and a gradient of 520 T/m.

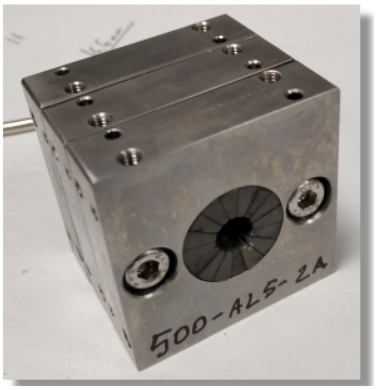

Figure 3.28: Photos of the new PMQs proposed to upgrade the previous ones.

Their field maps were extracted (Fig 3.30) and placed within the ASTRA code to characterize these quadrupoles [58]. This study aimed to evaluate the dynamics of a low-charge beam (50 pC) (Tab 3.14) by minimizing its output transverse dimension. Simulative tests were conducted to assess

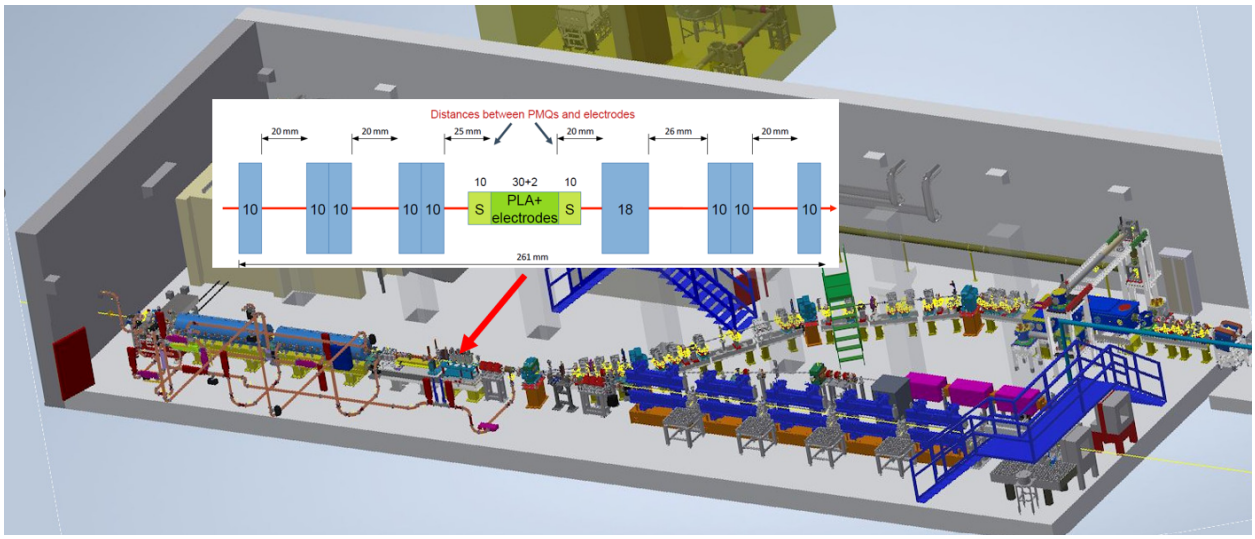

Figure 3.29: SPARC_LAB layout with an overview of the PMQ area and plasma section. An additional triplet is placed at the plasma outlet to capture the accelerated beam.

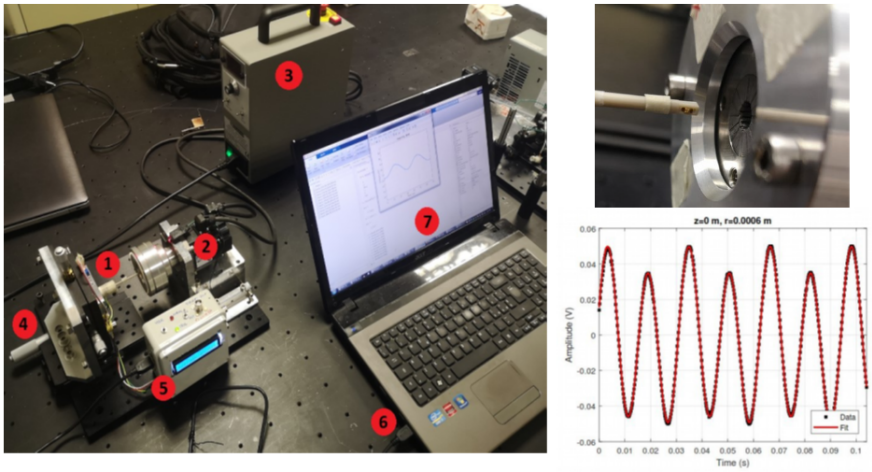

Figure 3.30: characterization of PMQs [58].

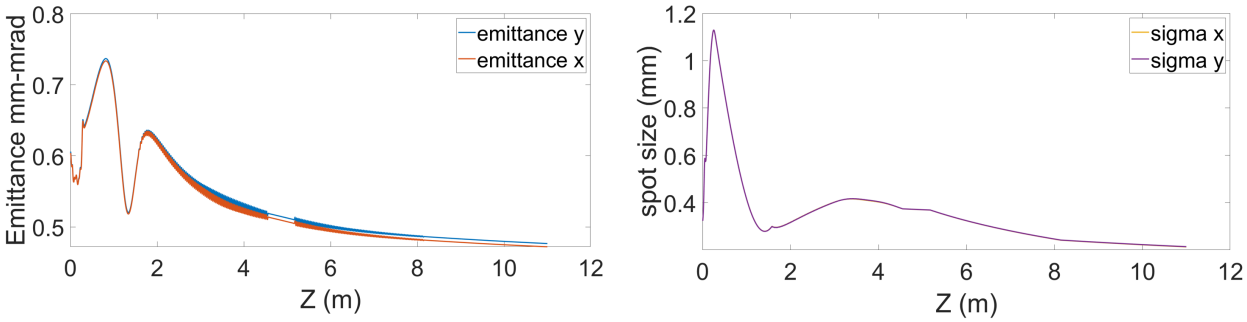

(a) emittance of 50 pC beam before PMQ

(b) Rms envelope of 50 pC beam before PMQ

Figure 3.31: evolution of emittance and rms envelope of the 50 pC beam before the PMQs.The simulation was done using ASTRA code.

whether the extracted field maps were able to reproduce the dynamics seen in the measurements. To test the PMQ maps, a 50 pC witness-like beam was optimized along the linac to reach the smallest possible spot as pointed out, in Fig 3.31a, Fig 3.31b, Fig 3.32a, Fig 3.32b there are the

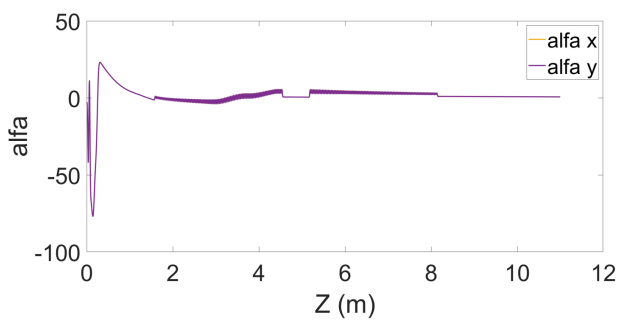

(a) alfa twiss of the 50 pC beam

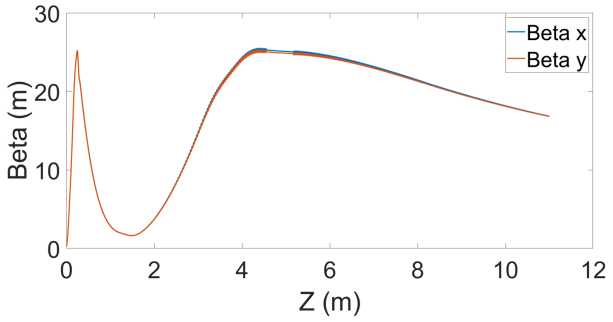

(b) beta twiss of the 50 pC beam

Figure 3.32: Twiss parameters of the 50 pC beam at PMQs entrance. The simulation was done using ASTRA code.

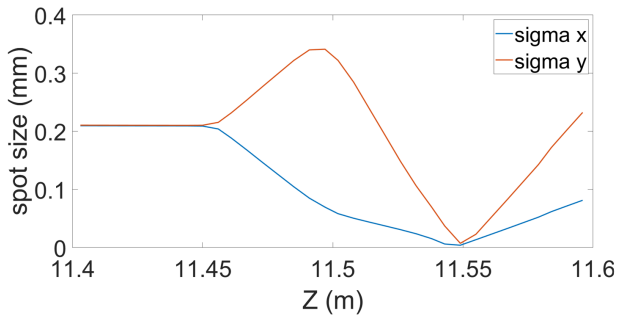

(a) Zoom of the envelope simulation of 50 pC beam with ASTRA code. We can see the minimum spot achievable before the plasma entrance.

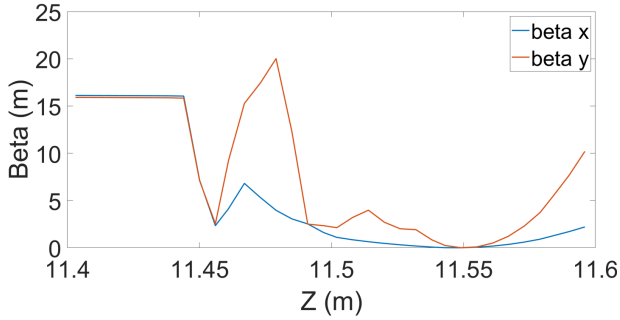

(b) Zoom of the beta function simulation of 50 pC beam with ASTRA code. We can see the minimum beta achievable before the plasma entrance.

Figure 3.33: Zoom on the spot and beta at the waist.

Table 3.14: 50 pC Beam Parameters at cathode

Beam Parameters@Cathode	Value
Spot Size	0.3 mm
Bunch Length	100 fs
Longitudinal Distribution	Gaussian
Charge	50 pC
Transverse Distribution	Radial Uniform

simulations of optimized transverse and longitudinal parameters before the PMQs entrance. The optimization involved all active elements such as accelerating sections and solenoids. The input spot to the PMQs was also optimized to minimize the focus in the two transverse planes and avoid inducing nonlinearity effects due to the proximity to the PMQ edge. Once the beam passes through the PMQs, it feels the 500 T/m field that generates a waist at 11.55 m before the plasma injection. The transverse parameters at the waist are reported in Fig 3.33, where we can observe the minimum spot size achievable of 4 um and 7 um and a beta of 5 mm and 9 mm in the x and y plane respectively. The measurements showed an order of magnitude difference from the predictions of the simulations, a spot of 40 um and 70 um. This trend could be justified by the fact that the extracted maps are too ideal and do not reproduce the actual behavior of the quadrupoles. Since the measurements showed a completely different behavior with respect to the simulations, this

PMQs layout has been substituted with a different configuration that I did not study and analyze. Another system to ensure that the beam is properly focused before entering the section at plasma is an electromagnetic quadrupole triplet system. The magnets' characteristics are:

- Max gradient : 5 T/m
- Aperture Diameter: 50 mm
- Field Quality $\frac{dB}{G_0} \cdot X$ (Go is the gradient value at the magnetic center) from n=3 to n=10 within the good field area (radius r=10 mm)$\leq 5 \times 10^{-4}$
- Air Convection cooled coils
- Current : <20 A
- Voltage : <15 V
- Room temperature: T= 23 ±1°C

Simulations for optimizing the dynamics of the SPARC_LAB linac were carried out using a comb beam with a 50 pC witness and a 200 pC driver. This working point reflects the comb beam characteristics used in the various experiments at SPARC_LAB. More details on the characteristics of the two beams at the cathode can be found in Tab 3.15. This triplet of quadrupoles is posed 10.5 cm from the beginning of the accelerating section in band C. They are 8 cm long and separate 8 cm from each other. In Fig 3.34 more details of the simulative and experimental layout are shown.

The final parameters to be met are a beam separation of 1 ps (with a density of 10^{15} cm^{-3} the

Table 3.15: Comb Working Point for Simulation with Quadrupole Triplet

Cathode's Beam Parameters	**Witness**	**Driver**
Spot Size	0.25 mm	0.32 mm
Bunch Length	100 fs	100 fs
Charge	50 pC	200 pC
Bunch Separation	3.5 ps	–

temporal distance between driver and witness should be half of plasma wavelength Fig 3.36b), and a length of 20 fs for the witness beam and 150/200 fs for the driver, respectively (Fig 3.35). Those lengths have been optimized to maintain the witness energy spread below the 1%, here alfa is the normalized accelerating gradient.

$$\frac{\delta\gamma}{\gamma} = \frac{\delta\alpha L_{acc}}{\gamma_0 + \alpha L_{acc}} \approx \frac{\delta\alpha}{\alpha} = \frac{\sigma_z}{\lambda_p} \tag{3.29}$$

More details on the equation are reported in Appendix B. The energy was set to be 75 MeV because of a limitation on the maximum gradient achievable in the C-band structure (Fig 3.36a). The Twiss parameters were optimized to achieve $\alpha \approx 0$, as this condition minimizes phase-space correlations. The beam dynamics in phase space is governed by the equation:

$$\gamma x^2 + 2\alpha x x' + \beta x'^2 = \epsilon, \tag{3.30}$$

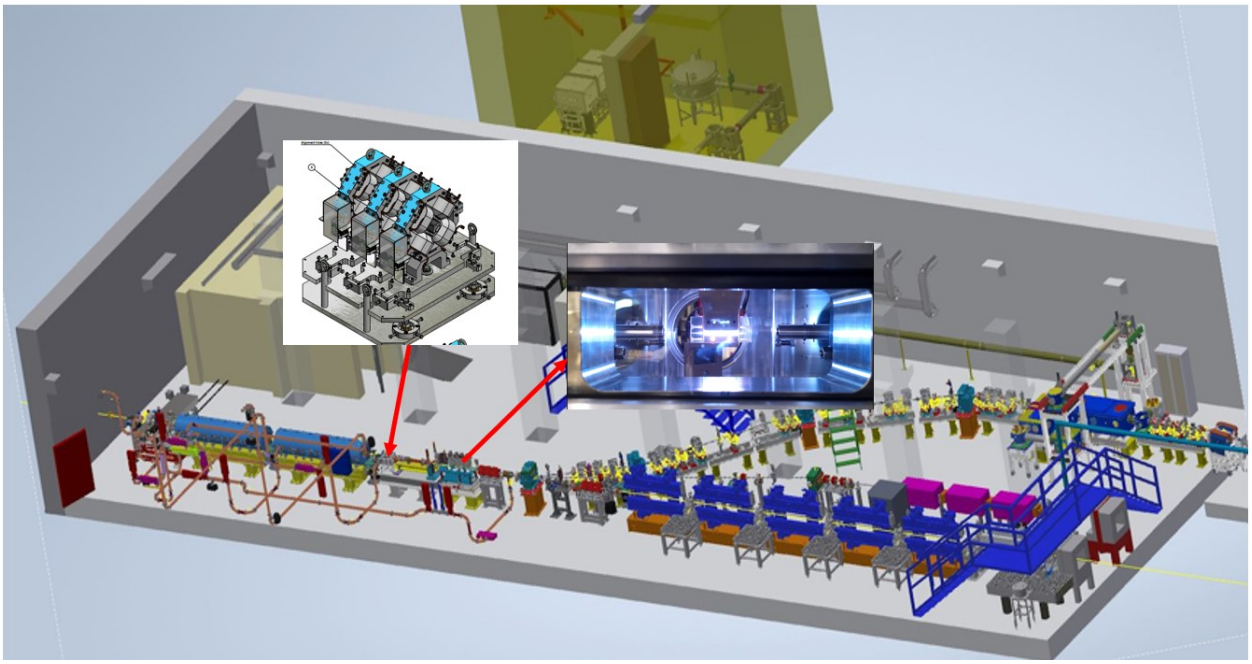

Figure 3.34: SPARC_LAB layout where we can observe the position of the quadrupole triplet and the position of the plasma section.

where $\alpha = 0$ implies that the ellipsoid in phase space is upright. This corresponds to the beam being injected at the focal waist, ensuring no initial correlations between position and divergence. As a result, the beam enters the plasma stage with minimal betatron oscillations, optimizing its initial conditions for acceleration. The design constraint for the witness beam's β-function is to keep it below 1 meter. From Eq. (3.28), the matching condition with a plasma density of $10^{15}\,\mathrm{cm}^{-3}$ gives a theoretical optimal β value of approximately 20 cm. This value was refined during the optimization process to balance practical constraints imposed by the preceding beamline optics and focusing systems (Fig. 3.37). After optimization, the Twiss parameter β for the witness beam was set to 80 cm. These simulations highlight the final focusing system's limitations before plasma injection. Specifically, the larger-than-optimal β-function reduces the ability to fully preserve the beam emittance during acceleration in the plasma, resulting in less efficient emittance preservation.

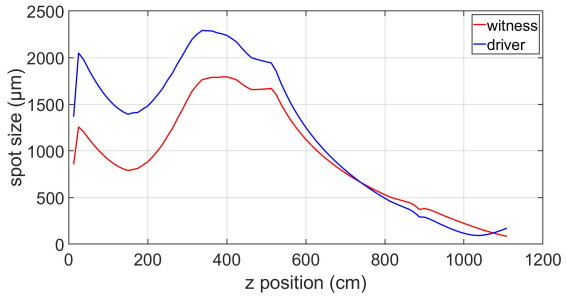

(a) envelope of the driver and witness bunches.

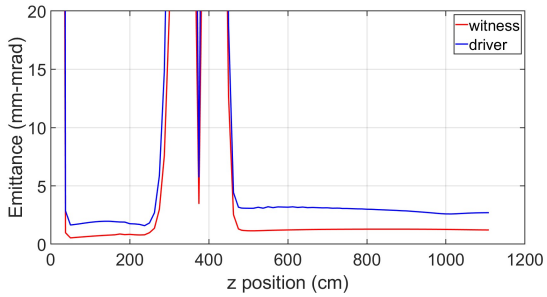

(b) emittance of the driver and witness bunches

Figure 3.35: Evolution of the envelope and the emittance of the comb beams. The final spots are 91 and 170 um respectively for witness and driver. The emittances are 1.2 and 2.7 mm-mrad.

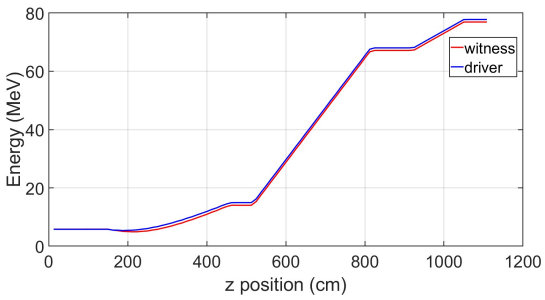

(a) Energy of the comb beam.

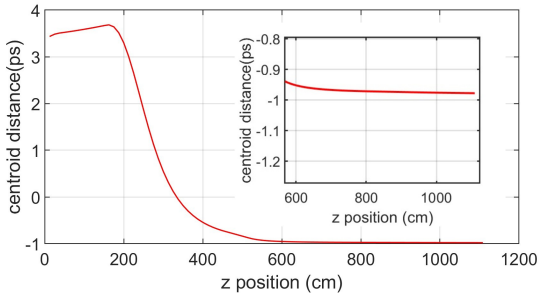

(b) Evolution of the bunch separation along the linac, final value is 1ps.

Figure 3.36: Energy and separation of the comb beam up to the end of the C-band accelerating structure. The final beam energy is 75 MeV and the bunch separation is 1 ps

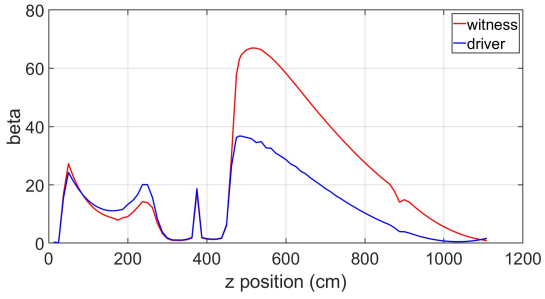

(a) Beta twiss of the comb beam.

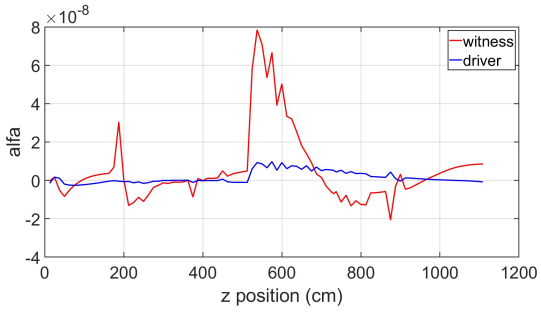

(b) Alfa twiss of the comb beam.

Figure 3.37: Evolution of the twiss parameters of the comb beam. Alfa is almost zero and, the witness beta is 0.8 m and the driver beta is 1.6 m

Chapter 4

Advanced, compact and high repetition rate C-band injector: EuPRAXIA@SPARC_LAB photo injector upgrade proposal

C-band technology possesses the capability to generate high-energy, high-brightness electron beams by significantly enhancing the peak electric fields of both the cathode and the cavity within the machine. This advanced injector design offers an innovative approach for achieving a high repetition rate, thus facilitating operations of kHz frequencies. This conceptualization is inspired by the EuPRAXIA@SPARC_LAB S-band injector, in which the original gun is substituted with a 2.6-cell C-band RF gun. This substitution leads to a proportional scaling of the injector beamline, effectively reducing longitudinal lengths by a factor of two while simultaneously doubling the electric and magnetic fields within the system. By operating with short radio frequency pulses, the 2.6-cell C-band RF gun effectively mitigates issues related to breakdown rates and power dissipation, which are common challenges in high-frequency operations. The use of higher peak fields, along with the application of established scaling laws to decrease laser spot size and duration, allows for significant reductions in both cathode and space charge emittance. This results in improved beam quality, which is crucial for advanced applications. The integration of a complete C-band injector is anticipated within the framework of the X-band linear accelerators for the EuPRAXIA@SPARC LAB design study. This integration aims to produce ultra-high-quality beams that are optimally suited for cutting-edge applications such as advanced light source production or plasma acceleration. These applications require precise control over beam properties, for the stability of a user facility, and benefit from the enhanced performance characteristics offered by C-band technology. By advancing the design and implementation of this innovative injector, this work hopes to unlock new possibilities in high-energy physics and related fields.

4.1 Design of a high gradient, high repetition rate C-band photo injector

High-brightness RF photoinjectors are crucial for generating electron beams with high peak current and low transverse emittance. C-band technology was selected as a compromise between S-band and X-band technologies. It offers a higher peak field in the gun region, which enhances beam brightness and provides a higher accelerating gradient in the TW accelerating structures compared to S-band technology. At the same time, it offers greater flexibility in terms of electron beam charge and length compared to the X-band solution. Additionally, it is expected to ensure reliable operation at repetition rates of up to 1 kHz. A C-band injector, operating at 5.712 GHz, is particularly beneficial for enhancing beam quality and brightness. Optimizing both active and passive machine components, such as laser systems, gun solenoids, and RF devices, is essential to increase brightness by an order of magnitude compared to the current state of the art. Start-to-end beam dynamics simulations will be conducted to determine the optimal configuration for the C-band photoinjector. The motivations behind the EuPRAXIA@SPARC_LAB C-band injector proposal include:

- **Higher Peak Fields**: Achieving cathode and accelerating structures peak fields as high as 160-180 MV/m and 60 MV/m, respectively (S-band is limited to 35 MV/m) [59][60].
- **Increased Efficiency**: Making it suitable for applications requiring repetition rates in the range of 200 Hz to 1 kHz.
- **Reduced Footprint**: Maintaining high-quality, high-brightness beams while minimizing the injector's physical size [61].
- **Easier transition to the X-band booster.**

The preliminary layout of the RF injector includes a C-band SW RF gun operating at 5.712 GHz (Fig 4.1), with 2.6 cells, followed by four C-band TW accelerating structures, each 2 meters long [62]. The first and second accelerating structures can utilize the velocity bunching regime, similar to the S-band configuration, with both "comb" and single bunch configurations, and are surrounded by emittance compensation solenoids. The 2.6-cell SW gun operates with a peak field (E_{cath}) of

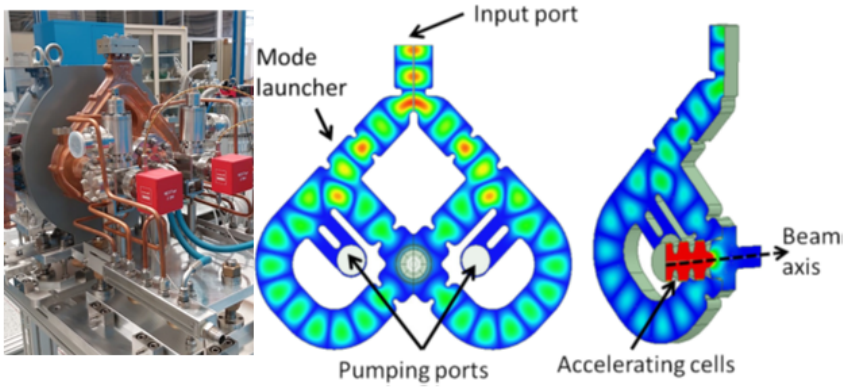

Figure 4.1: Layout of the 2.6 cells C-band RF gun [63]. The introduction of a mode launcher opens an increased flexibility in positioning the input waveguide relative to the gun body turns in a more powerful cooling capability of the accelerating cells especially useful for the high repetition rate operation.

160–180 MV/m (400-100 Hz, Fig 4.2). It is designed with a coupling coefficient of 3 to allow operation with short RF pulses (less than 300 ns), reducing breakdown rates (BDR), pulsed heating, and power dissipation [63]. The design and fabrication of the gun is driven by the main quantities that play a crucial role in the BDR control: the peak electric field, the modified Poynting vector, the RF pulse length, and the pulsed heating, with the parameters in Tab 4.1. The gun is designed and fabricated keeping these under control quantities. A beam dynamics study with a drive-live

Parameter	**Unit**	**Value**
Frequency	GHz	5.712
Number of cells		2.6
Ecath/$\sqrt{Pdiss}$	MV/(m×MW$^{0.5}$)	51.4
Peak input power	MW	18
Cathode field	MV/m	160 (180)
Cathode type		OFHC copper
Rep. rate	Hz	100 (400)
Quality factor		11900
Filling time	ns	166
Coupling coefficient		3
RF pulse length	ns	300
Mode sep. $\pi - \pi/2$	MHz	47
Esurf/Ecath		0.96
Mod. Poy. Vect.	W/mm^2	2.5
Pulsed heating	°C	<16
Av. diss. Power	W	250 (1000)

Table 4.1: 2.6 cells C-band Gun parameters.

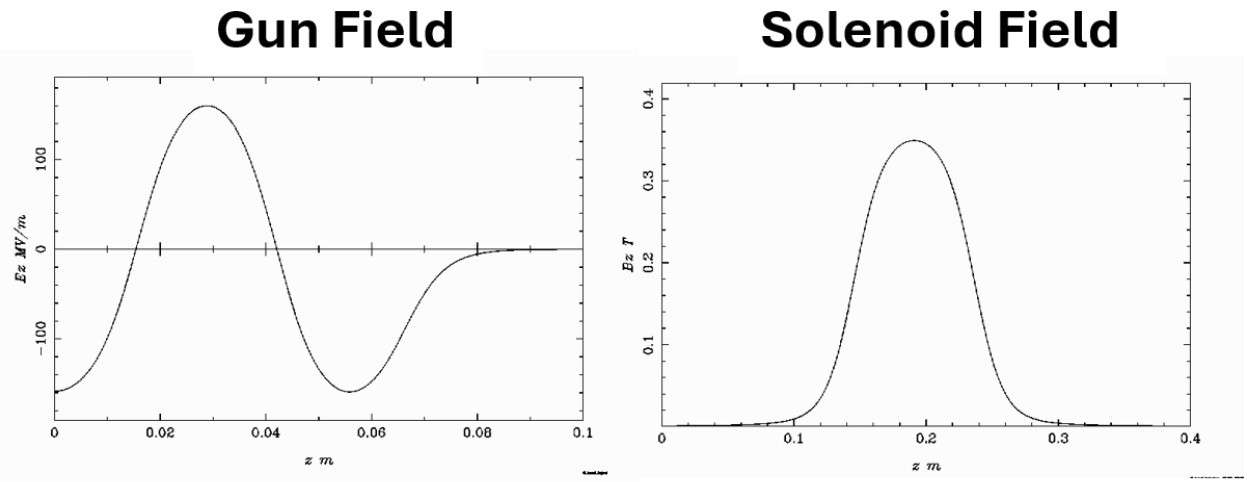

Figure 4.2: Gun electric and solenoid field.

beam has already been conducted with a similar layout. This section presents the implementation of two velocity bunching acceleration structures to achieve ultra-short, high-quality beams ready to interface with a plasma section. The initial phase in the design of the new injector involved a comprehensive study of velocity bunching dynamics, focusing specifically on single beam configurations. This phase included simulating electron beams that resemble both driver-like and witness-like

characteristics to assess the feasibility of operating a C-band photoinjector within this regime. In the context of a fully S-band configuration, conducting such a study might be considered superfluous, as the SPARC_LAB photoinjector already serves as a reference point. At SPARC_LAB, velocity bunching operations, even with single beams, are routinely performed. This familiarity and routine handling underscore the capability of the S-band configuration to effectively manage velocity bunching without necessitating further investigation. However, transitioning to a C-band photoinjector presents unique challenges and opportunities. The higher frequency and peak fields associated with C-band technology necessitate a detailed examination of how velocity bunching can be optimized for this specific configuration. By thoroughly simulating and analyzing the dynamics of driver-like and witness-like beams, the aim is to ensure that the C-band photoinjector can achieve similar or improved performance compared to its S-band counterpart. The study's goal was to explore how the enhanced electric fields and reduced longitudinal lengths of the C-band setup could impact beam compression and quality. These simulations help identify potential adjustments needed in the photoinjector design to accommodate the distinct operational characteristics of C-band technology. Ultimately, the insights gained from this study will contribute to refining the injector's design, ensuring that it can deliver high-quality, high-brightness beams suitable for PWFA applications. The photoinjector design presented here deviates partially from conventional scaling laws and encounters technological challenges, particularly related to RF components under high repetition rate operations. These challenges include the maximum achievable peak fields and operational constraints, such as the mechanical and space requirements between components for diagnostics, vacuum systems, or other functionalities. A significant effort has been made to design a new C-band gun, complete with a dedicated power distribution system and solenoid. In a C-band injector design in [64] a 1.6-cell C-band gun that operates at a peak field of at least 240 MV/m has been proposed. However, for constraints in terms of high repetition rate operations, this field is too high for my solution. In such operations, the maximum available field is limited to 160 MV/m at 1 kHz to avoid breakdown. To overcome this constraint a 2.6 cell is proposed, an additional cell with respect to the gun presented in [64]. This modification ensures that the beam enters the downstream accelerating section with a minimum energy of 5.5 MeV. Additionally, a mode launcher was introduced to improve flexibility in positioning the input waveguide relative to the gun body[65]. This design feature enhances the cooling capability of the accelerating cells, which is particularly beneficial for high repetition rate operations. The gun layout, along with the mode launcher and the on-axis electromagnetic field (Fig 4.1). However, this layout introduces two significant drawbacks [66]:

1. **Continuation of the Electromagnetic Field in the Mode Launcher Region:** This could potentially impact the beam dynamics, requiring careful management to avoid adverse effects.

2. **Complex Gun Solenoid Design:** The solenoid requires a larger bore and the introduction of a bucking coil to cancel the magnetic field at the cathode. This is crucial for minimizing the magnetic field's contribution to the beam's emittance, which is essential for maintaining beam quality.

This design represents a balance between addressing the challenges of high repetition rate operation and optimizing beam dynamics. By addressing these challenges head-on, the new design aims to

leverage the benefits of C-band technology while maintaining the reliability and efficiency demonstrated by existing S-band systems. This approach not only highlights the potential of C-band injectors but also paves the way for their broader adoption in research facilities.

4.1.1 Beam dynamics simulations and optimizations

In the literature [62][67], there is a study conducted on a C-band photoinjector (Fig 4.3), utilizing a single bunch distribution. The beam dynamics have been studied to generate a 200-pC beam with a variable length in the range of 55–280 μm. Specifically, three beam lengths have been investigated: 55 μm, 100 μm, and 280 μm. The 55 μm beam is of interest as a driver for a particle wakefield acceleration system, while the 100 μm and 280 μm beams represent the maximum lengths that avoid distortions in the longitudinal phase space when passing through a downstream X-band or C-band booster linac, respectively. The main EuPRAXIA@SPARC_LAB working point relies on an electron beam with 1 GeV energy, less than 1 mm·mrad transverse emittance, and at least 1.5 kA peak current at the undulator entrance. The beam energy will be boosted up to 1 GeV by using the X-band linac, coupled or not with the plasma acceleration module, depending on the type of application. For these purposes, the plasma accelerator requires a so-called comb-beam, consisting of a 200 pC—55 µm/75 µm long beam (the driver) followed by a 30 pC—3 µm long beam (the witness). On the other hand, the full X-band linac option (without plasma) requires a single bunch with charges in the range of 200–500 pC (high flux light sources) and an rms length of the order of 100 µm. In both cases, the photoinjector will be operated in the velocity bunching configuration with different compression regimes. This layout was initially taken as a reference and subsequently

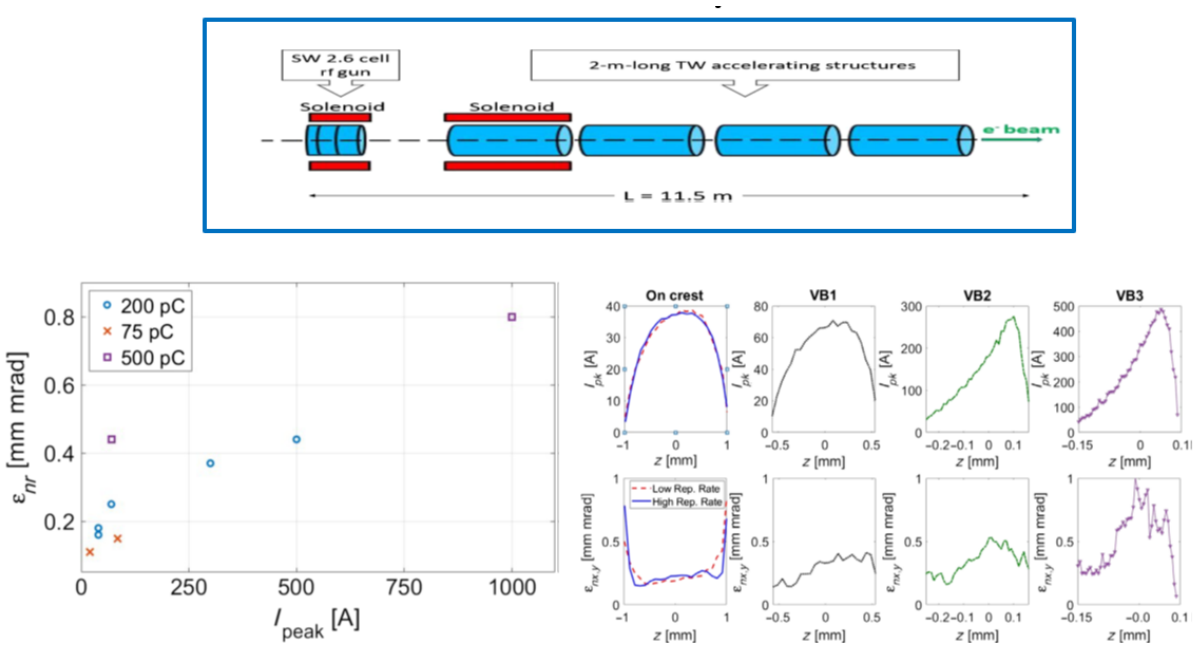

Figure 4.3: Beam dynamics simulations with a driver-like electron beam for the C-band injector. The plots show the evolution of the peak current of the beam for different velocity bunching compression phases [62]. These simulations have been taken into account for the preliminary layout implemented in the simulations

optimized for PWFA applications. The primary goal was to adapt the injector configuration to effectively serve the requirements of these advanced applications. The first step in this optimization process involved implementing a second VB structure in the XLS Compact Light injector layout (Fig

4.4). This addition complemented the existing VB section, allowing the system to achieve both single and comb beam lengths at the end of the injector. By introducing this second VB section, the study aims to enhance the flexibility and performance of the photoinjector, enabling it to produce beams with the desired properties for PWFA experiments. This enhancement was crucial for tailoring the beam characteristics to meet the stringent requirements of PWFA applications, where precise control over beam length and quality is essential for successful acceleration. As introduced in the

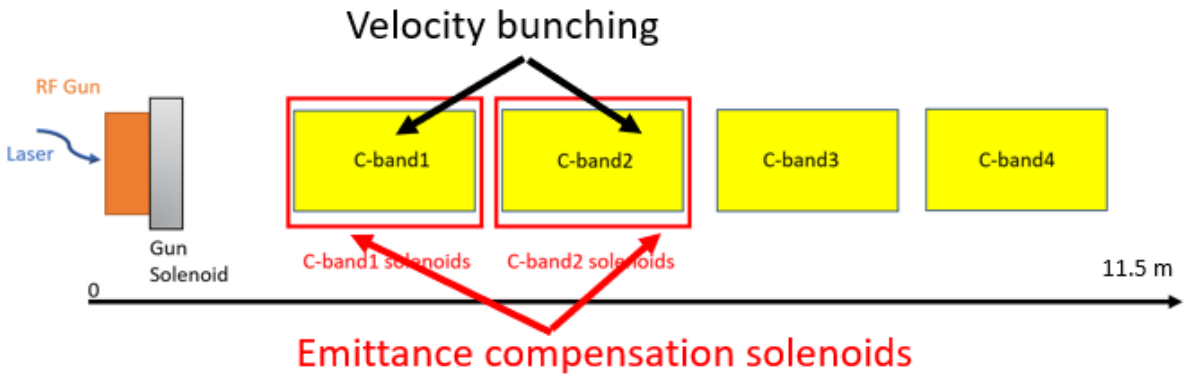

Figure 4.4: Preliminary layout of the full C-band injector with an overall length of 11.5 m. In the figure there is the detail of the second VB accelerating structure added in the layout to serve the PWFA application.

previous section, the first step was to test the feasibility of establishing a working point based on double velocity bunching with individual electron beams that mirrored the characteristics of the driver and witness beams. The comparison was made using the parameters from the S-band injector, focusing initially on the one-to-one reproducibility of the single beam. The results presented in the following figures (Fig 4.5, Fig 4.6), and summarized in Tab 4.2, demonstrate that this injector is capable of reproducing the dynamics of individual beams in terms of high brightness, ultrashort beam duration, high peak current, and low emittance. After verifying this reproducibility of

Table 4.2: Single Bunch Parameters at Injector Exit.

Injector Exit Parameters	Witness (30 pC)	Driver (200 pC)
Spot Size	0.42 mm	0.67 mm
Bunch Length	5.0 μm	62.0 μm
Emittance	0.58 μm	1.29 μm
Energy	156 MeV	157 MeV
Peak Current	1.6 kA	0.8 kA

managing to control the dynamics of a single witness-like and driver-like beam in a double velocity bunching compression stage, the next step was to implement a comb working point (both driver and witness) on the machine to assess its response. The optimization of this working point followed the same approach as in the S-band case, aiming to reproduce the beam parameters dictated by the plasma requirement and generated by the S-band photoinjector. A direct comparison was then made with the comb beams at the output. With the addition of the comb configuration, the first step is to re-optimize the bunch parameters at the cathode. The bunches are shortened from 290 fs to 220 fs, and the bunch separation is increased to 6.3 ps. The new bunch parameters are reported in Tab 4.3. The key points in the simulations are:

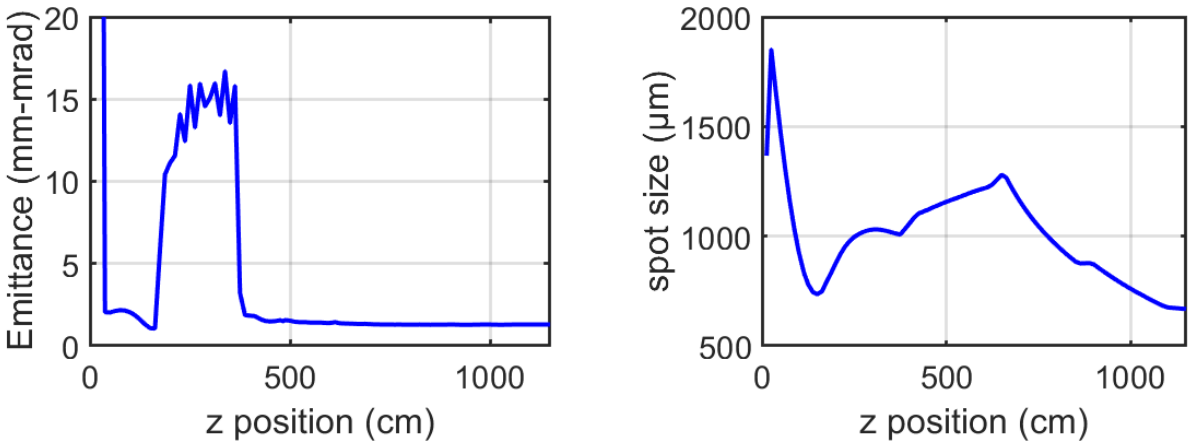

(a) evolution of driver emittance

(b) evolution of driver Rms envelope

Figure 4.5: evolution of emittance and rms envelope of the driver-like bunch.

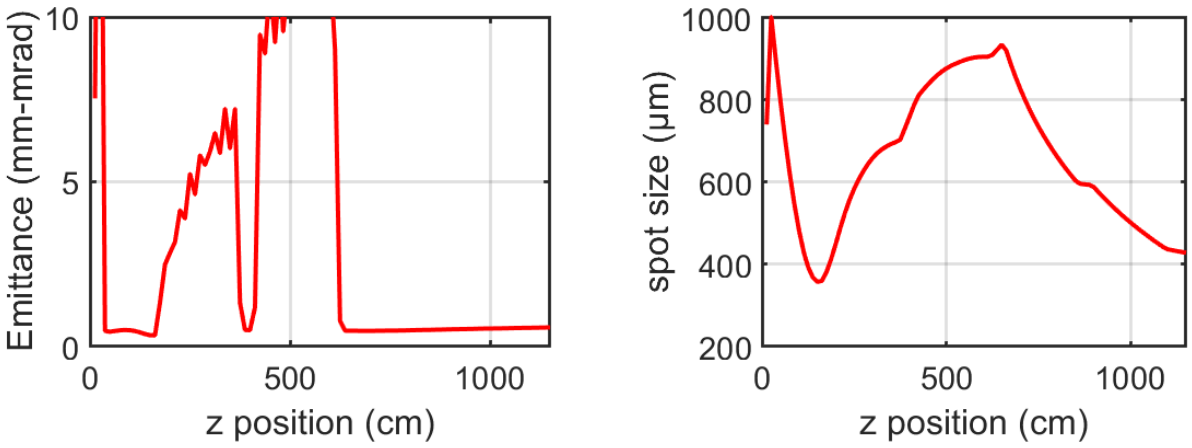

(a) evolution of witness emittance

(b) evolution of witness Rms envelope

Figure 4.6: evolution of emittance and rms envelope of the witness-like bunch.

- Setting the cathode field strength: If the energy at the gun exit is too high, the velocity bunching effect may not provide sufficient compression of the bunches at the photo-injector exit.
- Adjusting the compression phases in the velocity bunching (VB) structure to control the degree of compression.
- Controlling the bunch separation to match the beam with the plasma module.

The preliminary results of the comb simulation, shown in Tab 4.4, indicate that the longitudinal and transverse parameters of the witness bunch at the photoinjector exit meet the desired specifications: very short bunch length (Fig. 4.7a), high peak current Fig 4.8c, and low transverse emittance Fig 4.8a. While the driver dynamics are nearly reproduced, the driver bunch length is larger compared to the results from the S-band injector and the driver-like single bunch (Fig. 4.7b). Additionally, the bunch separation of 0.22 ps, as reported in Tab 4.4, is insufficient (the target is 0.5 ps) for operating with the design plasma density. Once I observe that the single bunch operation in a double compression scheme is feasible, in terms of parameters related to the high brightness operation, the

Table 4.3: Beam Parameters @ Cathode

Beam @ Cathode	Witness	Driver
Bunch Length	220 fs	220 fs
Charge	30 pC	200 pC
Spot Size	0.175 mm	0.35 mm
Bunch Separation	6.3 ps	–

Table 4.4: Driver and Witness Bunch Parameters at Injector Exit

Injector Exit Parameters	Witness	Driver
Bunch Length	3.4 μm	100 μm
Emittance	0.48 μm	1.40 μm
Energy Spread	0.2 %	1.1 %
Peak Current	1.9 kA	0.3 kA
Bunch Separation	0.22 ps	–

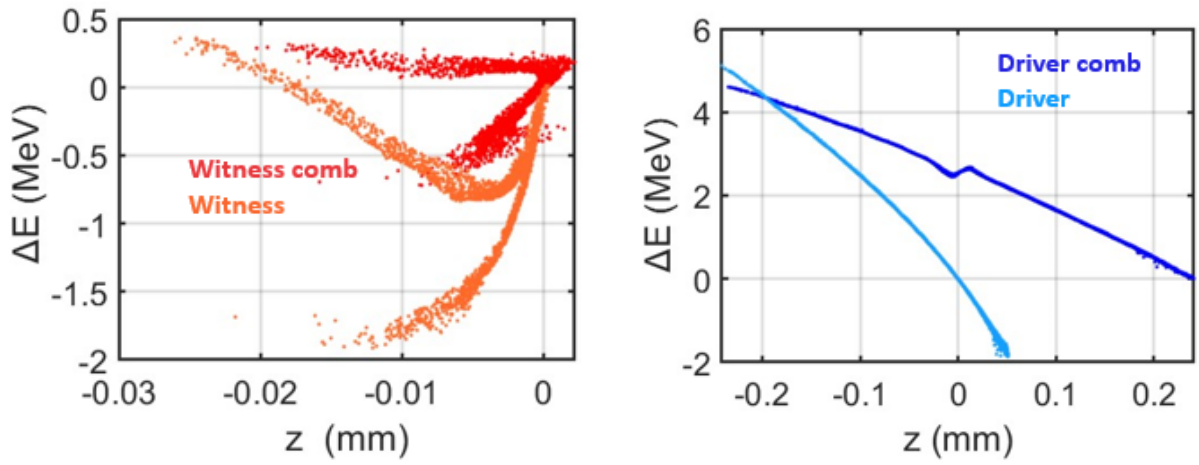

(a) witness lps **(b)** driver lps

Figure 4.7: Longitudinal phase space (lps) of driver and witness bunches, alone and in the comb configuration. The plots show the differences between the single beam lps with the correct parameters and the comb beam who still need to be optimized.

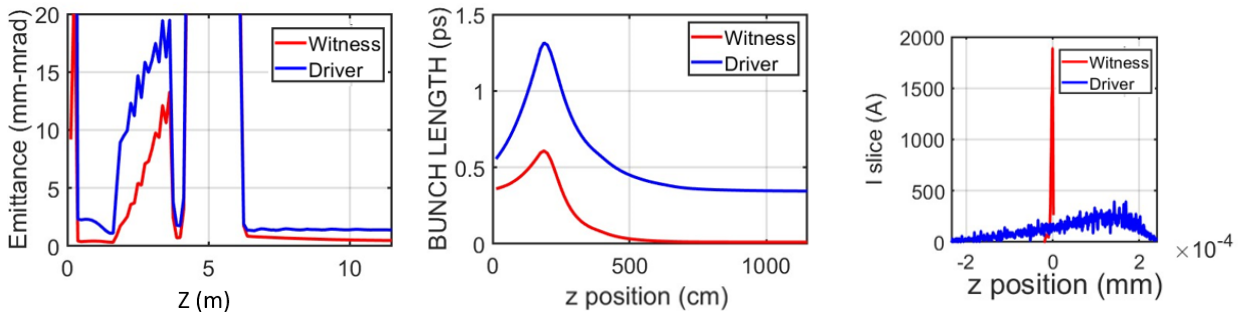

(a) Emittance **(b)** bunch length **(c)** peak current

Figure 4.8: Emittance, bunch length, and peak current of the comb beam.

C-band photoinjector has been scaled from the S-band layout (Fig 4.9), maintaining the 2.6 cell RF gun, shrinking by factor 2 the longitudinal lengths, while doubling the electric and magnetic fields [61] (Fig 4.10). Also, the drift between the cathode and the first section will be properly scaled and then re-optimized. Considering the higher peak field and properly reducing the laser spot size and the duration using the well-known scaling laws. Using the ASTRA code, I optimized the positions of the sections and the integrated magnetic fields. The RF phase of the first two sections was adjusted to achieve RF compression through velocity bunching. The C-band injector, scaled from the S-band design, features an initial cavity length of 1.5 meters, with subsequent cavities each measuring 1 meter. The electric fields within the cavities are doubled compared to the S-band configuration. The first cavity operates with a peak electric field of 34.4 MV/m to support velocity bunching operations. Additionally, the magnetic field in the solenoid cavities is also doubled in accordance with the scaling laws. The final layout of the injector is shown in the following figures. The distribution at the cathode was also optimized to achieve the desired injector output parameters. The major change was the lengths of the beams at the cathode, which were halved as expected. However, the separation between the beams was increased to 11.5 ps (Tab 4.5 and 4.11, to allow them to achieve the final separation required for injection into the plasma section. Further optimizations were made to the beam line elements to fully reproduce the

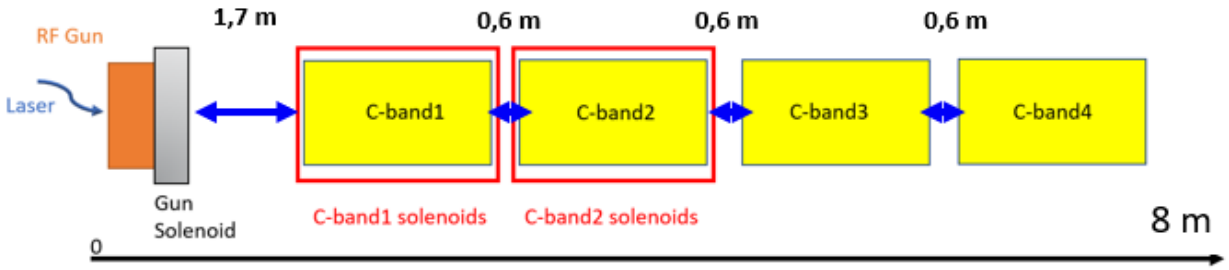

Figure 4.9: Final C-band injector layout with an overall length of 8m. The C-band injector, scaled from the S-band design, features an initial cavity length of 1.5 meters, with subsequent cavities each measuring 1 meter. The electric fields within the cavities are doubled compared to the S-band configuration.

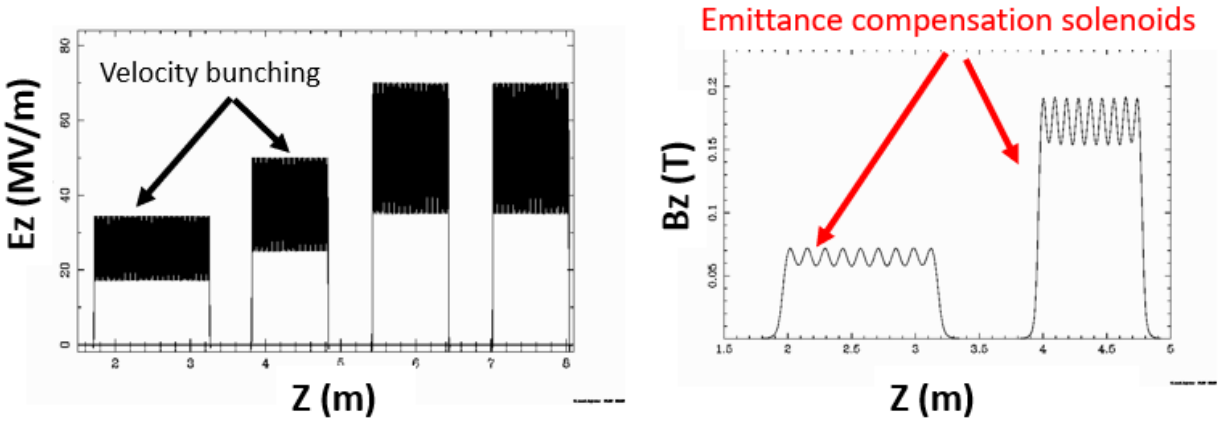

Figure 4.10: Peak Electric (left) and magnetic (right) field of the C-band injector with the details on the VB accelerating structures and the emittance compensation solenoids. The 70 MV /m accelerating field value seen in the last two structures must be multiplied by a factor of 0.7 to obtain the correct field value seen by the beam. This is because the ASTRA code wants the peak value of the field.

Table 4.5: New Beam Parameters @ Cathode

Beam @ Cathode	Witness	Driver
Bunch Length	100 fs	100 fs
Charge	30 pC	200 pC
Spot Size	0.20 mm	0.32 mm
Bunch Separation	11.5 ps	–

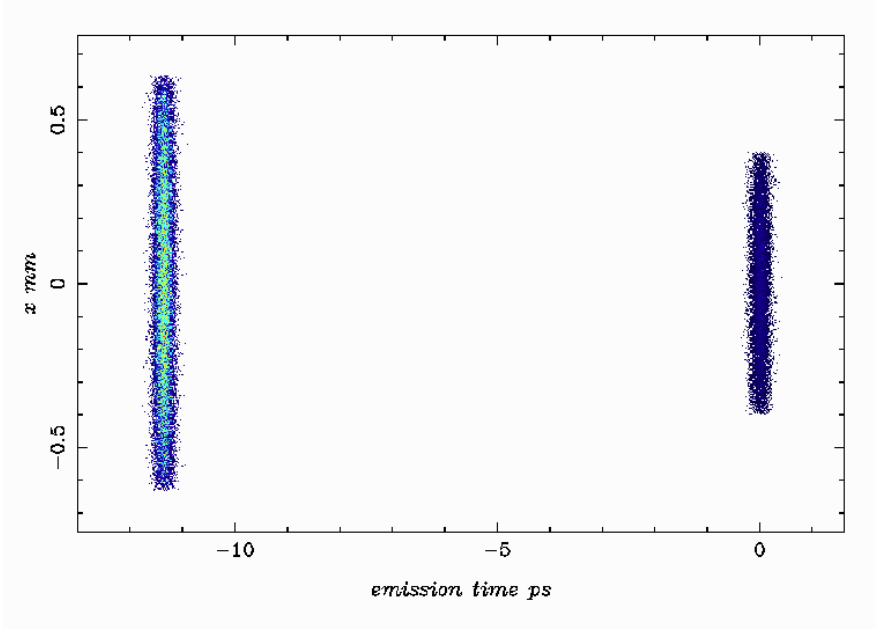

Figure 4.11: Optimized bunch separation at the cathode to reach the final separation of 0.45 ps. The first bunch at time zero is the witness, followed by the driver delayed by 11.5ps.

comb working point, Tab 4.6. The results of the simulations are presented below (Figs 4.12, 4.13, 4.14). The gradient of the first accelerating section was adjusted to accommodate VB operations, allowing beam compression to achieve a witness current peak on the order of kAs and a driver with low energy spread. The accelerating fields were doubled for the remaining cavities, and the solenoid fields around the velocity bunching sections were also doubled to compensate for emittance growth during compression. This study demonstrates the feasibility of operating a plasma

Figure 4.12: Energy and energy spread evolution in the injector.

stage equipped with a fully integrated C-band injector. By utilizing C-band technology, the system is anticipated to significantly enhance the repetition rate of the accelerator while simultaneously

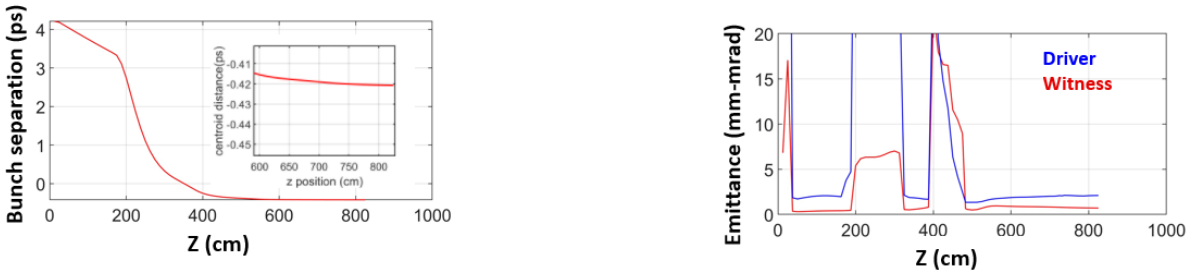

Figure 4.13: Bunch separation and emittance evolution in the injector.

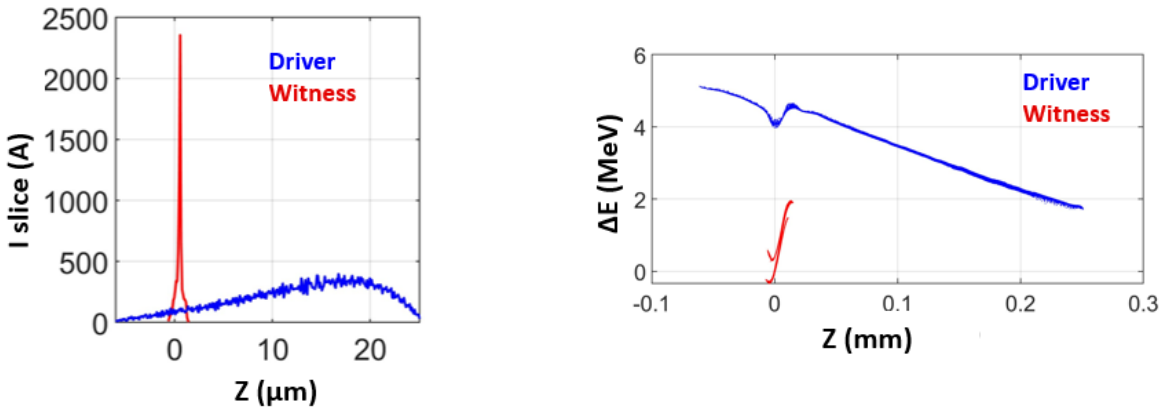

Figure 4.14: Current and longitudinal phase space at the end of injector

Table 4.6: Driver and witness bunch parameters at injector exit.

Injector Exit Parameters	Witness	Driver
Bunch Length	3.2 μm	70 μm
Emittance	0.7 mm-mrad	2 mm-mrad
Energy Spread	3.5 keV	5.8 keV
Peak Current	2.35 kA	0.35 kA
Bunch Separation	0.45 ps	–

reducing the physical footprint of the injector. The compact design not only optimizes space but also maintains high-quality beam performance. This advancement represents a significant step forward in achieving more efficient and space-conserving accelerator designs, potentially leading to improved overall performance in particle acceleration applications.

4.2 Photo injector stability and jitters analysis

As discussed in Section 3.3, jitters significantly impact beam stability and performance. To accurately compare the effectiveness of the two different injectors, it is essential to assess their operation under the influence of these machine jitters. This evaluation will provide insight into how each injector performs in real-world conditions, considering variations in phase and amplitude that could affect beam quality. Understanding their behavior in the presence of jitters will help in determining

which injector offers better stability and reliability for maintaining high-quality beams. Before delving into the specifics of the study, it is crucial to first compare how jitters impact the performance of the two types of injectors. This comparison will focus on understanding the differential effects of phase and amplitude jitters on each injector type. By analyzing these effects, we can better understand how each injector handles variations in machine conditions, providing a foundation for evaluating their overall performance and stability. This preliminary comparison will set the stage for a more detailed examination of each injector's behavior under jitter conditions. Beam dynamics as discussed in the previous chapter, have established an upper limit on the allowable RF station jitter: 0.02 degrees RMS for the S-band and 0.08 degrees RMS for the HHC. A measurement campaign was carried out @SPARC_LAB using an intra-pulse feedback prototype, with the results showing a remarkable reduction in C-band klystron phase jitter by a factor of more than 3, from 0.065 degrees to 0.019 degrees (equivalent to 9.2 fs, Fig 4.15) [68][69]. For the C-band injector jitter analysis, this phase jitter has been taken into account. It should be noted that, with the C-band

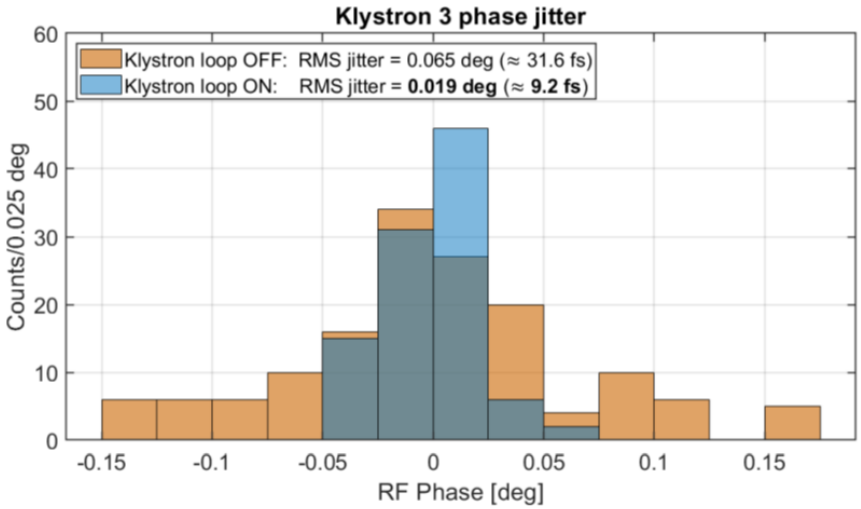

Figure 4.15: Intra-pulse feedback prototype measurement results at SPARC_LAB facility on the C-band power plant. In bold the results obtained with the new feedback on [69].

machine layout, a gentle RF compression factor, which means a compression phase nearest to the on-crest ones, is sufficient to achieve kA-level peak currents without resorting to a blowout regime or strong overcompression schemes. These approaches, which would be necessary if using S-band technology, would lead to a deterioration of beam emittance and a reduction in the stability of the working point. The jitters simulated are presented in Tab 4.7. What immediately stands out

Table 4.7: Jitter values used in the simulations are based on actual measurements taken@SPARC_LAB.

total charge	spot size	RF phase	voltage
2 %	1%	0.02 deg (10 fs)	0.02% rms

is a shorter witness that can be achieved with soft compression phases in the velocity bunching structures. The jitter of this parameter is halved, demonstrating a reduced sensitivity of the bunch length to machine jitters. In the chapter dedicated to the study of S-band injector jitters, an analytical treatment was presented explaining why the jitter of the separation between the two beams should be on the order of femtoseconds. As shown in Tab 4.8, the C-band exhibits a jitter value for

Table 4.8: Comparison between S-band (without HHC) and C-band injector jitter values in terms of witness bunch length, witness emittance, and bunch separation.

injector	witness emittance	bunch separation	witness bunch length
C-band	0,6272 ± 0,0236 (mm-mrad)	0,45 ± 0,0047 (ps)	0,0096 ± 1,6e-4
S-band	0,5732 ± 0,0027 (mm-mrad)	0,50 ± 0,0045 (ps)	0,0185 ± 3,0e-4

the distance between the driver and witness beams of 4.7 fs, similar to the S-band one. While the study on beam dynamics appears exhaustive in terms of achieving the final parameters of the comb beam, the dynamics could be further optimized, not only to establish a working point based on the reproducibility of the comb beam for PWFA applications but also to further reduce the associated jitters. Given the high peak current—2.3 kA compared with 1.8 kA in the S-band case—one could consider reducing the compression even more to further mitigate the effects of RF jitter. Of course, this statement must be proved with further simulations.

4.2.1 High Harmonic Ka-band cavity

To complete the comparison between the two injectors, the insertion of a high-harmonic cavity between the gun and the first accelerating section was also evaluated, Fig 4.16. A high-harmonic cavity is designed to generate an additional RF field component at harmonics of the fundamental frequency, which helps in manipulating the longitudinal phase space of the beam. This process reduces non-linear distortions and improves the current profile. In the S-band case, it was observed that this cavity improved the driver-witness separation. By optimizing the phase space and the current distribution, the cavity contributed to a more uniform beam quality and reduced diver witness separation jitter. This enhancement leads to better synchronization and stability of the beam, which is crucial for maintaining the performance of the accelerator and achieving the desired beam parameters. In this context, a high-harmonic cavity operating in the SW Ka-band was considered. Because the side effect of velocity bunching is to accumulate charge at the bunch head, a correction was implemented by introducing a Ka-band cavity before the first C-band structure [70]. This Ka-band cavity operates at 180° relative to the crest and decelerates the beam by approximately 0.3 MeV, the advantages of this deceleration have been described in the section dedicated to the X-band cavity. This cavity has a resonant frequency of 36 GHz and an electric field acceleration (E_{acc}) of 10 MV/m. The system comprises 19 cells, with a total length of 8 cm and a radius of 3.5 mm, Tab 4.9. The specific design and operational parameters of this cavity ensure effective beam linearization and improved performances. From analytical calculations, the

HHC	**Resonant Frequency**	**E acc**	**Number of cells**	**Length**	**Radius**
SW Ka-band	36 GHz	10 MV/m	19	8 cm	3.5 mm

Table 4.9: SW Ka-band Parameters

integrated voltage required to manipulate the LPS at the photo-injector exit is approximately 2.5 to 3.0 MV. This corresponds to a maximum applied electric field E_{max} ranging from 10 to 15 MV/m on average [47]. However, using higher voltages could result in dumping the beam or disrupting its

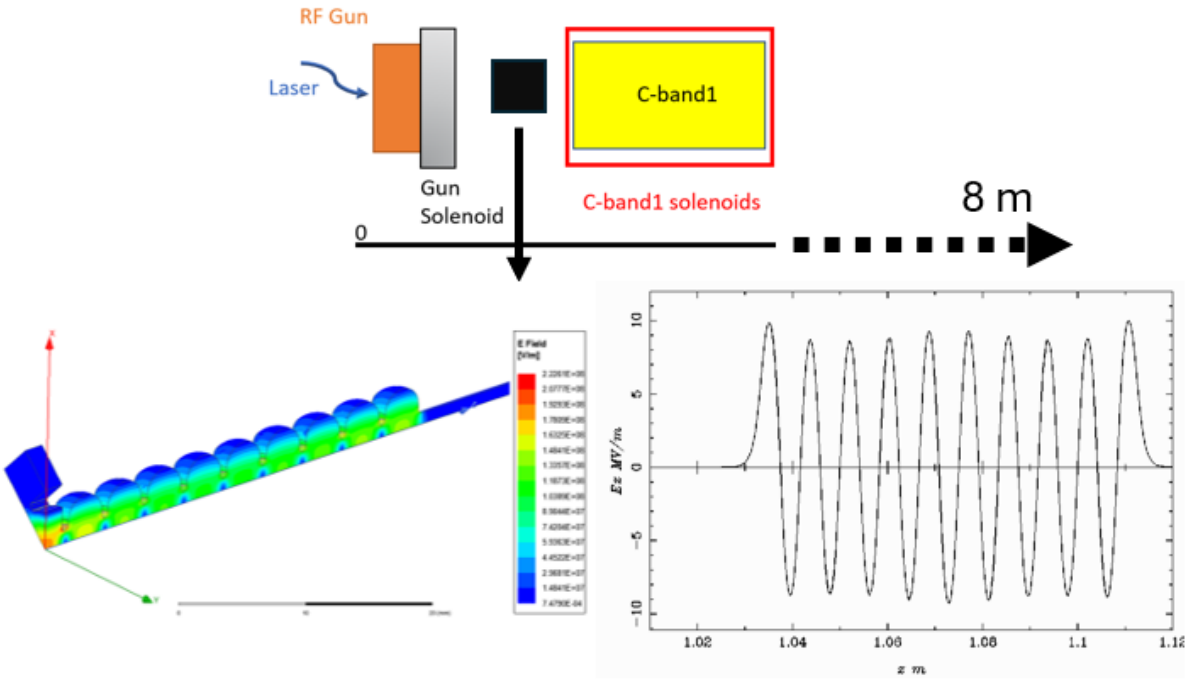

Figure 4.16: Ka-band cavity layout. 3D model of one-eighth of half a SW structure simulated with the HFSS software [70][71].

phase space quality. The equation for space phase linearization is given by [71][72]:

$$V_{\mathrm{HHC}} = \frac{k_{\mathrm{HHC}}}{k} V \cos(\phi) \tag{4.1}$$

where:

- V_{HHC} is the amplitude of the high-harmonic cavity (HHC) voltage,
- V is the amplitude of the accelerating voltage,
- k_{HHC} and k are the RF wave numbers for the HHC and the fundamental mode, respectively,
- $\cos(\phi)$ represents the phase of the accelerating voltage.

As shown in the summary Tab 4.10 of the injector output parameters, the addition of the longitudinal phase space manipulation cavity enhances the quality of the output beam in terms of brightness. The separation between the beams becomes sharper, achieving the required 0.5 ps to inject the beams into the plasma section (Fig 4.18 left). Additionally, the emittance improves by approximately 30%, decreasing from 0.7 mm-mrad (Tab 4.6), the case without the ka-band, to 0.48 mm-mrad (Tab 4.10). In Fig 4.18(right), a comparison of witness currents with and without the HHC is shown. It is noted that the peak value of the current remains unchanged despite the addition of the linearizer. There is a trade-off between emittance and peak current. Generally, increasing the peak current requires compressing the beam, which can increase emittance if not managed properly. This is because higher compression can increase the angular and spatial spread of the particles. Coupling soft velocity bunching with a high-harmonic cavity enables the successful reduction of emittance while maintaining a high peak current value. This approach allows for optimizing the

beam quality by improving the spatial and angular distribution of particles, thus achieving a high brightness without compromising on the current. The benefit of the HHC in the dynamics of the comb beam is much more clear in this layout since the degree of the deceleration is smaller 0.3 MeV compared to 1.27 MeV with the X-band and the related LPS distortion is lower. This type of system, which employs a 36 GHz cavity, is highly futuristic and entails a significant effort in terms of research and development, making it very challenging. However, during the optimization of this alternative injector, the use of different high-harmonic cavities was also considered, including the X-band, either as a single cavity as in the previous case or as two consecutive cavities to make the layout more feasible in a real-world scenario. Simulations conducted with the previously highlighted solutions, however, did not yield acceptable results in terms of the injector's output parameters, making the Ka-band the only viable option for adequately manipulating the longitudinal phase space of the bunches and making them suitable for PWFA applications. Nonetheless, this solution is far from straightforward or easy to implement.

Beam parameter	Witness	Driver
Emittance (mm-mrad)	0.48	2.46
Energy (MeV)	136	138
Energy spread (KeV)	4.6	4.8
Bunch separation (ps)	0.5	–
Bunch length (um)	3.7	56

Table 4.10: Injector exit parameters

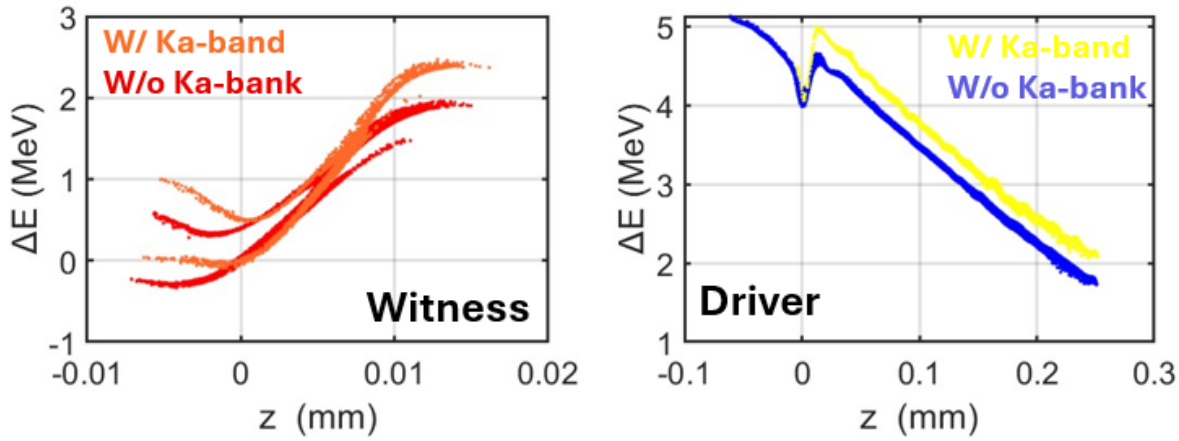

Figure 4.17: Final LPS of the driver and witness bunches

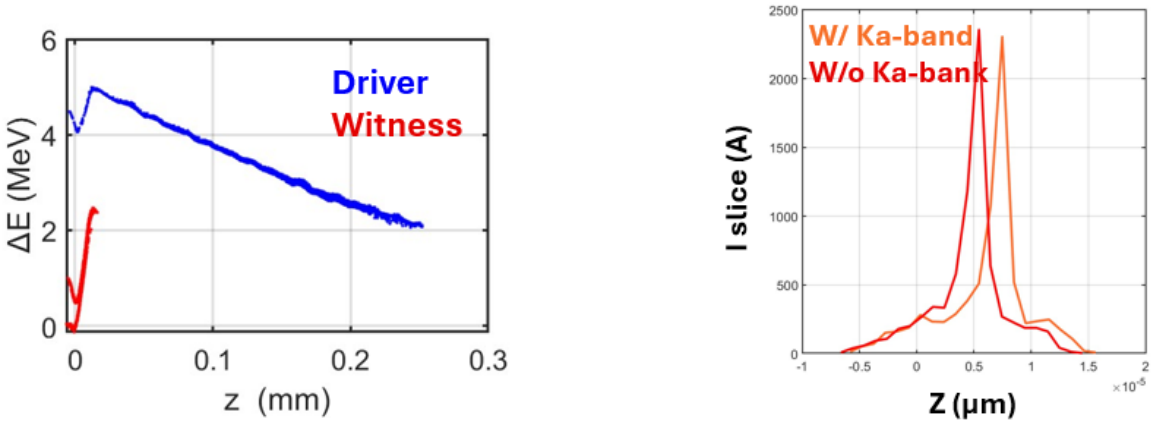

Figure 4.18: LPS (right) of the comb beam where now is much more clear the separation between the bunches.Peak current (left) of the witness beam w and w/o the Ka-band linearizer

Chapter 5

High brightness beam @PEGASUS beamline

PEGASUS (Photo Electron Generated Amplified Spontaneous Undulator Radiation Source) is a compact accelerator laboratory constructed to study high-brightness electron beams and test novel concepts in accelerator and beam physics (Fig 5.1, 5.2). In the last year, PEGASUS has become an important laboratory for the study of the physics and applications of beams with very low charges, characterized by sub-100 fs bunch lengths and nm-scale emittances. One of the main characteristics of the laboratory is that it is entirely student-run, thus offering unmatched hands-on experience to all students and trainees working in accelerator and beam science at UCLA. Among the conceivable topics, two standout areas beckon for exploration: Firstly, an empirical inquiry into the feasibility of employing alternative metal cathodes, specifically focusing on yttrium (Y), as a substitute for conventional copper (Cu), this study is to complete the study regarding photoinjectors by including the electron source part as well. This investigation aims to elucidate the viability, efficiency, and potential advantages of such a transition. Due to a lower work function with respect to Cu, Y photocathodes are particularly appealing for the possibility of illuminating them with visible laser pulses. This has the advantage of a higher energy per pulse, paving the way to high repetition rate photoinjectors, driven by conventional laser sources. In addition, working at $\lambda \sim 400$ nm, the small energy difference between the Y work function and the laser photon energy reduces the contribution of the intrinsic emittance of the material [73]. The possibility of driving the photoemission with radiation in the visible range avoids the conversion to higher laser harmonics. This solution increases the laser energy per pulse, allowing for electron bunches with more available charge. Secondly, a study on Markov Chain Monte Carlo (MCMC). MCMC methods [74][75][76] are a class of algorithms used to sample from complex probability distributions. These methods are particularly useful in high-dimensional spaces where direct sampling is challenging. MCMC combines the concepts of Markov chains and Monte Carlo methods to estimate distributions effectively. MCMC methods have several applications in the field of particle accelerator physics:

- **Beam Tuning**: MCMC methods optimize parameters such as magnetic field strengths, cavity frequencies, and beam optics settings to achieve desired beam properties like energy, emittance, and brightness.
- **Uncertainty Quantification**: MCMC can propagate uncertainties through beam dynamics

simulations, estimating resulting uncertainty in beam properties.

In summary, MCMC methods provide a powerful framework for sampling complex distributions, optimizing parameters, and analyzing data in particle accelerator physics. Their flexibility and robustness make them a valuable tool for tackling a wide range of problems in the field.

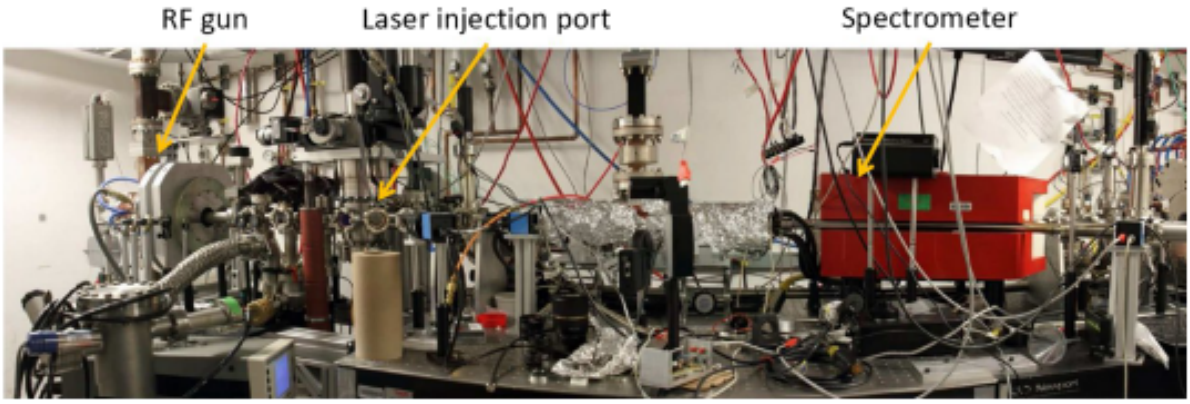

Figure 5.1: Pegasus beamline with details of the RF gun, laser port, and spectrometer [77].

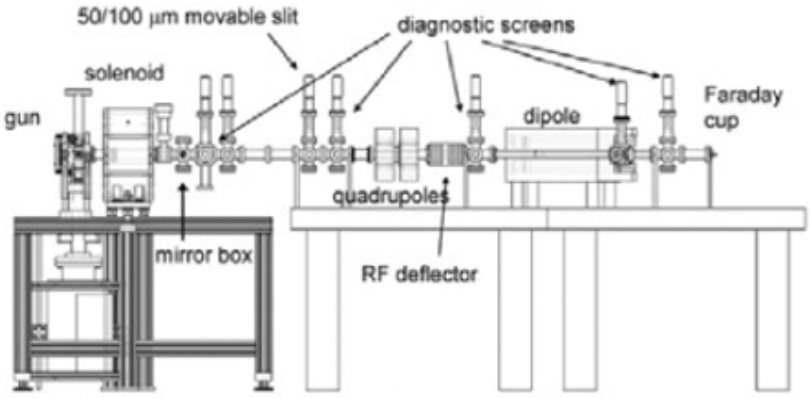

Figure 5.2: Pegasus schematic layout.

5.1 PEGASUS photogun

The Pegasus photo gun (Fig. 5.3) is a 1.6-cell cavity operating in the S-band at 2.856 GHz that can achieve accelerating gradients of up to 75 MV/m at the cathode, it has been built at INFN-LNF [77]. An ultra-high vacuum (UHV) of around 4e-10 Torr is kept in the gun when not operational. When in use vacuum rises to around 3e-9 Torr. Cathodes grown on INFN-style plugs can be inserted into the gun via a backplane which has been specially modified to allow using removable cathodes. The load lock chamber behind the gun has two transfer arms to slide the carriage out of the suitcase to exchange cathodes. The UHV suitcase allows for the cathodes to be transported from the growth chamber in Cornell to the UCLA laboratory while maintaining <1e-10 Torr. The carriage inside the suitcase can hold 4 INFN-style plugs, but only 3 slots are accessible at UCLA due to the dimensions of the transfer arms. For cathode tests, two plugs were used (an empty spot was needed to store the

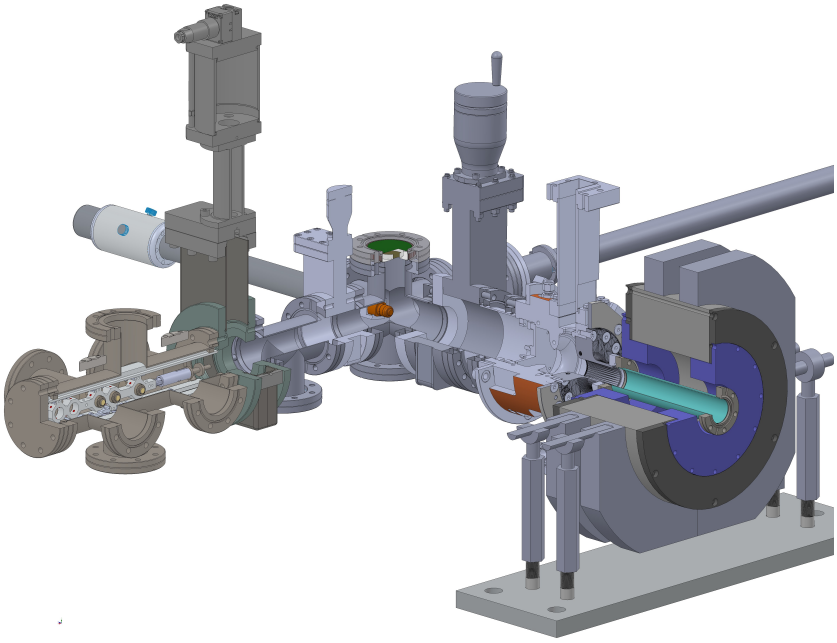

Figure 5.3: Pegasus photo gun consisting of the RF gun and solenoid for beam production and transport as well as the UHV suitcase (chamber on the left) and load-lock chamber for cathode exchange.

plug already installed in the gun). A collection coil in front of one of the cathodes can be positively biased to collect charge for low-field QE measurements.

5.1.1 MCMC approach for solenoid scan analysis

The solenoid scan method (Fig 5.4) is a technique used to measure the emittance of an electron beam. Emittance is a critical parameter that characterizes the beam's quality, describing its spread in position and angle. This method involves using a solenoid magnet to focus the beam and analyzing how the beam size changes with varying magnetic fields to determine the emittance. By

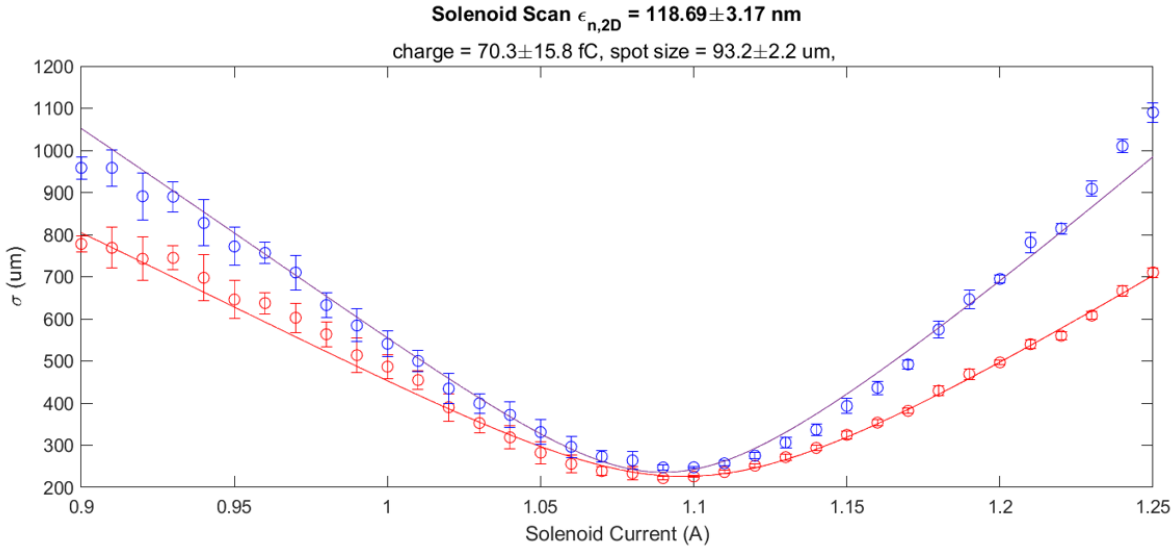

Figure 5.4: Example of a real solenoid scan. The x-axis is the solenoid current in the y-axis is spot size

varying the solenoid field and analyzing the resulting beam sizes, one can extract the beam emittance, which is essential for optimizing beam dynamics in accelerator systems. Proper calibration and consideration of potential errors are crucial for accurate measurement, so virtual diagnostics could be useful to enhance the analysis [78]. Thermal emittance is a crucial factor influencing the maximum achievable electron brightness, which varies depending on the electron source. Thermal, or intrinsic emittance, describes the transverse momentum of electrons emitted from the material surface. This emittance depends on several factors: the properties of the cathode material (including surface roughness and crystallinity), the applied electric field, and the wavelength of the incident laser. It effectively encapsulates the physics of the emission process and the properties of the cathode material, summarizing the divergence of the emitted electrons. The thermal emittance is also influenced by the Mean Transverse Energy (MTE) of the electrons. MTE reflects the properties of the cathode material, the condition of the cathode surface, and the energy of the incident photons, rather than the spot size of the drive laser. Therefore, MTE is an important parameter for characterizing cathode properties. Factors such as the electric field at the surface, crystal defects within the semiconductor cathode, and the operating temperature also affect the MTE. Equation (5.1) illustrates a commonly used formula for describing thermal emittance. Various formulas may incorporate additional emission parameters, such as the bandgap (E_{gap}), electron affinity, or photon energy. In the equation, $\sigma_{\text{laser,rms}}$ represents the root mean square (rms) spot size of the laser, c is the speed of light in vacuum, kT denotes the effective transverse energy of the electrons, m is the electron mass, $\sigma_{laser,rms}$ is the rms size of the electron bunch starting from the cathode, and MTE refers to the mean transverse energy of the electron beam. For photocathodes, a low thermal emittance is desirable, with typical values ranging from 0.5 to 1.5 um, depending on the cathode material [11].

$$\epsilon_{n,x} = \sigma_{laser,rms}\sqrt{\frac{\mathrm{kT}}{mc^2}} = \sigma_x\sqrt{\frac{\mathrm{MTE}}{mc^2}}, \tag{5.1}$$

To determine this relationship, we utilized the solenoid scan technique. By performing a waist scan with the solenoid, at different spot sizes at the cathode, we measured the MTE by applying the linear beam transport formalism to compute the emittance from the measurements (Fig 5.5). Precise measurement requires accurate knowledge of the beam energy, the relative positions of the solenoid and the screen, and the magnetic field profile within the solenoid. These parameters are essential for the fitting model, but they are often imprecisely known or may fluctuate during measurements due to intrinsic system variations, such as changes in high-power RF amplitude, phase, or gun voltage. In such cases, utilizing a virtual diagnostic can be advantageous. In this part of the work, I employ a surrogate model machine learning-based approach to enhance the analysis of solenoid scan measurements using a sample-inefficient method [79]. By combining a GPT [80] simulation model of the photoinjector with Monte Carlo Markov Chain (MCMC) analysis, we can extract accelerator parameters that are not directly measurable. This approach fundamentally improves our understanding of the photoinjector beamline. This analysis was conducted using solenoid scan measurements from the Pegasus gun. Initially, a surrogate model of the Pegasus injector was developed by running tens of thousands of simulations. This model was then used to train a multilayer neural network capable of predicting solenoid scans based on various input parameters. Finally, a combined neural network and MCMC model were employed to analyze the solenoid scans and investigate the relationships between the input parameters of the model. The photoinjector is a

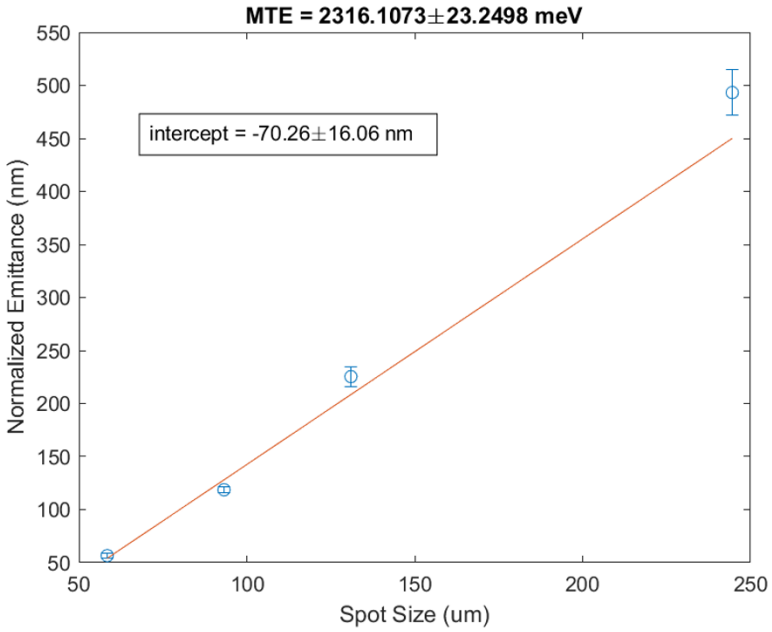

Figure 5.5: Example a typical measurement to retrieve MTE. This is an example for a copper cathode, each point is a solenoid scan result. The linear fit is done with the relation between normalized transverse emittance and the MTE.

critical component in many particle acceleration systems, and optimizing its performance requires a thorough understanding of its behavior under various operational conditions. However, detailed simulations of such systems can be computationally intensive. To address this challenge, a surrogate model has been developed using a MATLAB script to call GPT simulation code. This surrogate model enables rapid prediction of the photoinjector's performance without the need for running detailed simulations every time. Specifically, the script focuses on simulating solenoid scans and analyzing the results to create a model that can be used to optimize the system more efficiently. The range of values for the solenoid current and other operational parameters of the photoinjector are set. These parameters include:

- **MTE (Mean Transverse Energy, ev)**
- **Laser x and y rms, spot size (um)**
- **Aspect Ratio**
- **Pulse Length rms (fs)**
- **Gun Loop Voltage (mV), related to the accelerating field**
- **Gun Phase (degrees)**
- **Charge (pC)**

These parameters are varied within a specific range to explore different configurations of the system. Values are generated randomly to simulate various operational conditions. The simulations generate solenoid scan data, which is subsequently processed. After loading the simulation data, the script analyzes the results to compute key statistics and variables of interest. The analyses include:

- **Covariance Calculation**: The covariance matrix of the beam data is computed to determine the beam size and correlation.
- **Beam Dimensions**: The beam size in the horizontal and vertical directions, as well as the correlation between these dimensions, are calculated.
- **Emittance**: The beam emittance is calculated using the covariance matrix, mean energy value and beta parameter. Emittance is an indicator of beam quality and is computed for both beam directions.

The surrogate model created with this MATLAB script provides an efficient method for simulating and analyzing solenoid scans in the photoinjector. By utilizing rapid simulations and thorough analysis of the results, a predictive model can be obtained that facilitates system optimization and analysis. This approach significantly reduces the time and computational resources required compared to detailed simulations and allows for the effective exploration of multiple system configurations. This section explains the process of creating and evaluating a neural network (NN) model used for simulating the behavior of the Pegasus photoinjector. A well-documented way to speed up simulations is to use a so-called surrogate model [81], where a fast-executing ML model learns the nonlinear relationships between inputs and outputs in a system. The neural network serves as a surrogate model to predict the performance based on various input parameters. The network is designed to learn the relationship between an input dataset, referred to as `pred`, and a target dataset, referred to as `target`. Both datasets are transposed to match the format required by the neural network. For training, the Bayesian Regularization Levenberg-Marquardt backpropagation algorithm, specified by the function `trainbr`, is selected. This choice is motivated by the fact that the Levenberg-Marquardt algorithm is known for its fast convergence properties, while Bayesian regularization helps in preventing overfitting. This makes it particularly suitable for complex problems where generalization is crucial. The neural network architecture consists of five hidden layers, each containing 20 neurons. This deep configuration allows the model to capture complex nonlinear relationships within the data. The network is initialized using the `fitnet` function, which is specifically designed for regression and function approximation tasks. The dataset is divided into three subsets:

- 80% for training,
- 10% for validation,
- 10% for testing.

This division helps the model to generalize well by avoiding overfitting and ensuring that the performance is evaluated on unseen data. The training process is configured to run for a maximum of 3000 epochs, allowing the network to iteratively adjust its weights and biases to minimize the error between predicted and actual target values. Once the network is trained, it is used to generate predictions based on the input data. The difference between the predicted and actual target values is computed to assess the performance of the model. The performance is evaluated using MATLAB's built-in `perform` function, which quantifies the error in the predictions. Overall, this neural network configuration is aimed at achieving high accuracy in function approximation tasks by leveraging deep learning techniques, regularization methods, and extensive training iterations. The first

step in the process involves preparing and normalizing the simulation data (pred and target). This step is crucial for ensuring that the data fed into the neural network is scaled appropriately, which helps in improving the training efficiency and performance of the model. Data normalization involves calculating average values, standard deviations, and covariance matrices from the simulation results. These statistics are used to standardize the data, making it easier for the neural network to learn patterns and relationships. Once the data is prepared and normalized, the next step is to train the neural network. The training process involves defining the network architecture and feeding it the normalized data. The neural network learns to map the input parameters to the output parameters through iterative optimization. The network is structured with multiple layers, and the training process adjusts the weights of these layers to minimize the error between the predicted and actual output values. After training, the neural network is saved as a function that can be used for making predictions with new data. After training, the performance of the neural network model is evaluated by comparing its predictions to actual GPT simulation results (Fig 5.6). This involves generating predictions for a range of input parameters and comparing these predictions with the actual outcomes from simulations. A common approach for evaluation is to visualize the predicted results against the actual data. This helps in understanding how well the neural network model performs and identifies any discrepancies between the predicted and observed values. The

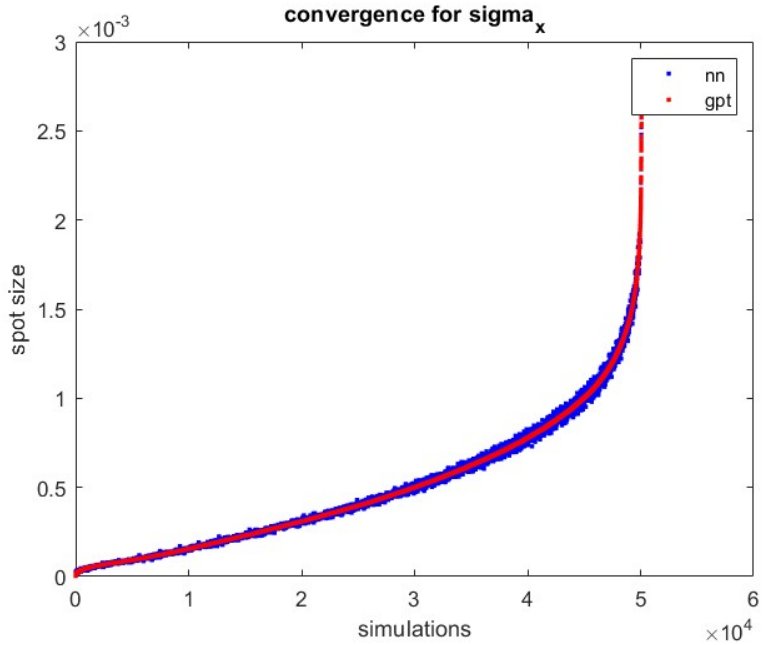

Figure 5.6: Neural network prediction vs GPT 50K simulations.

script includes a testing phase where the neural network model is used to simulate solenoid scans with varying solenoid currents. This phase helps in validating the model's predictions by comparing them with experimental measurements. The results from the neural network are plotted alongside the experimental data to assess the model's accuracy (Fig 5.7). This comparison allows for the identification of any deviations and helps in refining the model if necessary. To ensure the model's accuracy, optimization techniques are employed to fine-tune the model parameters. This involves minimizing the residual errors between the model's predictions and the experimental data. The optimization process is performed using algorithms that adjust the model parameters to achieve

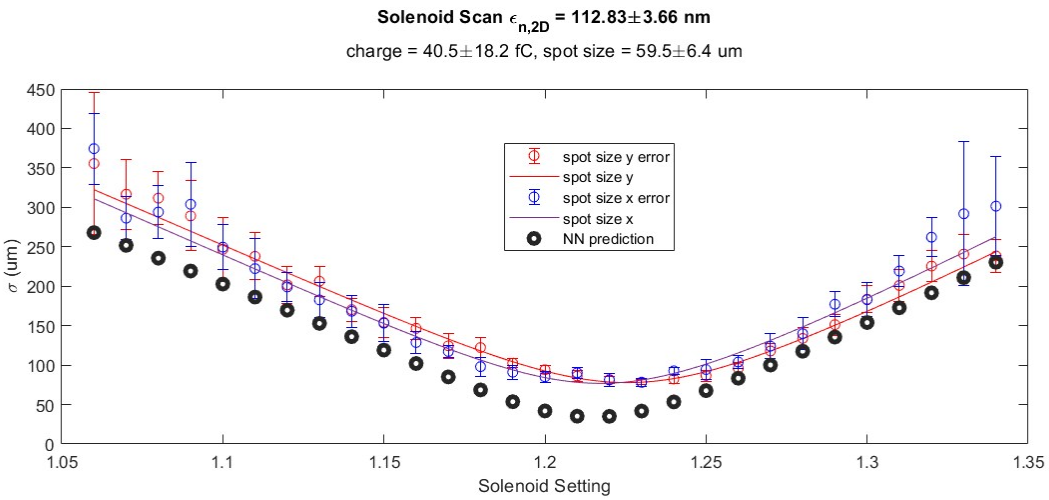

Figure 5.7: Neural network solenoid scan compared with measurement. The black dots are the NN prediction, the blue and red points are the x and y spot sizes respectively. The NN predicts with a good agreement the measurements.

the best fit. The final optimized parameters are evaluated to ensure that the model's predictions are as close as possible to the actual measurements. This approach provides a robust method for predicting and analyzing the performance of the photoinjector based on various input parameters. The goal of MCMC algorithms is to approximate the posterior distribution of your model parameters by random sampling in a probabilistic space. The idea is that we use a number of walkers that will sample the posterior distribution (i.e. sample the Likelihood profile). The goal is to produce a "chain", i.e. a list of values, where each is a vector of parameters for your model. If you start far away from the truth value, the chain will take some time to converge until it reaches a stationary state. Once it has reached this stage, each successive elements of the chain are samples of the target posterior distribution. This means that, once we have obtained the chain of samples, we have everything we need. We can compute the distribution of each parameter by simply approximating it with the histogram of the samples projected into the parameter space. This will provide the errors and correlations between parameters. A Markov chain is a sequence of random variables where the probability of each subsequent variable depends only on the current state. This is known as the Markov property. The Monte Carlo methods rely on repeated random sampling to obtain numerical results, which are useful for estimating properties of complex distributions. While both MCMC sampling and optimization, like the ones in the previous chapters, address the same problem, they approach it differently. An optimizer aims to identify a single point in parameter space that best fits the data. In contrast, MCMC sampling is used to determine the regions of parameter space with the highest probability of aligning with the data. The key to finding the posterior probability given the date is the Bayes theorem. The Bayesian approach assumes that parameters are not fixed but instead have a probability distribution reflecting their uncertainty. A probability distribution is a mathematical function that describes the likelihood of a random variable taking on particular values. This distribution can be discrete (e.g., Bernoulli, Binomial, or Poisson) or continuous (e.g., Gaussian, also known as the normal distribution). The Bayesian method begins with prior beliefs about the system under study, which are then updated as data is collected. The updating process is governed by Bayes' theorem. For simplicity, let's denote the parameter by θ and the observed data

by B. Bayes' theorem then provides a way to estimate the parameter θ given the observed data:

$$\Pr(\theta \mid \text{data}) = \frac{\Pr(\text{data} \mid \theta) \times \Pr(\theta)}{\Pr(\text{data})} \tag{5.2}$$

Let's break down each component of this equation:

- **Posterior Distribution**: This is on the left-hand side and represents what you know about the parameter after seeing the data. This distribution forms the basis for inference and is the primary goal of Bayesian analysis. It can be multivariate if more than one parameter is involved.
- **Likelihood**: This appears on the right-hand side and is the same as in the MLE (Maximum Likelihood approach) approach. Both Bayesian and frequentist methods share this component, which is why their results often align. The likelihood function reflects the information contained in the data, given a model parameterized by θ.
- **Prior Distribution**: This term represents what you knew about the parameter before observing the data. The choice of prior can be a subject of debate. If little is known about θ, the prior may be vague. However, typically, you would use a prior that reflects existing knowledge.
- **Marginal Likelihood** Pr(data): Also known as the average likelihood, this is obtained by integrating the likelihood over the prior distribution:

  $$\Pr(\text{data}) = \int \mathcal{L}(\text{data} \mid \theta) \Pr(\theta)\, d\theta. \tag{5.3}$$

  This integration ensures that the posterior distribution is normalized to one, making it a proper probability distribution. Calculating this integral can be challenging, especially as the number of parameters increases. This complexity is one reason why Bayesian methods were less commonly used until the advent of modern computational algorithms.

When implementing MCMC, one of the key tasks is determining the burn-in period—the number of initial iterations to discard before the Markov chain converges to the target distribution. Additionally, it's important to decide how many iterations are required after convergence to obtain reliable Monte Carlo estimates, such as posterior means and credible intervals. In practice, we discard the initial observations from the Markov chain (burn-in) and use only the observations from the post-convergence period. The simplest method for determining the length of the burn-in period is by inspecting trace plots. Preliminary MCMC runs are typically performed to determine the appropriate length of the burn-in period, the burn-in period is 0.01 While inspecting the trace plot (Fig 5.8) for a single run is useful, it's common practice to run the Markov chain multiple times, each starting from different over-dispersed points. This helps ensure that all chains converge to the same stationary distribution. Once the burn-in period is determined, the next question is how long the chain should be to yield reliable parameter estimates. Successive steps in a Markov chain are not independent, a phenomenon known as autocorrelation. Trace plots can be used to diagnose potential issues to minimize autocorrelation. Trace plots for different values of the standard deviation of the normal proposal distribution can reveal how autocorrelation behaves (Fig 5.9, Fig5.10).

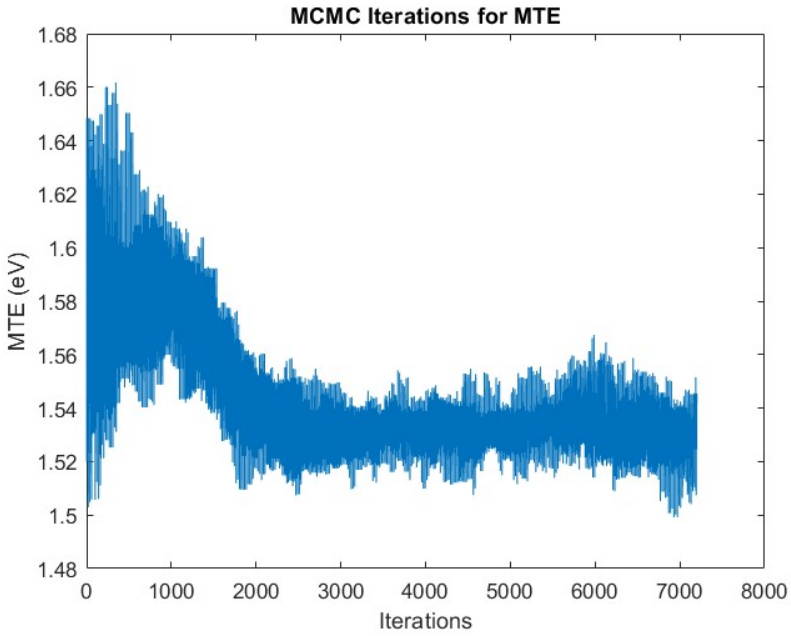

Figure 5.8: Example of walker convergence for MTE. The walkers first spread out and finally converged.

Additionally, Autocorrelation Function (ACF) plots are helpful for visualizing the strength of autocorrelation across sampled values at increasing lags. In summary, using Bayes' theorem, you

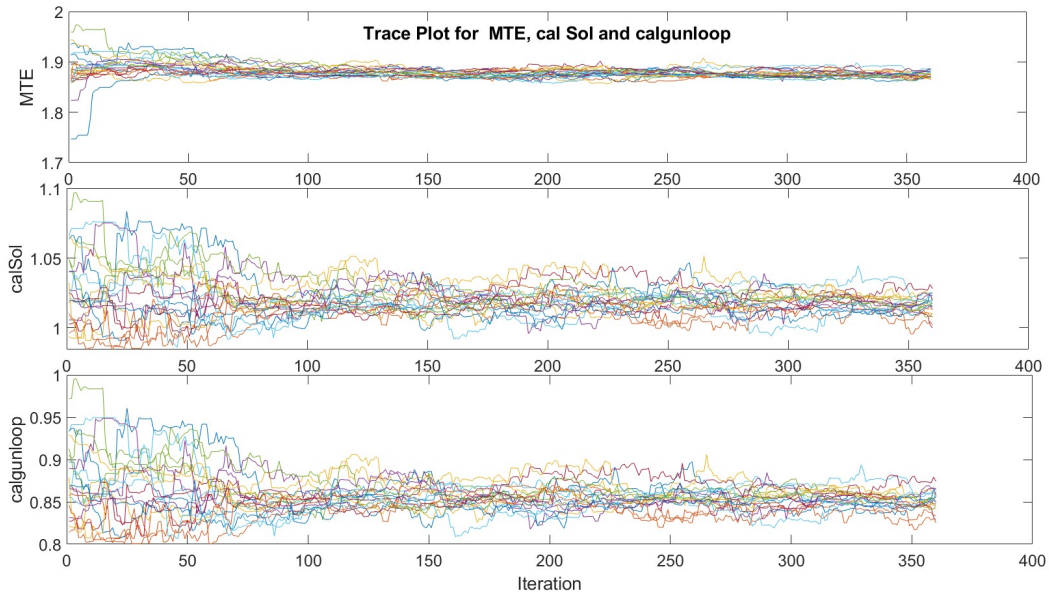

Figure 5.9: The trace plot displays how values of parameters change across MCMC iterations. The x-axis represents the iterations or sampling steps, while the y-axis shows the parameter value.

update your beliefs (prior) with new data (likelihood) to obtain posterior beliefs (posterior):

$$\text{posterior} \propto \text{likelihood} \times \text{prior}.$$

The concept behind MCMC is to simulate values from a Markov chain with a stationary distribution equal to the posterior distribution you are interested in. In practice, you run a Markov chain multiple times, each time starting from over-dispersed initial values. You discard iterations during

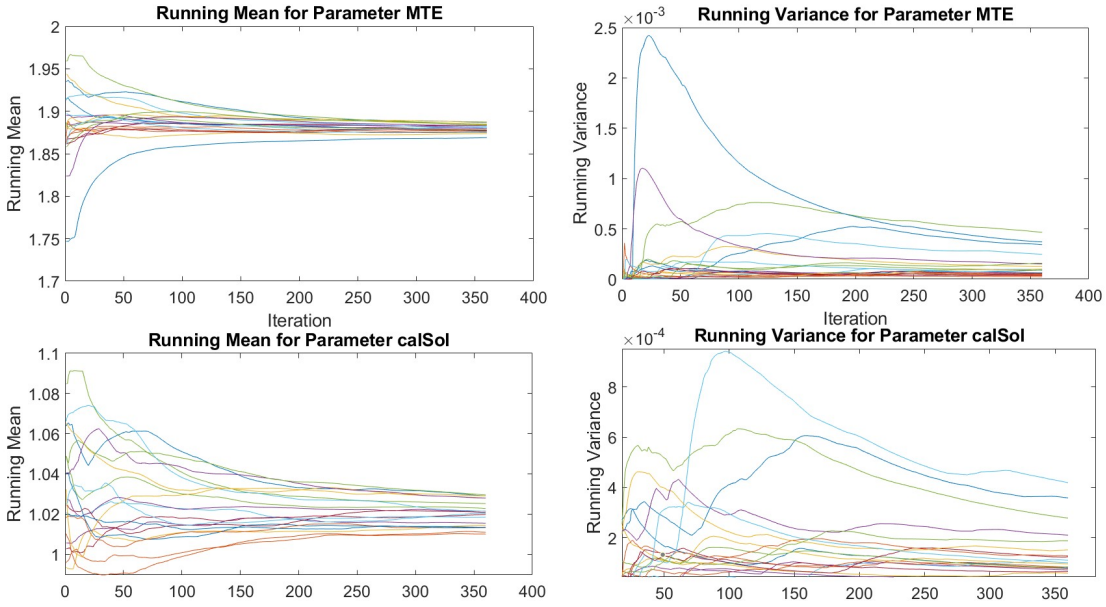

Figure 5.10: Running mean tracks the average value of the parameter over time. A stable running means indicates that the parameter estimates are converging to a value. Running variance tracks how the variance of the parameter estimates changes over time. A decreasing running variance indicates that the estimates are becoming more stable and concentrated around the mean.

an initial burn-in phase and achieve convergence when all chains reach the same regime. From there, you run the chains long enough to calculate Monte Carlo estimates of numerical summaries (e.g., posterior means and credible intervals) for the parameters. Some tools can be used to assess the chain convergence, one of these is the Gelman-Rubin statistic. The Gelman-Rubin $\hat{R}$ statistic is a diagnostic tool used in MCMC simulations to assess the convergence of chains [82] [83] [84]. If the chains have converged, they should have similar variances both within and between chains. The $\hat{R}$ statistic compares these variances to evaluate convergence. analysis using MCMC, you might start with several chains from different initial points. If the chains are truly sampling from the same distribution, they should eventually converge and produce similar results. The $\hat{R}$ statistic assesses this convergence. Now the step for the calculation of Gelman-Rubin $\hat{R}$

1. **Within-Chain Variance (W)**:

$$W = \frac{1}{G}\sum_{g=1}^{G} s_g^2 \tag{5.4}$$

   Where G is the number of chains and s_g^2 is the variance of samples in chain g.

2. **Between-Chain Variance (B)**:

$$B = \frac{n}{G-1}\sum_{g=1}^{G}(\bar{x}_g - \bar{x})^2 \tag{5.5}$$

   Where $\bar{x}_g$ is the mean of samples in chain g and $\bar{x}$ is the mean of the means of the chains.

3. **Estimate of Overall Variance ($\hat{\sigma}^2$)**:

$$\hat{\sigma}^2 = \frac{n-1}{n}W + \frac{1}{n}B \tag{5.6}$$

4. **Gelman-Rubin Statistic ($\hat{R}$)**:

$$\hat{R} = \sqrt{\frac{\hat{\sigma}^2}{W}} \tag{5.7}$$

- $\hat{R} \approx 1$: Indicates that the chains have likely converged to the same distribution(Fig 5.11 and Tab 5.1.
- $\hat{R} > 1$: Suggests that the chains might not have converged and that more iterations might be needed (Fig 5.12 and Tab 5.2).
- $\hat{R} < 1$: This is rare and might indicate errors in the calculation.

MTE	calSol	VCCcal	tau	calgunloop	phaseoffset	calQ	pixscreen
1.0556	1.0957	1.0255	1.0838	1.0848	1.1593	1.0075	1.0574

Table 5.1: Gelman-Rubin $\hat{R}$ for a converging chain.

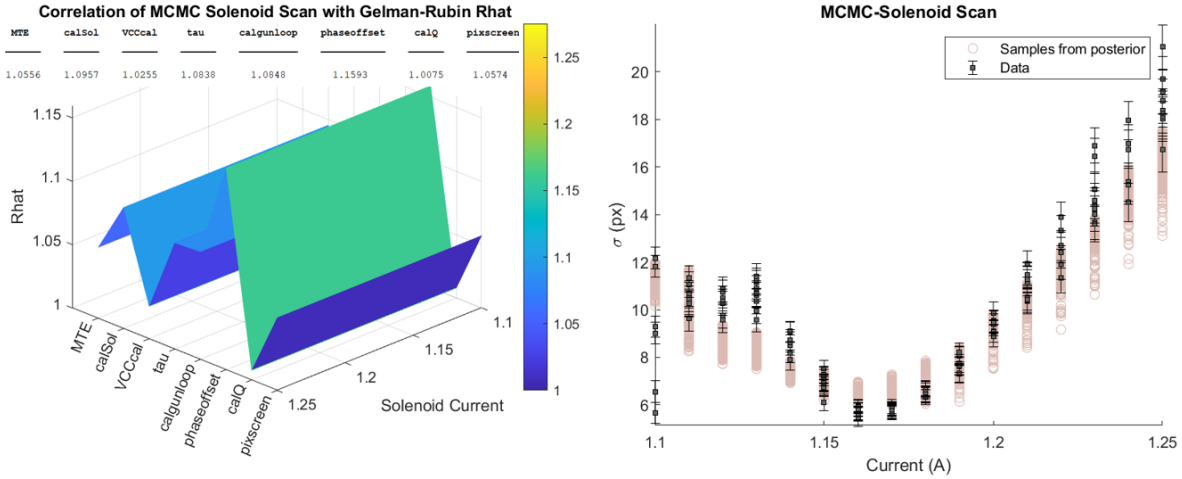

Figure 5.11: Correlation between Gelman-Rubin $\hat{R}$ and MCMC solenoid scan. $\hat{R} \approx 1$ indicates that the chain converges.

MTE	calSol	VCCcal	tau	calgunloop	phaseoffset	calQ	pixscreen
18.74	2.6274	1.1213	1.1993	2.2315	1.2392	1.3773	1.1988

Table 5.2: Gelman-Rubin $\hat{R}$ for a non-converging chain.

Several solenoid scans were analyzed using the previously described model to estimate MTE. The Results of the analysis are presented in the following graphs. The model was tested on two different cathodes, copper and yttrium with 266 nm laser wavelength. The model prediction was compared with the "classical" linear fit model for MTE estimation (Fig 5.13). The clear markers are the MCMC prediction, the black ones are the data with the corresponding errors (Fig 5.14 5.15). Applications of this optimization method, MCMC, and advanced virtual diagnostics have been extensively studied in this doctoral thesis [85], where this algorithm has been applied to various beamlines. The results obtained have motivated the use of this technique for the PEGASUS laboratory as well.

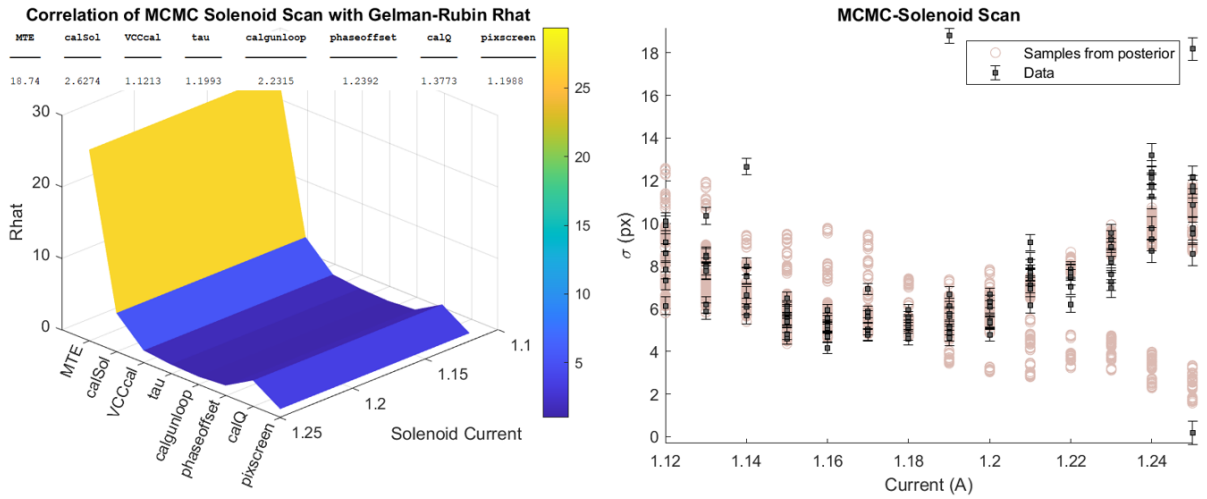

Figure 5.12: Correlation between Gelman-Rubin $\hat{R}$ and MCMC solenoid scan. The chains have not converged as the MCMC solenoid scan plot also shows.

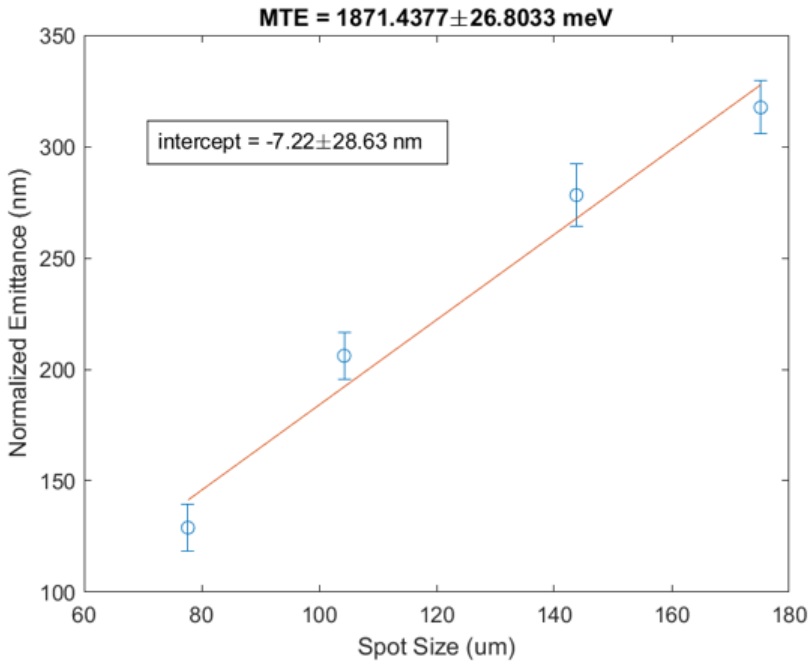

Figure 5.13: MTE measured with a linear fit. Each point is a solenoid scan analysis to retrieve the emittance measurement.

5.1.2 Measurements and characterization of different cathode materials at different wavelengths

The following section will report a series of measurements aimed at characterizing different cathodes at various wavelengths. The types of cathodes studied include: Copper, Yttrium, and Sodium Potassium Antimony. The family of alkali-metal-antimonide photocathodes encompasses a diverse range of compositions, combining various alkali metals with antimony (Sb). This group includes several well-known photocathodes such as cesium antimonide (Cs_3Sb), potassium cesium antimonide (K_2CsSb), sodium potassium antimonide (Na_2KSb), and sodium potassium antimonide with cesium ($Na_2KSb(Cs)$). These photocathodes are extensively used in particle accelerator systems due

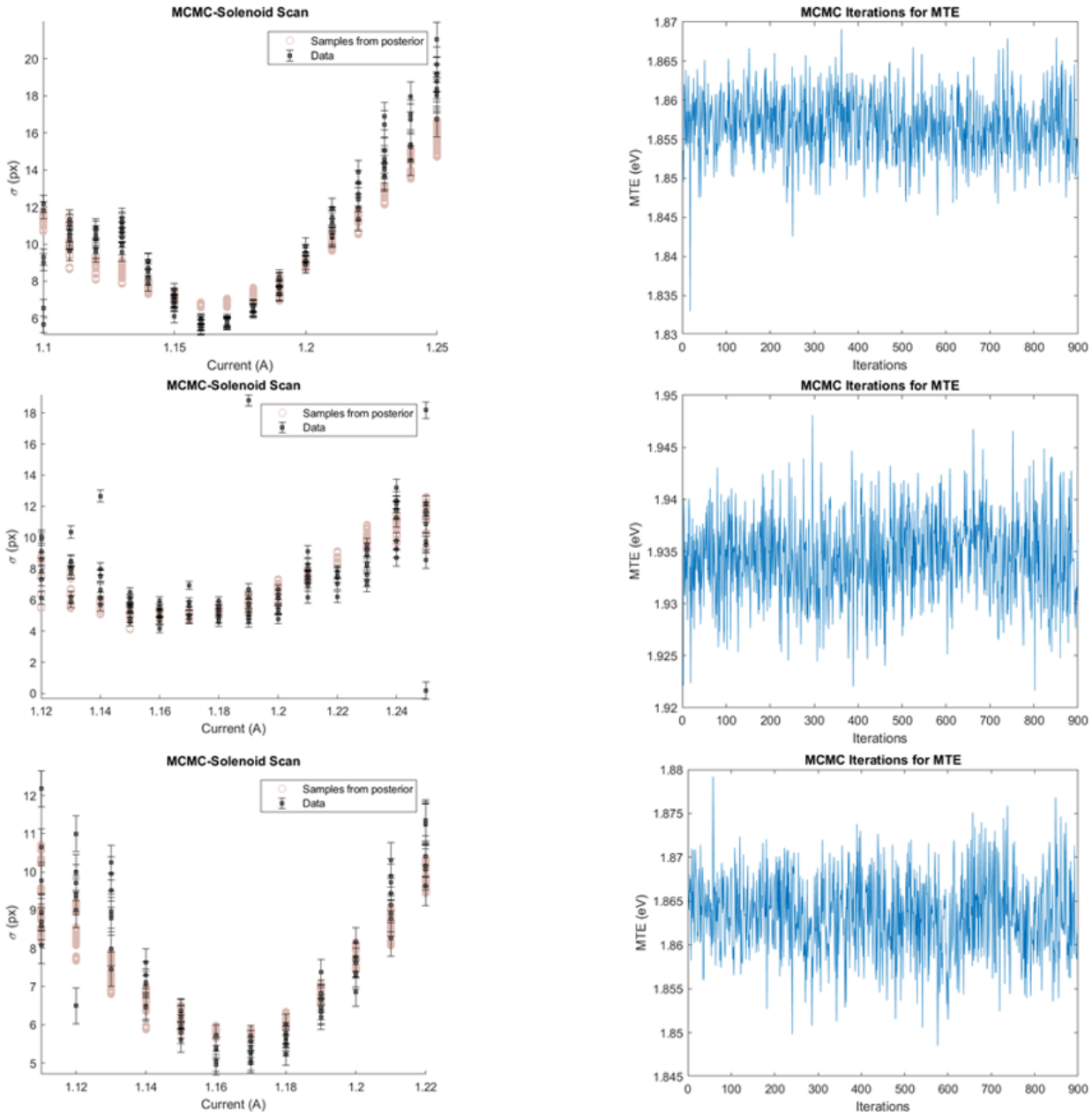

Figure 5.14: MTE predicted with MCMC, all the solenoid scans of the linear fit have been analyzed with the algorithm. The MCMC shows a good agreement with the measurements (copper cathode).

to their favorable emission properties. The photoemission properties of sodium potassium antimony (NaKSb) photocathodes grown at Cornell were measured at high gradients in the UCLA Pegasus S-band photoinjector. These measurements were enabled by the flexible suitcase-load lock system, which has been developed in the last few years based on the INFN-style design and cathode plugs. Preliminary measurements have been carried out using UV (266 nm) laser pulses, which were readily available to illuminate the cathode. The quantum efficiency was measured to be 1.5% at 266 nm and was shown to have a degradation time of around 4.5 days. Dark current was measured with accelerating gradients of up to 75 MV/m. NaKSb is a multi-alkali antimonide semiconductor that was shown to be a good photo emitter in the 1950s [86]. These air-sensitive crystals form with stoichiometry M_3Sb, where M is an alkali metal [87]. The work function is expected to be around

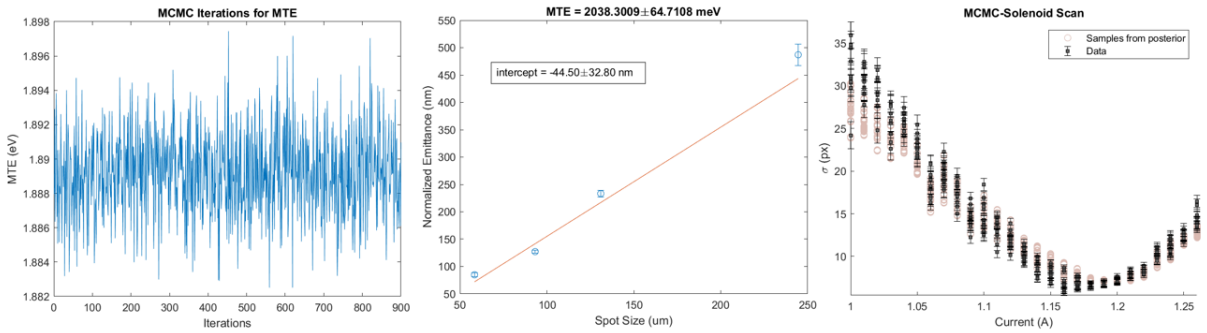

Figure 5.15: MTE predicted with MCMC, now looking only to one solenoid scan taken with the same cathode as previous figure Fig 5.14. The MTE prediction is 1.9 and the calculated one is 2.

1.75–2 eV [87–90]. Of the two NaKSb photocathodes grown at Cornell and transported to UCLA, one was on a molybdenum substrate plug and the other on a copper plug, likely with stoichiometry NaK_2Sb. These were flown to UCLA in the UHV suitcase for testing at high gradients. The molybdenum plug cathode was visibly accessible in the suitcase and was used to monitor the degradation of the quantum efficiency (QE) over time (Fig 5.16) by reading the photocurrent created when a diode laser was focused onto the cathode. Wavelengths from 405 to 532 nm were used. The largest decreases in QE were observed at the times corresponding to transport to UCLA and transfer into the gun. After installing the copper plug cathode in the Pegasus gun, we used the 100 fs, 266 nm

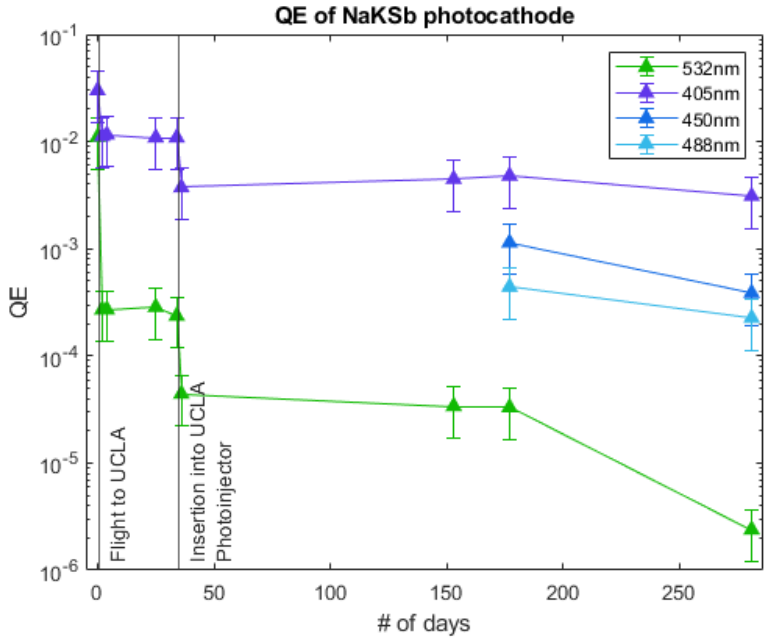

Figure 5.16: QE measured in the UHV suitcase using diode lasers from 405-532 nm.

laser pulse from the photoinjector drive laser to test the cathode properties. An initial QE of 1.5% was measured at 75 MV/m peak field. Using the SQL database that logs data from Pegasus, we were able to passively monitor the QE over multiple days while the facility was running other experiments, obtaining a characteristic lifespan of 4.5 days, as shown by the solid line fit to the first five points (Fig. 5.17). After many days, the QE reached a saturation floor (Fig. 5.17 dashed line), which lies above the QE of polycrystalline copper. Many factors in the violent environment of the

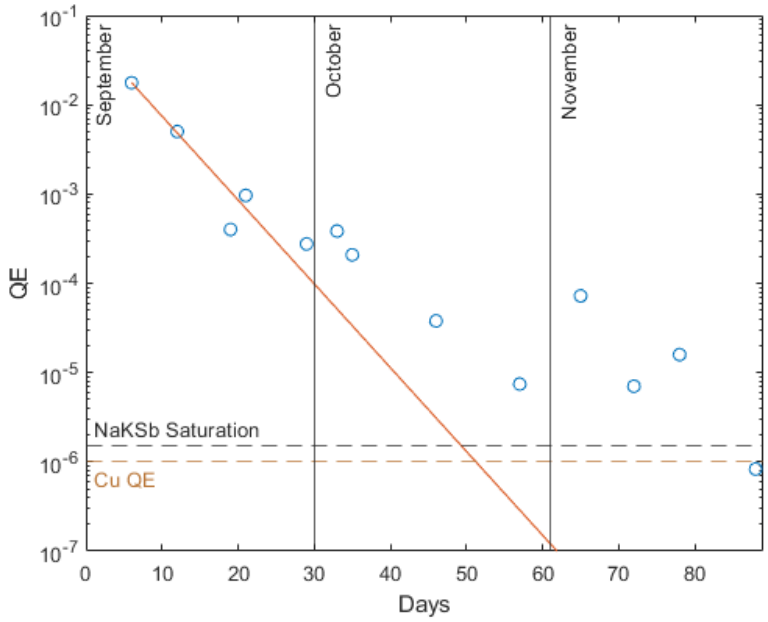

Figure 5.17: QE measured at 266nm during the cathodes lifetime in Pegasus.

RF photoinjector degrade the QE of these alkali antimonide cathodes. The alkali metals in these semiconductors are very sensitive to air, so poor vacuum conditions alter the surface chemistry, degrading the QE. If the cathode plug does not sit flush with the backplane of the gun, the RF cavity will be detuned from resonance. At Pegasus, they tune the cavity back to resonance with temperature, and any increase in temperature degrades the QE further. Measurements of the dark current were also made where field emission current was focused onto a calibrated screen as the accelerating gradient was increased to measure the charge extracted at a given field created by a 2.5 µs RF pulse. We plotted this against field emission from other photocathodes tested at UCLA (Fig. 5.18) including copper, cesium antimony (CsSb), and previous NaKSb photocathodes. The range of past data sets does not overlap as they were taken when the gun was powered by a PFN klystron amplifier, which was slightly more powerful but less stable than our current solid-state modulator. These low work function photocathodes display more field emission than metals, as expected. The most recent data set from 2024/05/13 was taken with a 3 µs pulse during conditioning of the gun, which explains why we see more charge from this NaKSb cathode compared to previous ones. Pure metal photocathodes, such as copper (Cu), are characterized by their high work functions, which necessitate the use of ultraviolet (UV) light for their operation [11]. This requirement represents a significant drawback, particularly for high average current applications where UV light is less practical. Despite this limitation, metal photocathodes offer several notable advantages. One of the most significant advantages is their exceptional robustness. Metal photocathodes can endure prolonged operational periods, often lasting several years, without significant degradation in performance. This durability makes them particularly suitable for long-term use in demanding environments. Another advantage of metal photocathodes is their simpler preparation process compared to semiconductor photocathodes. The fabrication and handling of metal photocathodes are generally less complex and less sensitive to contamination, which can be advantageous in various practical applications. In summary, while pure metal photocathodes require UV light

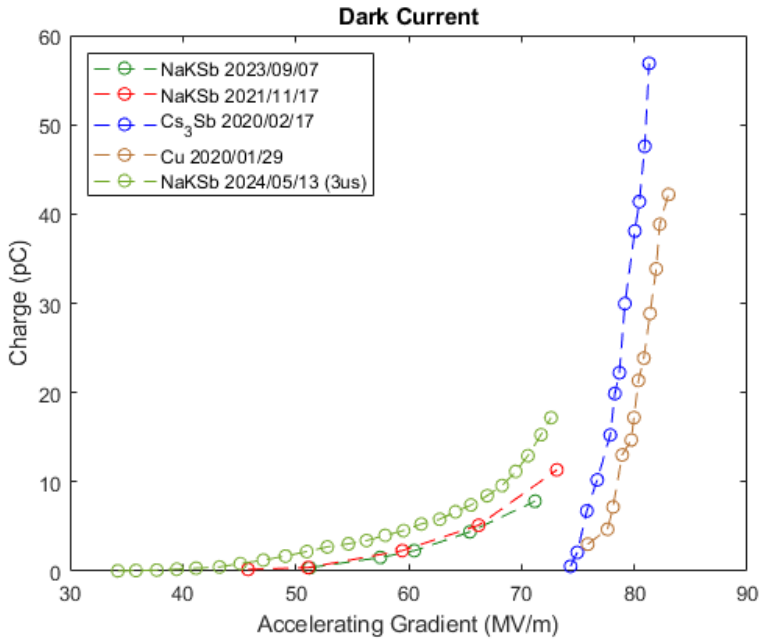

Figure 5.18: Dark current measured from NaKSb and other photocathodes. Measurements from 2020 used a more powerful PFN-modulated Klystron amplifier to power the gun.

Figure 5.19: Copper cathode used for the measurements.

and have a higher work function, their robustness and relatively straightforward preparation make them valuable for specific applications where long-term stability is crucial. Metal photocathodes generally exhibit relatively low QE values, typically in the range of 10^{-4} to 10^{-1}, compared to their semiconductor counterparts. This reduced efficiency is primarily attributed to the energy loss that

occurs during scattering events, with only electrons possessing a mean free path of approximately one electron wavelength being able to escape into the vacuum. The photoemission process in metals is predominantly confined to the first few surface layers of the material. This characteristic implies that the quantum efficiency of metal photocathodes is highly sensitive to surface quality. The exposure of metal photocathodes to air is less detrimental, consequently, metal photocathodes experience a smaller decrease in QE following brief exposure to air. However, prolonged exposure to gases can lead to oxidation of the metal surface. This oxidation results in changes to the surface work function, which in turn adversely affects the quantum efficiency. Measurements were conducted to evaluate the intrinsic emittance and MTE for the copper cathode (Fig 5.19). The following plots illustrate the results of these measurements. In Fig 5.20, solenoid scans were performed to determine the emittance of the electron beam. The electron beams studied had charges ranging from tens to a few hundred femtocoulombs, carefully chosen to minimize any contributions from space charge effects, thereby allowing an accurate determination of the intrinsic emittance. For these measurements, a constant charge density (i.e., the ratio of charge to the spot size at the cathode) was maintained. This approach was crucial, as it was observed that keeping a consistent charge density allowed for a more linear fit of the MTE as a function of the emitted charge. This consistency enhances the reliability of the intrinsic emittance measurements, as it reduces variables that could distort the linear relationship. In Fig 5.22, the comparison between the two transverse planes for the various solenoid scans is shown, with the solenoid current normalized to the waist value. The third plot in Fig 5.22 demonstrates the impact of the increased extracted charge on emittance growth. As expected, a rise in the extracted charge leads to a notable increase in the measured emittance due to space charge effects becoming more pronounced. This observation underscores the importance of operating within the low-charge regime to accurately extract the intrinsic properties of the cathode material, particularly when evaluating factors like thermal emittance. In the same operational mode, the influence of space charge forces on emittance was evaluated, as shown in the figures. In the constant spot solenoid scans (225 um), it is observed that higher emittance values are correlated with increased extracted charge (Fig 5.23). This trend is expected because, at a constant spot size on the cathode, raising the charge intensifies the space charge forces within the beam. These forces lead to greater mutual repulsion among the electrons, causing the beam to diverge more significantly and, consequently, increasing the measured emittance. On the other hand, when maintaining a constant extracted charge (60 fc) while varying the spot size at the cathode (as seen in Fig 5.24), a clear relationship emerges: smaller spot sizes at the cathode result in lower measured emittance values. This is due to the fact that reducing the spot size concentrates the emitted electrons, thereby decreasing the initial beam divergence. A smaller initial beam divergence results in a lower thermal emittance, which is closely tied to the intrinsic properties of the cathode material and the MTE of the emitted electrons. In essence, for a fixed charge, decreasing the spot size confines the electrons to a more focused initial distribution, reducing the effective thermal emittance. This makes the initial phase space distribution narrower, leading to a reduction in the overall emittance. However, it's important to note that at extremely small spot sizes, space charge forces can once again become significant even for a constant charge. In this case, a denser distribution of electrons can increase localized space charge effects, which may counteract some of the gains in reducing thermal emittance. Therefore, an optimal spot size must be chosen to balance space charge effects with the desire for lower thermal emittance. These observations highlight the importance of carefully

controlling both the charge and the spot size on the cathode when aiming to minimize emittance for specific applications. Lower emittance is desirable for achieving high beam quality, particularly in accelerator applications where precise beam focusing and minimal beam spread are crucial. Thus, understanding the interplay between extracted charge, spot size, and space charge forces is fundamental in optimizing the performance of photoinjector sources. Y-based photocathodes are

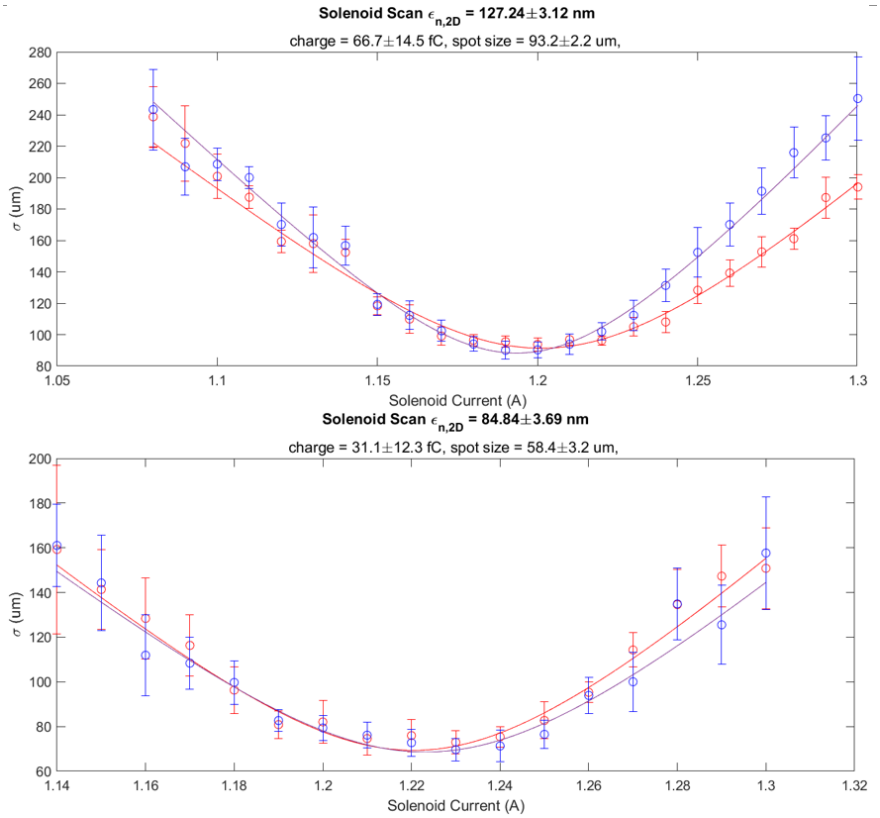

Figure 5.20: Solenoid scan realized at constant charge density for emittance calculation.

particularly advantageous due to their ability to be illuminated by visible laser pulses. This capability offers several benefits, including the potential for higher energy per pulse, which facilitates the development of high repetition rate photoinjectors using conventional laser sources. Operating with a wavelength (λ) around 400 nm allows these photocathodes to benefit from a smaller energy difference between the work function of the photocathode and the photon energy of the laser. This reduced energy gap minimizes the contribution of intrinsic emittance from the material, improving the overall performance of the photocathode. Moreover, utilizing visible light for photoemission obviates the need for converting laser light to higher harmonics, which is typically required in other systems. This direct approach enhances the energy per pulse of the laser, enabling the generation of electron bunches with higher charge densities. In summary, Y-based photocathodes provide significant advantages in high repetition rate applications due to their efficient use of visible light and the resulting reduction in intrinsic emittance, while also maximizing the available charge per electron bunch. Moving now to the measurements made with yttrium (Fig 5.25), the same analysis made on the previous cathode will not be reported but rather an analysis made with tunable wavelength lasers. An instrument called PALITRA was used to tune the wavelength of the laser (Fig 5.26). The Palitra tunable light source is a valuable tool for conducting photoemission studies on cathodes, allowing precise control of the wavelength of light used to investigate the electron emission

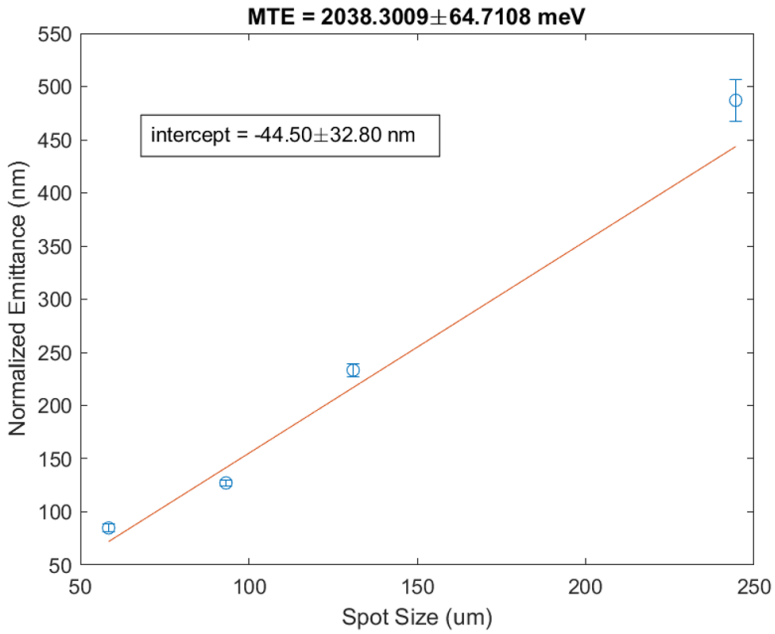

Figure 5.21: MTE calculation from the Fig 5.20 solenoid scans. The MTE has been calculated with the equation (5.1)

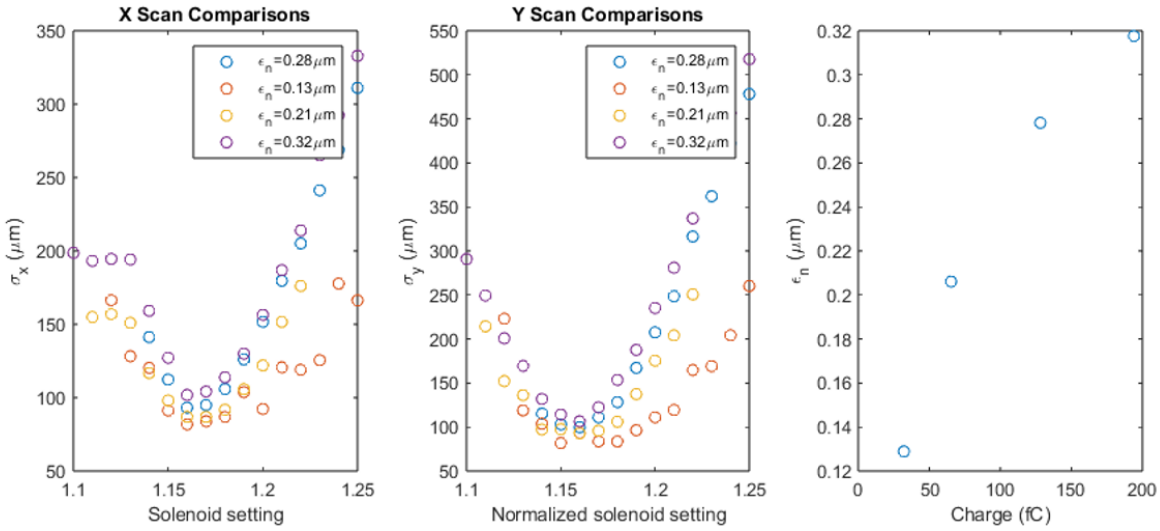

Figure 5.22: Solenoid scan for emittance measurements in both transverse plane.The measurement has been done at constant charge density. The last plot shows the emittance growth due space charge forces

properties of various cathode materials. This precision is critical for understanding the underlying mechanisms of photoemission and optimizing cathode performance. The Palitra-FS Series of Optical Parametric Amplifiers (OPAs) stands out in the market for its exceptional capabilities, offering the widest gap-free tuning range of 230 nm to 22 µm and achieving high conversion efficiency of over 40% at peak performance. The Palitra is a high-efficiency OPA that converts 800nm pulses from a Ti:Sapph laser into tunable pulses. The Palitra used to be pumped by a 5mJ laser Ti:Sapph laser Estrella, during the experiment was pumped by a 1mJ Ti:Sapph laser. This unique combination of features makes the Palitra-FS an ideal choice for a variety of scientific applications. The Key

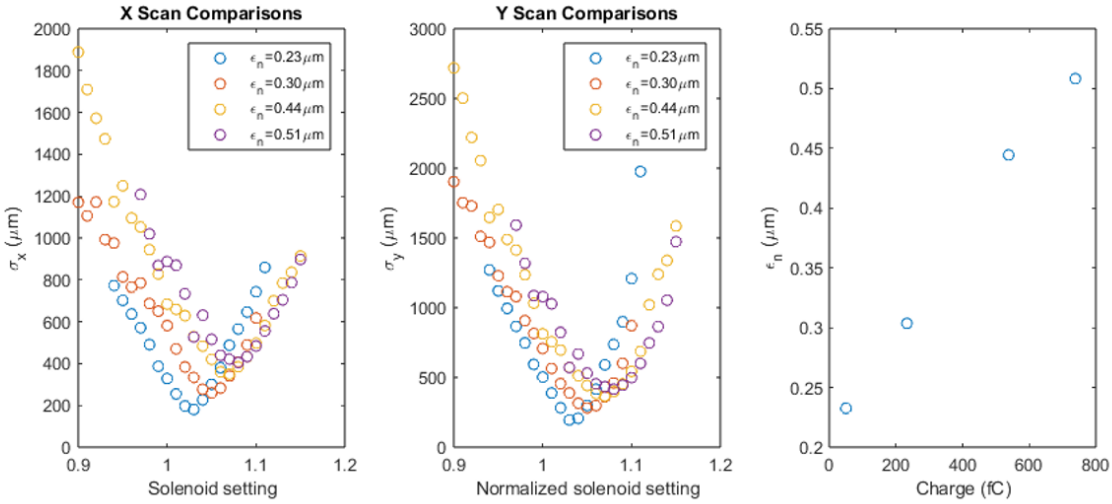

Figure 5.23: Solenoid scan for emittance measurements in both transverse planes.The measurement has been done at constant laser spot, 224 um. The last plot shows the emittance growth due to space charge forces.

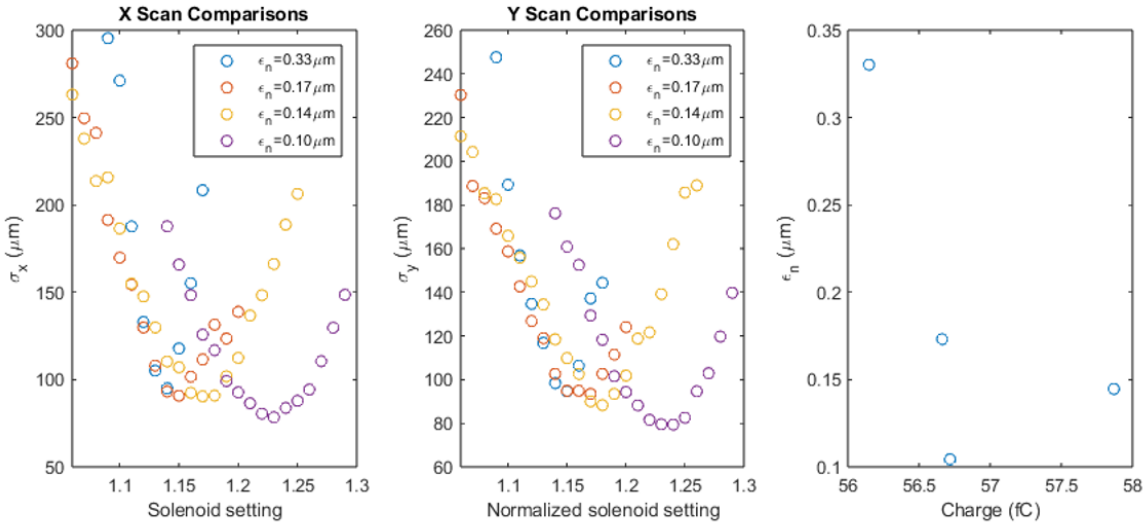

Figure 5.24: Solenoid scan for emittance measurements in both transverse plane. The measurement has been done at a constant charge, 57 fc. The last plot shows that for a fixed charge, decreasing the spot size confines the electrons to a more focused initial distribution, reducing the effective thermal emittance.

Features are:

- **Broad Tuning Range:** The extensive tuning range allows researchers to explore a wide spectrum of wavelengths without the need for additional equipment, making it suitable for diverse experimental requirements in fields such as spectroscopy, microscopy, and material science.

- **High Conversion Efficiency:** With a conversion efficiency exceeding 40% at peak, the Palitra-FS maximizes output power, ensuring effective signal amplification while minimizing noise, which is critical for high-precision measurements.

Figure 5.25: Yttrium sputtered onto copper INFN plug by the Aerospace Corporation, plasma cleaned to remove surface impurities.

- **Compact and Thermally Stabilized Design:** Housed in a compact, thermally stabilized enclosure, the Palitra-FS ensures reliable, hands-free performance. This design mitigates thermal drift and provides consistent output, enhancing experimental repeatability and accuracy.
- **White-Light Continuum Seeded:** The Palitra-FS operates as a white-light continuum (WLC) seeded, collinear OPA. This configuration allows for seamless wavelength tuning while maintaining pulse quality, enabling femtosecond pulse generation across the entire tuning range.
- **Flexible Upgrade Options:** The Palitra-FS Series is designed with flexibility in mind, offering several easily upgradeable extensions and options. This adaptability allows users to customize their systems to meet the evolving demands of cutting-edge ultrafast scientific research.
- **Palitra-Duo FS Integration:** The Palitra-Duo FS:FS configuration integrates two Palitra-FS OPAs into a single enclosure, sharing the same seed. This setup optimizes coherence between the OPA outputs, providing enhanced stability and consistency in dual-wavelength experiments.

The benefits are:

- **Versatility:** The ability to tune across a broad spectrum and customize configurations makes the Palitra-FS suitable for a wide range of applications, from fundamental research to practical industrial uses.

- **Enhanced Experimental Control:** With high efficiency and stability, researchers can achieve better control over experimental parameters, leading to more precise and reproducible results.
- **Cost-Effective Performance:** The combination of a wide tuning range and high conversion efficiency ensures that researchers receive maximum value from their investment, minimizing the need for multiple systems.

Table 5.3: Features of Optical Parametric Amplifiers

Extension	Tuning Range (nm)	Conversion Efficiency (%)	Polarization
UV3	230-280	>1 / >2 (20-70 fs / 70-200 fs)	Vertical
UV2	270-470	>1.5 / >3 (20-70 fs / 70-200 fs)	Horizontal
UV13	340-550	>0.7 / >1.5 (20-70 fs / 70-200 fs)	Vertical
VIS3	460-560	>5 / >8 (20-70 fs / 70-200 fs)	Horizontal
VIS2	530-950	>10 / >14 (20-70 fs / 70-200 fs)	Vertical
VIS1	670-1100	>5 / >8 (20-70 fs / 70-200 fs)	Horizontal
Signal	1050-1900	>23 / >23 (20-70 fs / 70-200 fs)	Horizontal
Idler	1340-2700	>20 / >20 (20-70 fs / 70-200 fs)	Vertical
IR1	2600-11000	>0.7 / >1 (20-70 fs / 70-200 fs)	Vertical
nIR16	2600-11000	>0.9 / >1.2 (20-70 fs / 70-200 fs)	Vertical
IR2	3500-17000	>0.5 / >0.8 (20-70 fs / 70-200 fs)	Vertical
nIR26	3500-17000	>0.7 / >1 (20-70 fs / 70-200 fs)	Vertical
nIR36	13000-22000	>0.15 / >0.25 (20-70 fs / 70-200 fs)	Vertical

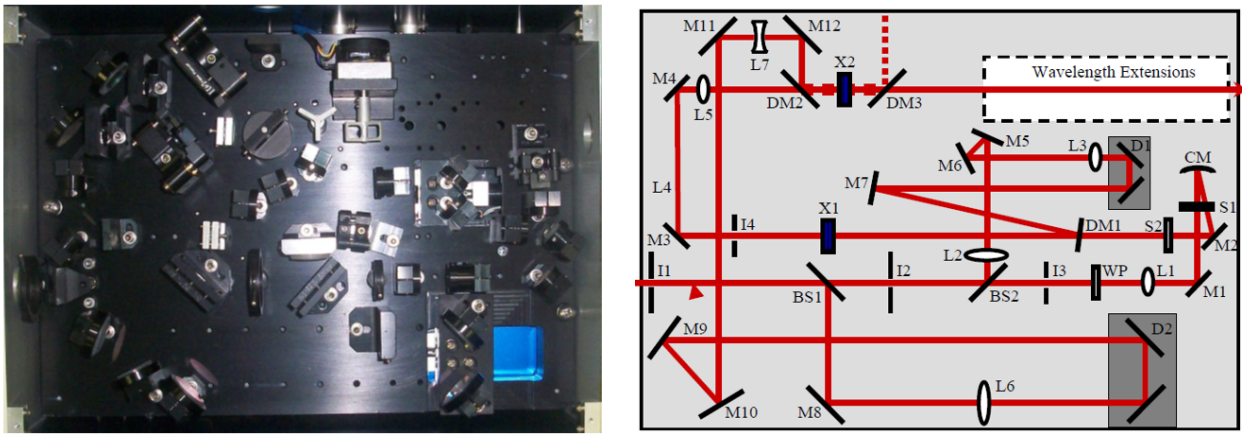

Figure 5.26: Layuout and the optical path of the laser inside the palitra.

Using this instrument, the yttrium cathode was illuminated with different wavelengths, 260, 320, 350, and 375 nm. Tunable wavelength measurements were conducted to extrapolate a reliable photoemission model. The charge scans (Fig 5.27) reveal a curvature characteristic of multiphoton emission, indicating complex behavior during the process. Charge scans on yttrium cathodes demonstrate an increase in emitted charge as the excess photon energy rises. The charge measurements were taken using an Integrating Current Transformer (ICT), though values below 50 fC exhibit significant noise. A calibrated image from our Virtual Cathode Camera (VCC) was utilized to determine the laser pulse energy. The spectral response of this calibration plays a crucial role in ensuring accurate energy measurements, as it directly affects the assessment of the photoemission

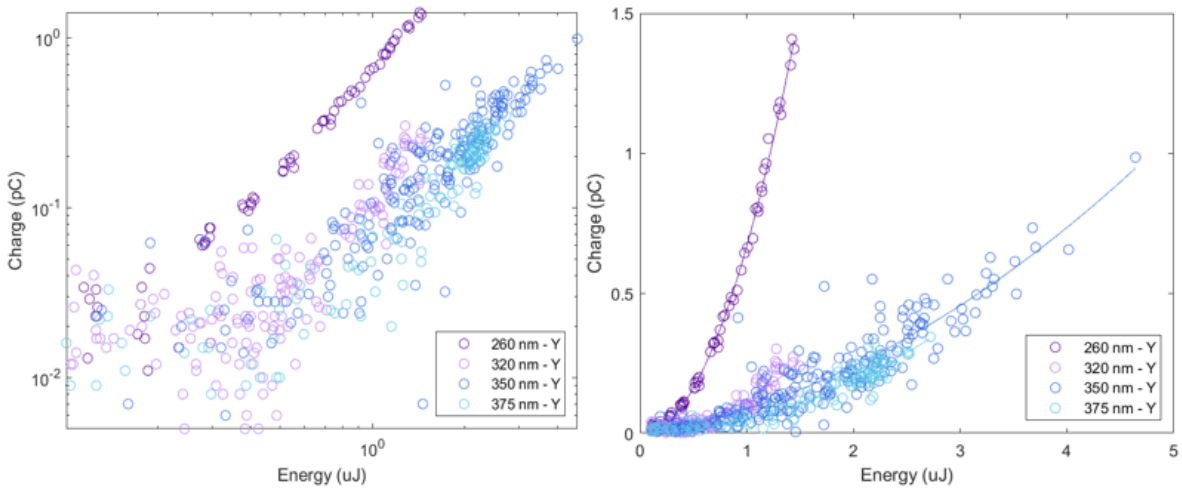

Figure 5.27: Charge scan for different laser wavelength, on the left the linear plot, on the right logarithmic plot to better have a look at the emission regime .

characteristics. These preliminary analyses suggest the need for further investigation to develop a precise photoemission model, Fowler-DuBridge-like [91], which is essential for accurately evaluating the potential advantages of transitioning to yttrium cathodes as described earlier. Photoemission studies on yttrium were conducted at the Cavity Test Facility (CTF) of Elettra Sincrotrone Trieste [73] [92]. The main parameters of the experimental layout are provided in the table and illustrated in Fig 5.28. The experimental setup consists of three main components: the gun (the same for both facilities), a solenoid, and a screen. The primary difference between the CTF and PEGASUS setups lies in the distance between these elements. In the case of CTF, the solenoid is positioned 0.13 m from the gun, and the screen is 1.17 m away Tab 5.4. In the case of PEGASUS, the solenoid is positioned 0.30 m from the gun, and the screen is 1.32 m away Tab 5.5. The results obtained at

Table 5.4: Photoinjector settings and laser parameters for QE and beam emittance measurements at CTF.

Parameters	**Value**
E_{rf}	91 MV/m
Working RF phase	30°
Energy at the gun exit	4.15 MeV
Laser pulse length	1.5 ps - FWHM (Gaussian)
Laser wavelength	$\lambda = 392$ nm
Laser spot size	$\sigma_x = 0.19 \pm 0.02$ mm, $\sigma_y = 0.21 \pm 0.02$ mm

Table 5.5: Photoinjector settings and laser parameters for QE and beam emittance measurements at PEGASUS. Sigmas are referred for the 4 different wavelengths.

Parameters	**Value**
E_{rf}	75 MV/m
Working RF phase	17°
Energy at the gun exit	3.7 MeV
Laser pulse length	100 fs - RMS
Laser wavelength	$\lambda = 260 - 320 - 350 - 375$ nm
Laser spot size	$\sigma_x = 0.10 \pm 0.001$, 0.05 ± 0.006 , 0.06 ± 0.003, 0.07 ± 0.01 mm

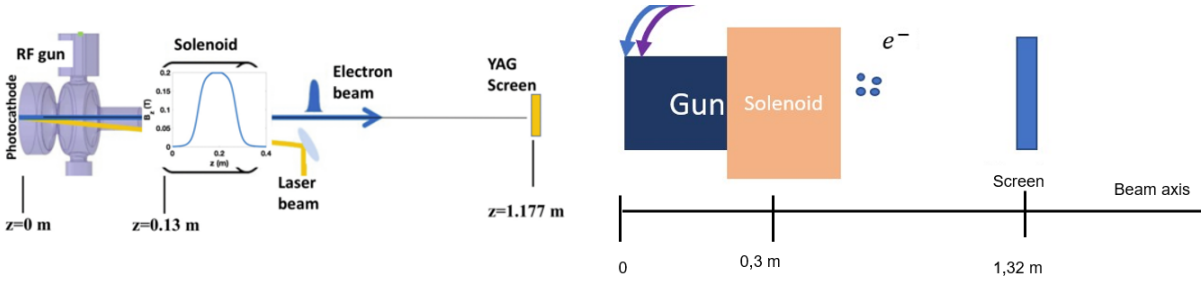

Figure 5.28: CTF layout (left). The solenoid is installed at 0.13 m from the photocathode. After the solenoid and a drift space a screen is placed perpendicular to the electron beam at 1.177m. PEGASUS layout (right). The solenoid is installed at 0.3 m from the photocathode. After the solenoid and a drift space a screen is placed perpendicular to the electron beam at 1.32m (image not in scale).

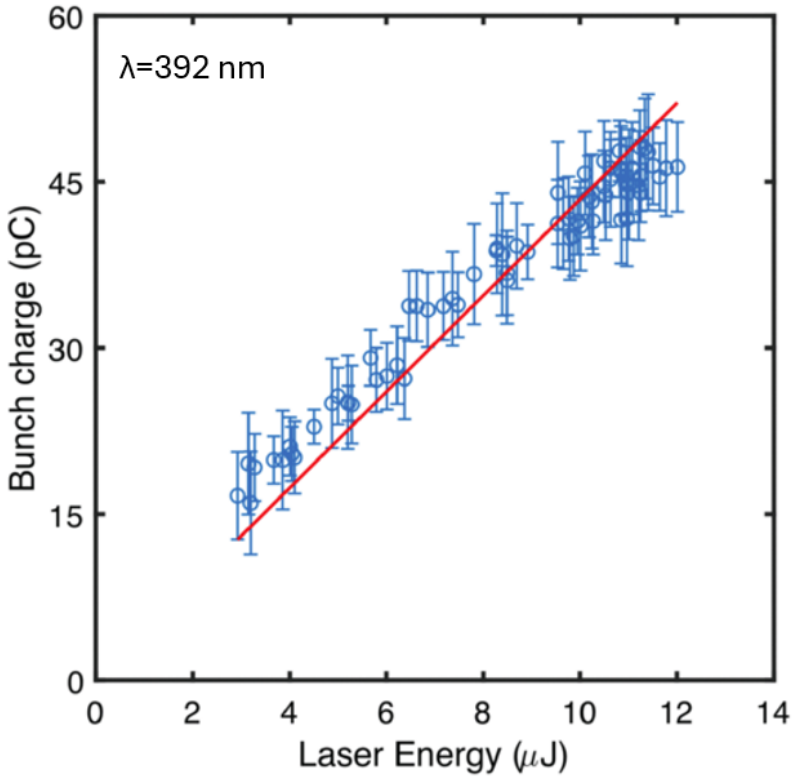

Figure 5.29: Collected charge as a function of the laser energy. The solid red line is the linear fit curve, $QE = (1.3 \pm 0.3) \times 10^{-5}$ [73].

CTF are in good agreement with the theoretical model. They measured a $QE = (1.3 \pm 0.3) \times 10^{-5}$ with respect to $QE = (1.4) \times 10^{-5}$ from the theory. By the way, the results in intrinsic emittance and QE are comparable with the Cu (as reported in the paper), which is opening the way to avoid high harmonic laser conversion. Results obtained at PEGASUS are far from the previous results (Fig 5.30a, 5.30b, 5.31a, 5.31b). The QE is measured in the order of $10^{-}6$. The Gun phase was set to 17 degrees but we did several phase scans (from 10 to 40 degrees), and they gave analogous results. The improvement in the measurement system, VCC upgrade to a UV-sensitive CMOS sensor, pulse stretcher for Palitra to study one photon emission from photocathodes and the analysis

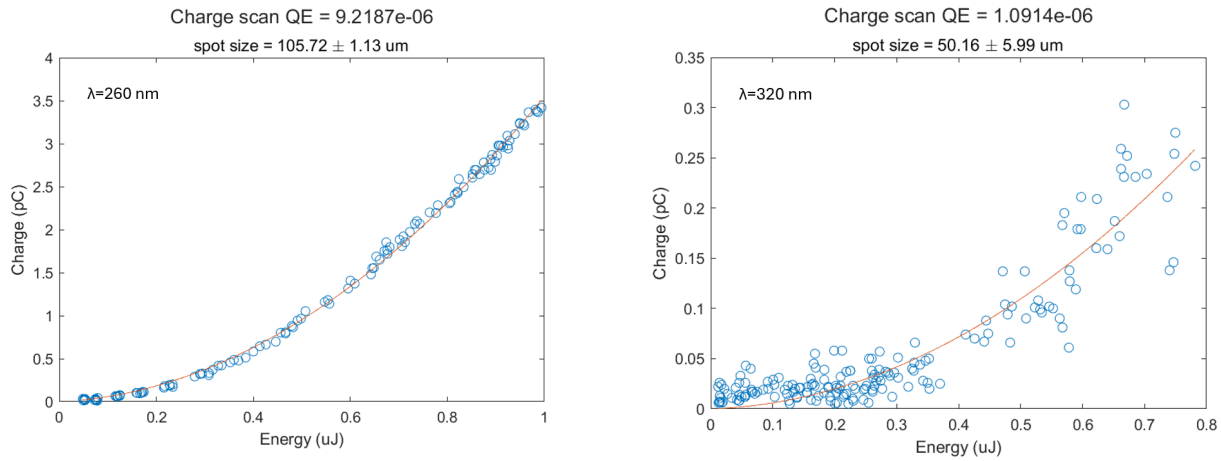

(a) QE measurements for 260 nm wavelength. **(b)** QE measurements for 320 nm wavelength.

Figure 5.30: Collected charge as a function of the laser energy. The solid red line is the fit curve that shows a multiphoton emission regime.

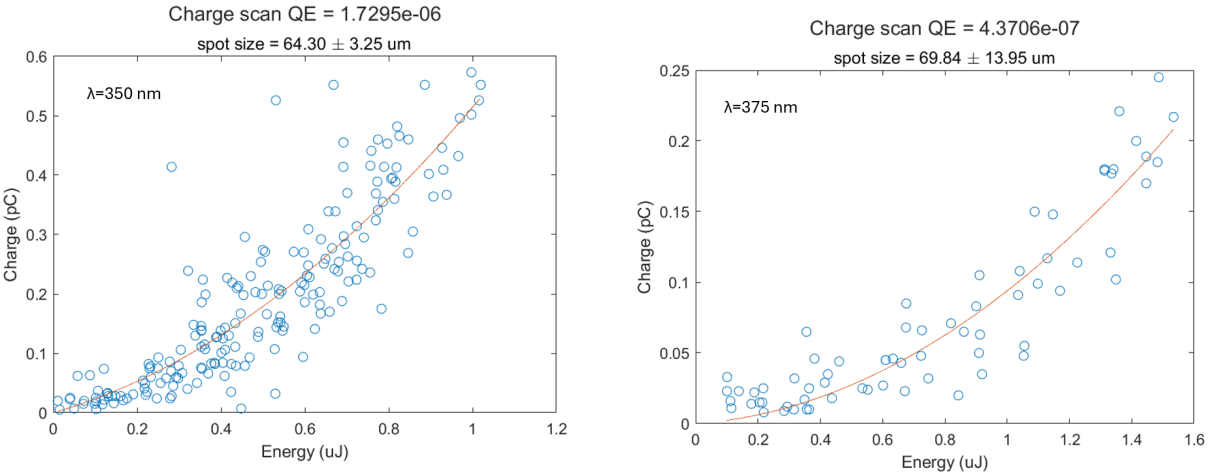

(a) QE measurements for 350 nm wavelength. **(b)** QE measurements for 375 nm wavelength.

Figure 5.31: The solid red line is the fit curve that shows a multiphoton emission regime.

model, images from the virtual cathode camera are numerically integrated to calculate the form factor could improve our results. The relevance of driving photocathodes with variable wavelengths has also been assessed at other facilities worldwide. A study conducted at the SwissFEL Injector Test Facility explores the impact of varying photocathode laser wavelengths on thermal emittance and QE for a copper cathode [93]. The results obtained by me in the PEGASUS laboratory cannot be compared with those previously mentioned due to substantial differences in the measurement layout and the electron source used. Copper was used for SwissFEL, while yttrium was used in the PEGASUS laboratory. Nevertheless, the interest in driving photoinjectors with variable wavelengths has garnered positive feedback within the scientific community, reflecting a shared interest. Regarding the EuPRAXIA@SPARC_LAB project, the work conducted at UCLA within the PEGASUS laboratory is integrated into the doctoral research and thesis as an exploration of alternative beam dynamics approaches. These studies leverage machine learning techniques, which show potential as non-invasive diagnostic systems for low-energy comb beams exiting the GUN, with the prospect of extending their application to the entire machine. The MCMC algorithm, coupled with a surrogate

model of the Gun, demonstrated strong predictive capabilities when compared to the experimental measurements analyzed. The investigation into various cathode materials represents an initial step in selecting the optimal cathode to serve as the beam source for EuPRAXIA. Additionally, the validation of a more sophisticated photoemission model is expected to contribute significantly to the generation of high-quality beams, which are critical for driving the plasma stage. Although the measurements conducted at PEGASUS were performed using electron beams with charges far from those required for EuPRAXIA operational parameters, the finalized model could be scaled to match the facility's target values.

Chapter 6

Conclusions and future perspectives

This work focused on studying electron beam dynamics in advanced RF photo-injectors. I began by defining the quality parameters of electron beams and then explored various techniques for generating high-brightness beams. Utilizing simulation codes and algorithms enabled me to optimize existing machines, such as SPARC_LAB and PEGASUS, while also conducting preliminary studies for future accelerators, specifically the EuPRAXIA@SPARC_LAB injector. The study focused on developing reproducible simulation techniques to generate high-brightness electron beams, primarily for PWFA applications. Utilizing established physical principles and tailored injector requirements for these scenarios, significant results were obtained, contributing to future accelerator development: the optimization of the EuPRAXIA@SPARC_LAB injector starting from the machine baseline and adding an HHC to improve beam separation; the study of the final focusing for the SPARC linac to optimize the plasma injection spot; the investigation of an advanced C-band injector for high-repetition-rate operations; machine learning studies for advanced diagnostic systems; studies on photoemission models to characterize cathodes made of different materials. The core of this thesis was the EuPRAXIA@SPARC_LAB injector. The research began with the optimization of the comb's working point, using the ASTRA tracking code alongside the GIOTTO genetic algorithm. Further enhancements to the machine's performance were achieved with the integration of a high-harmonic cavity operating at 12 GHz. This addition is necessary to improve both the driver-witness separation and its jitter in relation to the jitter from beamline components maintaining the energy jitter in the plasma stage below 1%. For the SPARC_LAB facility, the final focusing system, which relies on permanent quadrupoles, was evaluated to optimize the final focusing prior to plasma injection. Additionally, a comprehensive analysis of the comb working point was performed, employing a triplet of electromagnetic quadrupoles to achieve optimal beam matching. Building on the EuPRAXIA@SPARC_LAB injector baseline, the study investigated potential upgrades by transitioning from the existing S-band configuration to a C-band technology, which promises enhanced efficiency and performance. This technology offers several advantages, including higher efficiency, a reduced footprint, and the maintenance of high-brightness parameters. For this new layout, the feasibility of producing a comb electron beam with the necessary properties was initially assessed, followed by an optimization of the beam dynamics. Given the challenge of adequately separating the two beams to match the plasma density, a high-harmonic cavity at 36 GHz was introduced for the C-band configuration. Based on the results from the previous layout, this cavity was expected to provide improved separation. Indeed, the cavity proved essential in enhancing the beam dynam-

ics, specifically improving the emittance of the witness beam while maintaining its peak current, thereby preserving the final brightness. In addition, machine learning studies were conducted for the PEGASUS photogun. The developed algorithm showed satisfactory agreement with experimental measurements and was used to predict parameters such as MTE, which are often affected by multiple measurement uncertainties. These virtual diagnostic systems could be implemented in the future for comb applications, where low-energy measurements are typically challenging due to the beams' close proximity and strong interactions. For this photogun, characterization measurements were also carried out on various cathodes at different wavelengths to identify the best cathode for future applications at the facility and investigate the transition to the Yttrium cathode to achieve high repetition rate operation. Some open points remain from this study, which will be the focus of future investigations. For future studies, it will be essential to assess how transverse wakefields in the X-band cavity amplify trajectory jitter caused by laser pointing instability at the cathode. Understanding and addressing these effects will be critical to optimizing the performance of the whole injector. A complete stability study for the C-band injector similar to those conducted for the S-band. This step will allow us to determine definitively whether the proposed solution can be considered for a future upgrade of the machine. Additionally, the possibility of further optimizing the working point without relying on the high-harmonic cavity must be explored, considering the technological challenges not only in fabricating the cavity but also in sourcing the necessary power supplies. This point represents the greatest challenge in the development of this injector, given the even stricter need for the HHC after the Gun. Future perspectives also include the development of a photoemission model to analyze data collected from various cathodes at the PEGASUS beam line, to assess the actual benefits of each, with a particular focus on yttrium cathodes, which have theoretically numerous advantages as discussed.

Bibliography

[1] J. S. Fraser, R. L. Sheffield, E. R. Gray, and G. W. Rodenz. High-brightness photoemitier injector for electron accelerators. *IEEE Transactions on Nuclear Science*, 32(5):1791–1793, 1985.

[2] R. Pompili, M.P. Anania, M. Bellaveglia, A. Biagioni, S. Bini, F. Bisesto, E. Chiadroni, A. Cianchi, G. Costa, D. Di Giovenale, M. Ferrario, F. Filippi, A. Gallo, A. Giribono, V. Lollo, A. Marocchino, V. Martinelli, A. Mostacci, G. Di Pirro, S. Romeo, J. Scifo, V. Shpakov, C. Vaccarezza, F. Villa, and A. Zigler. Recent results at sparc_lab. *Nuclear Instruments and Methods in Physics Research Section A: Accelerators, Spectrometers, Detectors and Associated Equipment*, 909:139–144, 2018. 3rd European Advanced Accelerator Concepts workshop (EAAC2017).

[3] D. Alesini et al. Eupraxia@sparc_lab conceptual design report. National Institute of Nuclear Physics Frascati National Laboratory Report INFN-18-03/LNF, 5 2018.

[4] R. W Assmann et al. Eupraxia conceptual design report. *The European Physical Journal Special Topics*, 229:3675–4284, 12 2020.

[5] S. Telfer, S. Reiche, J.B. Rosenzweig, P. Frigola, and G. Andonian. Commissioning of the ucla pegasus photoinjector laboratory. In *PACS2001. Proceedings of the 2001 Particle Accelerator Conference (Cat. No.01CH37268)*, volume 3, pages 2263–2265 vol.3, 2001.

[6] M. Migliorati, A. Bacci, C. Benedetti, E. Chiadroni, M. Ferrario, A. Mostacci, L. Palumbo, A. R. Rossi, L. Serafini, and P. Antici. Intrinsic normalized emittance growth in laser-driven electron accelerators. *Phys. Rev. ST Accel. Beams*, 16:011302, Jan 2013.

[7] Christoph Bostedt, Sébastien Boutet, David M. Fritz, Zhirong Huang, Hae Ja Lee, Henrik T. Lemke, Aymeric Robert, William F. Schlotter, Joshua J. Turner, and Garth J. Williams. Linac coherent light source: The first five years. *Rev. Mod. Phys.*, 88:015007, Mar 2016.

[8] V. Ayvazyan, N. Baboi, I. Bohnet, R. Brinkmann, M. Castellano, P. Castro, L. Catani, S. Choroba, A. Cianchi, M. Dohlus, H. T. Edwards, B. Faatz, A. A. Fateev, J. Feldhaus, K. Flöttmann, A. Gamp, T. Garvey, H. Genz, Ch. Gerth, V. Gretchko, B. Grigoryan, U. Hahn, C. Hessler, K. Honkavaara, M. Hüning, R. Ischebeck, M. Jablonka, T. Kamps, M. Körfer, M. Krassilnikov, J. Krzywinski, M. Liepe, A. Liero, T. Limberg, H. Loos, M. Luong, C. Magne, J. Menzel, P. Michelato, M. Minty, U.-C. Müller, D. Nölle, A. Novokhatski, C. Pagani, F. Peters, J. Pflüger, P. Piot, L. Plucinski, K. Rehlich, I. Reyzl, A. Richter, J. Rossbach, E. L.

Saldin, W. Sandner, H. Schlarb, G. Schmidt, P. Schmüser, J. R. Schneider, E. A. Schneidmiller, H.-J. Schreiber, S. Schreiber, D. Sertore, S. Setzer, S. Simrock, R. Sobierajski, B. Sonntag, B. Steeg, F. Stephan, K. P. Sytchev, K. Tiedtke, M. Tonutti, R. Treusch, D. Trines, D. Türke, V. Verzilov, R. Wanzenberg, T. Weiland, H. Weise, M. Wendt, I. Will, S. Wolff, K. Wittenburg, M. V. Yurkov, and K. Zapfe. Generation of gw radiation pulses from a vuv free-electron laser operating in the femtosecond regime. *Phys. Rev. Lett.*, 88:104802, Feb 2002.

[9] D. Filippetto, P. Musumeci, R. K. Li, B. J. Siwick, M. R. Otto, M. Centurion, and J. P. F. Nunes. Ultrafast electron diffraction: Visualizing dynamic states of matter. *Rev. Mod. Phys.*, 94:045004, Dec 2022.

[10] P A Walker, P D Alesini, A S Alexandrova, M P Anania, N E Andreev, I Andriyash, A Aschikhin, R W Assmann, T Audet, A Bacci, I F Barna, A Beaton, A Beck, A Beluze, A Bernhard, S Bielawski, F G Bisesto, J Boedewadt, F Brandi, O Bringer, R Brinkmann, E Bründermann, M Büscher, M Bussmann, G C Bussolino, A Chance, J C Chanteloup, M Chen, E Chiadroni, A Cianchi, J Clarke, J Cole, M E Couprie, M Croia, B Cros, J Dale, G Dattoli, N Delerue, O Delferriere, P Delinikolas, J Dias, U Dorda, K Ertel, A Ferran Pousa, M Ferrario, F Filippi, J Fils, R Fiorito, R A Fonseca, M Galimberti, A Gallo, D Garzella, P Gastinel, D Giove, A Giribono, L A Gizzi, F J Grüner, A F Habib, L C Haefner, T Heinemann, B Hidding, B J Holzer, S M Hooker, T Hosokai, A Irman, D A Jaroszynski, S Jaster-Merz, C Joshi, M C Kaluza, M Kando, O S Karger, S Karsch, E Khazanov, D Khikhlukha, A Knetsch, D Kocon, P Koester, O Kononenko, G Korn, I Kostyukov, L Labate, C Lechner, W P Leemans, A Lehrach, F Y Li, X Li, V Libov, A Lifschitz, V Litvinenko, W Lu, A R Maier, V Malka, G G Manahan, S P D Mangles, B Marchetti, A Marocchino, A Martinez de la Ossa, J L Martins, F Massimo, F Mathieu, G Maynard, T J Mehrling, A Y Molodozhentsev, A Mosnier, A Mostacci, A S Mueller, Z Najmudin, P A P Nghiem, F Nguyen, P Niknejadi, J Osterhoff, D Papadopoulos, B Patrizi, R Pattathil, V Petrillo, M A Pocsai, K Poder, R Pompili, L Pribyl, D Pugacheva, S Romeo, A R Rossi, E Roussel, A A Sahai, P Scherkl, U Schramm, C B Schroeder, J Schwindling, J Scifo, L Serafini, Z M Sheng, L O Silva, T Silva, C Simon, U Sinha, A Specka, M J V Streeter, E N Svystun, D Symes, C Szwaj, G Tauscher, A G R Thomas, N Thompson, G Toci, P Tomassini, C Vaccarezza, M Vannini, J M Vieira, F Villa, C-G Wahlström, R Walczak, M K Weikum, C P Welsch, C Wiemann, J Wolfenden, G Xia, M Yabashi, L Yu, J Zhu, and A Zigler. Horizon 2020 eupraxia design study. *Journal of Physics: Conference Series*, 874(1):012029, jul 2017.

[11] Jana Schaber, Rong Xiang, and Nikolai Gaponik. Review of photocathodes for electron beam sources in particle accelerators. *J. Mater. Chem. C*, 11:3162–3179, 2023.

[12] David H. Dowell and John F. Schmerge. Quantum efficiency and thermal emittance of metal photocathodes. *Phys. Rev. ST Accel. Beams*, 12:074201, Jul 2009.

[13] David H. Dowell and John F. Schmerge. Quantum efficiency and thermal emittance of metal photocathodes. *Phys. Rev. ST Accel. Beams*, 12:074201, Jul 2009.

[14] Massimo Ferrario. Injection, Extraction and Matching. In *CAS - CERN Accelerator School 2019: High Gradient Wakefield Accelerators*, 7 2020.

[15] M. Ferrario. Space Charge Mitigation. *CERN Yellow Rep. School Proc.*, 5:89, 2018.

[16] Luca Serafini and James B. Rosenzweig. Envelope analysis of intense relativistic quasilaminar beams in rf photoinjectors:ma theory of emittance compensation. *Phys. Rev. E*, 55:7565–7590, Jun 1997.

[17] F. Lemery and P. Piot. Ballistic bunching of photoinjected electron bunches with dielectric-lined waveguides. *Phys. Rev. ST Accel. Beams*, 17:112804, Nov 2014.

[18] M. Ferrario et al. Experimental demonstration of emittance compensation with velocity bunching. *Phys. Rev. Lett.*, 104:054801, Feb 2010.

[19] L. Serafini and M. Ferrario. Velocity bunching in photo-injectors. *AIP Conference Proceedings*, 581(1):87–106, 2001.

[20] M. Ferrario et al. Experimental demonstration of emittance compensation with velocity bunching. *Phys. Rev. Lett.*, 104:054801, 2010.

[21] Klaus Floettmann. A space charge tracking code. `https://www.desy.de/~mpyflo/`.

[22] G. Campogiani, A. Giribono, S. Pioli, A. Mostacci, L. Palumbo, S. Guiducci, G. Di Pirro, A. Falone, C. Vaccarezza, A. Variola, S. Di Mitri, G. Gaio, J. Corbett, L. Sabato, P. Arpaia, and I. Chaikovska. Progress of the development of the eli-np gbs high level applications. *Nuclear Instruments and Methods in Physics Research Section A: Accelerators, Spectrometers, Detectors and Associated Equipment*, 909:327–331, November 2018.

[23] Cecile Limborg-Deprey. RF Design of the LCLS Gun. SLAC Nation Accelerator Laboratory Technical Note , LCLS-TN-05-3, 02 2005.

[24] S.H. Kong, J. Kinross-Wright, D.C. Nguyen, and R.L. Sheffield. Photocathodes for free electron lasers. *Nuclear Instruments and Methods in Physics Research Section A: Accelerators, Spectrometers, Detectors and Associated Equipment*, 358(1):272–275, 1995.

[25] Riccardo Pompili, D. Alesini, Maria Pia Anania, Mostafa Behtouei, M. Bellaveglia, Angelo Biagioni, Fabrizio Bisesto, M. Cesarini, Enrica Chiadroni, Alessandro Cianchi, Gemma Costa, Michele Croia, A. Dotto, D. Giovenale, Marco Diomede, F. Dipace, M. Ferrario, Anna Giribono, V. Lollo, and Arie Zigler. Energy spread minimization in a beam-driven plasma wakefield accelerator. *Nature Physics*, 17:1–5, 04 2021.

[26] S. Romeo, M. Ferrario, and A. R. Rossi. Beam loading assisted matching scheme for high quality plasma acceleration in linear regime. *Phys. Rev. Accel. Beams*, 23:071301, Jul 2020.

[27] M. Ferrario, D. Alesini, A. Bacci, M. Bellaveglia, R. Boni, M. Boscolo, P. Calvani, M. Castellano, E. Chiadroni, A. Cianchi, L. Cultrera, G. Di Pirro, L. Ficcadenti, D. Filippetto, A. Gallo, G. Gatti, L. Giannessi, M. Labat, S. Lupi, B. Marchetti, C. Marrelli, M. Migliorati, A. Mostacci, D. Nicoletti, E. Pace, L. Palumbo, V. Petrillo, M. Quattromini, C. Ronsivalle, A.R. Rossi, J. Rosenzweig, L. Serafini, M. Serluca, B. Spataro, H. Tomizawa, C. Vaccarezza, and C. Vicario. Laser comb with velocity bunching: Preliminary results at sparc. *Nuclear Instruments*

and Methods in Physics Research Section A: Accelerators, Spectrometers, Detectors and Associated Equipment, 637(1, Supplement):S43–S46, 2011. The International Workshop on Ultrashort Electron & Photon Beams: Techniques and Applications.

[28] Lixin Yan, Qiang Du, Yingchao Du, Jianfei Hua, Wenhui Huang, and Chuanxiang Tang. Uv pulse shaping for the photocathode rf gun. *Nuclear Instruments and Methods in Physics Research Section A: Accelerators, Spectrometers, Detectors and Associated Equipment*, 637(1, Supplement):S127–S129, 2011. The International Workshop on Ultra-short Electron & Photon Beams: Techniques and Applications.

[29] F. Villa, M.P. Anania, M. Bellaveglia, F. Bisesto, E. Chiadroni, A. Cianchi, A. Curcio, M. Galletti, D. Di Giovenale, G. Di Pirro, M. Ferrario, G. Gatti, M. Moreno, M. Petrarca, R. Pompili, and C. Vaccarezza. Laser pulse shaping for high gradient accelerators. *Nuclear Instruments and Methods in Physics Research Section A: Accelerators, Spectrometers, Detectors and Associated Equipment*, 829:446–451, 2016. 2nd European Advanced Accelerator Concepts Workshop - EAAC 2015.

[30] G J Silvi, A L Bacci, M Carillo, E Chiadroni, L Faillace, D Francescone, A Giribono, P Iovine, A Mostacci, M Ferrario, R Pompili, and C Vaccarezza. Beam dynamics optimization of eupraxia@sparc_lab rf injector. *Journal of Physics: Conference Series*, 2687(6):062024, jan 2024.

[31] A. Giribono et al. Electron beam analysis and sensitivity studies for the EuPRAXIA@SPARC_LAB RF injector. In *Proc. IPAC'23*, number 14 in International Particle Accelerator Conference, pages 2034–2037. JACoW Publishing, Geneva, Switzerland, 9 2023.

[32] L M Young and Billen J. The particle tracking code parmela. In *Proceedings of the 2003 Particle Accelerator Conference*, 2003.

[33] Alberto Bacci, Vittoria Petrillo, and Marcello Rossetti Conti. GIOTTO: A Genetic Code for Demanding Beam-dynamics Optimizations. In *7th International Particle Accelerator Conference*, pages 3073–3076, 2016.

[34] A. Mostacci et al. Advanced Beam Manipulation Techniques at SPARC. In *Proc. IPAC'11*, number 2 in International Particle Accelerator Conference, pages 2877–2881. JACoW Publishing, Geneva, Switzerland, 9 2011.

[35] Chandrashekhar Joshi. Plasma accelerators. *Scientific American*, 294(2):40–47, 2006.

[36] Anna Giribono et al. EuPRAXIA@SPARC_LAB: the high-brightness RF photo-injector layout proposal. *Nuclear Instruments and Methods in Physics Research Section A: Accelerators, Spectrometers, Detectors and Associated Equipment*, 909, 02 2018.

[37] A. Marocchino, F. Massimo, A.R. Rossi, E. Chiadroni, and M. Ferrario. Efficient modeling of plasma wakefield acceleration in quasi-non-linear-regimes with the hybrid code architect. *Nuclear Instruments and Methods in Physics Research Section A: Accelerators, Spectrometers, Detectors and Associated Equipment*, 829:386–391, 2016. 2nd European Advanced Accelerator Concepts Workshop - EAAC 2015.

[38] S. Romeo et al. Numerical studies for eupraxia@sparc_lab plasma beam driven working point. In *Proc. IPAC'23*, number 14 in IPAC'23 - 14th International Particle Accelerator Conference, pages 2042–2045. JACoW Publishing, Geneva, Switzerland, 05 2023.

[39] G Giannetti, M P Anania, M Bellaveglia, E Chiadroni, A Cianchi, A Del Dotto, M Galletti, A Gallo, A Giribono, L Piersanti, R Pompili, S Romeo, B Serenellini, S Tocci, C Vaccarezza, F Villa, and M Ferrario. Experimental and numerical characterization of timing jitter for short electron beams in a linear photo-injector. *Measurement Science and Technology*, 35(2):025015, nov 2023.

[40] F. Demurtas et al. Experimental characterization of the timing-jitter effects on a beam-driven plasma wakefield accelerator. In *Proc. 15th International Particle Accelerator Conference*, number 15 in IPAC'24 - 15th International Particle Accelerator Conference, pages 553–556. JACoW Publishing, Geneva, Switzerland, 05 2024.

[41] Riccardo Pompili, Alessandro Cianchi, D. Alesini, Maria Pia Anania, Bacci Alberto, M. Bellaveglia, Michele Castellano, Enrica Chiadroni, D. Giovenale, Giampiero Di Pirro, G. Gatti, Flavio Giorgianni, Massimo Ferrario, S. Lupi, Francesco Massimo, Andrea Mostacci, Andrea Rossi, Cristina Vaccarezza, and Fabio Villa. First single-shot and non-intercepting longitudinal bunch diagnostics for comb-like beam by means of electro-optic sampling. *Nuclear Instruments and Methods in Physics Research Section A Accelerators Spectrometers Detectors and Associated Equipment*, 740, 02 2014.

[42] E. Chiadroni et al. Status of Plasma-Based Experiments at the SPARC_LAB Test Facility. In *Proc. 9th International Particle Accelerator Conference (IPAC'18), Vancouver, BC, Canada, April 29-May 4, 2018*, number 9 in International Particle Accelerator Conference, pages 603–606, Geneva, Switzerland, June 2018. JACoW Publishing. https://doi.org/10.18429/JACoW-IPAC2018-TUXGBE3.

[43] R. Pompili, A. Cianchi, D. Alesini, M.P. Anania, A. Bacci, M. Bellaveglia, M. Castellano, E. Chiadroni, D. Di Giovenale, G. Di Pirro, G. Gatti, F. Giorgianni, M. Ferrario, S. Lupi, F. Massimo, A. Mostacci, A.R. Rossi, C. Vaccarezza, and F. Villa. First single-shot and non-intercepting longitudinal bunch diagnostics for comb-like beam by means of electro-optic sampling. *Nuclear Instruments and Methods in Physics Research Section A: Accelerators, Spectrometers, Detectors and Associated Equipment*, 740:216–221, 2014. Proceedings of the first European Advanced Accelerator Concepts Workshop 2013.

[44] A Biagioni, M P Anania, S Arjmand, E Behar, G Costa, A Del Dotto, M Ferrario, M Galletti, V Lollo, D Pellegrini, G Di Pirro, R Pompili, Y Raz, G Russo, and A Zigler. Gas-filled capillary-discharge stabilization for plasma-based accelerators by means of a laser pulse. *Plasma Physics and Controlled Fusion*, 63(11):115013, oct 2021.

[45] A. Bacci, L. Faillace, and M. Rossetti Conti. Extreme High Brightness Electron Beam Generation in a Space Charge Regime. In *Proc. 29th Linear Accelerator Conference (LINAC'18), Beijing, China, 16-21 September 2018*, number 29 in Linear Accelerator Conference, pages 314–319, Geneva, Switzerland, Jan. 2019. JACoW Publishing. https://doi.org/10.18429/JACoW-LINAC2018-TU1P01.

[46] A. Gallo et al. Study of a C-band Harmonic RF System to Optimize the RF Bunch Compression Process of the SPARC Beam. In *Proc. 6th International Particle Accelerator Conference (IPAC'15), Richmond, VA, USA, May 3-8, 2015*, number 6 in International Particle Accelerator Conference, pages 1552–1555, Geneva, Switzerland, June 2015. JACoW. https://doi.org/10.18429/JACoW-IPAC2015-TUPWA058.

[47] Paul Emma. X-Band RF harmonic compensation for linear bunch compression in the LCLS. SLAC Nation Accelerator Laboratory Technical Note SLAC-TN-05-004, LCLS-TN-01-1, 11 2001.

[48] Lucia Sabbatini et al. SABINA: A Research Infrastructure at LNF. In *12th International Particle Accelerator Conference* , 8 2021.

[49] R Pompili et al. Energy spread minimization in a beam-driven plasma wakefield accelerator. *Nature Physics*, 17(4):499–503, 2021.

[50] R Pompili et al. Free-electron lasing with compact beam-driven plasma wakefield accelerator. *Nature*, 605(7911):659–662, 2022.

[51] E. Chiadroni, M. Bellaveglia, P. Calvani, M. Castellano, L. Catani, A. Cianchi, G. Di Pirro, M. Ferrario, G. Gatti, O. Limaj, S. Lupi, B. Marchetti, A. Mostacci, E. Pace, L. Palumbo, C. Ronsivalle, R. Pompili, and C. Vaccarezza. Characterization of the THz radiation source at the Frascati linear accelerator. *Review of Scientific Instruments*, 84(2):022703, 02 2013.

[52] Andrea Frazzitta, Alberto Bacci, Arianna Carbone, Alessandro Cianchi, Alessandro Curcio, Illya Drebot, Massimo Ferrario, Vittoria Petrillo, Marcello Rossetti Conti, Sanae Samsam, Luca Serafini, and Andrea Renato Rossi. First simulations for the euaps betatron radiation source: A dedicated radiation calculation code. *Instruments*, 7(4), 2023.

[53] D Alesini, S Bertolucci, ME Biagini, C Biscari, R Boni, M Boscolo, M Castellano, A Clozza, G Di Pirro, A Drago, et al. The sparc project: a high-brightness electron beam source at lnf to drive a sase-fel experiment. *Nuclear Instruments and Methods A*, 507(1–2):345 – 349, 2003.

[54] FG Bisesto, MP Anania, M Bellaveglia, E Chiadroni, A Cianchi, G Costa, A Curcio, D Di Giovenale, G Di Pirro, M Ferrario, et al. The flame laser at sparc_lab. *Nuclear Instruments and Methods in Physics Research Section A: Accelerators, Spectrometers, Detectors and Associated Equipment*, 909:452–455, 2018.

[55] Enrica Chiadroni, Alessandro Cianchi, Massimo Ferrario, Andrea Mostacci, Riccardo Pompili, and Vladimir Shpakov. A versatile thz source from high-brightness electron beams: Generation and characterization. *Condensed Matter*, 5(2):40, 2020.

[56] V Shpakov, D Alesini, MP Anania, M Behtouei, B Buonomo, M Bellaveglia, A Biagioni, F Cardelli, M Carillo, E Chiadroni, et al. Design, optimization and experimental characterization of rf injectors for high brightness electron beams and plasma acceleration. *Journal of Instrumentation*, 17(12):P12022, 2022.

[57] M. Ferrario et al. Experimental demonstration of emittance compensation with velocity bunching. *Physical review letters*, 104(5):054801, 2010.

[58] R. Pompili, M. P. Anania, E. Chiadroni, A. Cianchi, M. Ferrario, V. Lollo, A. Notargiacomo, L. Picardi, C. Ronsivalle, J. B. Rosenzweig, V. Shpakov, and A. Vannozzi. Compact and tunable focusing device for plasma wakefield acceleration. *Review of Scientific Instruments*, 89(3):033302, 03 2018.

[59] Wencheng Fang, Qiang Gu, Xing Sheng, Chaopeng Wang, Dechun Tong, Lifang Chen, Shaopeng Zhong, Jianhao Tan, Guoqiang Lin, Zhihao Chen, and Zhentang Zhao. Design, fabrication and first beam tests of the c-band rf acceleration unit at sinap. *Nuclear Instruments and Methods in Physics Research Section A: Accelerators, Spectrometers, Detectors and Associated Equipment*, 823:91–97, 2016.

[60] D. Alesini, A. Bacci, M. Bellaveglia, R. Boni, G. Di Pirro, M. Ferrario, L. Ficcadenti, A. Gallo, F. Marcellini, Andrea Mostacci, E. Pace, B. Spataro, C. Vaccarezza, C. Ronsivalle, Luigi Palumbo, and V. Spizzo. Beam energy upgrade of the frascati fel linac with a c-band rf system. In *Proceedings of the 1st International Particle Accelerator Conference, IPAC 2010*, pages 3682–3684. Printed Edition, 2010. Presented at the 1st International Particle Accelerator Conference, IPAC 2010, Kyoto, 23 May 2010 through 28 May 2010.

[61] J. Rosenzweig and E. Colby. Charge and wavelength scaling of RF photoinjector designs. *AIP Conference Proceedings*, 335(1):724–737, 06 1995.

[62] A. Giribono, D. Alesini, F. Cardelli, G. Di Raddo, L. Faillace, M. Ferrario, A. Gallo, A. Gizzi, S. Lauciani, A. Liedl, L. Pellegrino, L. Piersanti, C. Vaccarezza, A. Vannozzi, J. Scifo, L. Ficcadenti, G. Castorina, G. Pedrocchi, G. J. Silvi, and T. G. Lucas. Dynamics studies of high brightness electron beams in a normal conducting, high repetition rate *c*-band injector. *Phys. Rev. Accel. Beams*, 26:083402, Aug 2023.

[63] D. Alesini et al. Design, realization and high power RF test of the new brazed free C band photo-gun. In *Proc. IPAC'24*, number 15 in International Particle Accelerator Conference, pages 2929–2932. JACoW Publishing, Geneva, Switzerland, 7 2024.

[64] M Croia, D Alesini, F Cardelli, M Diomede, M Ferrario, A Giribono, S Romeo, C Vaccarezza, and A Vannozzi. High gradient ultra-high brightness c-band photoinjector optimization. *Journal of Physics: Conference Series*, 1596(1):012031, jul 2020.

[65] G Castorina, L Ficcadenti, M Migliorati, A Mostacci, L Palumbo, F Cardelli, G Franzini, A Marcelli, B Spataro, G Sorbello, L Celona, S Gammino, G Torrisi, A Cahill, J Rosenzweig, and V A Dolgashev. A tm01 mode launcher with quadrupole field components cancellation for high brightness applications. *Journal of Physics: Conference Series*, 1067(8):082025, sep 2018.

[66] A. Giribono, D. Alesini, F. Cardelli, G. Castorina, G. Di Raddo, M. Ferrario, L. Ficcadenti, A. Gallo, G. Muti, G. Pedrocchi, J. Scifo, C. Vaccarezza, and A. Vannozzi. Effects of Mode Launcher on Beam Dynamics in Next Generation High Brightness C-Band Guns. In *Proc. IPAC'21*, number 12 in International Particle Accelerator Conference, pages 813–816. JACoW Publishing, Geneva, Switzerland, 08 2021. https://doi.org/10.18429/JACoW-IPAC2021-MOPAB257.

[67] G. D'Auria et al. The CompactLight Design Study Project. In *Proc. 10th International Particle Accelerator Conference (IPAC'19), Melbourne, Australia, 19-24 May 2019*, number 10 in International Particle Accelerator Conference, pages 1756–1759, Geneva, Switzerland, Jun. 2019. JACoW Publishing. https://doi.org/10.18429/JACoW-IPAC2019-TUPRB032.

[68] L. Piersanti et al. RF power station stabilization techniques and measurements at LNF-INFN. In *Proc. IPAC'24*, number 15 in International Particle Accelerator Conference, pages 1417–1420. JACoW Publishing, Geneva, Switzerland, 7 2024.

[69] Luca Piersanti, Marco Bellaveglia, Fabio Cardelli, Alessandro Gallo, Riccardo Magnanimi, Sergio Quaglia, Michele Scampati, Giorgio Scarselletta, Beatrice Serenellini, and Simone Tocci. Design and test of a klystron intra-pulse phase feedback system for electron linear accelerators. *Photonics*, 11(5), 2024.

[70] Mostafa Behtouei, Luigi Faillace, Spataro Bruno, A. Variola, and Mauro Migliorati. A sw ka-band linearizer structure with minimum surface electric field for the compact light xls project. *Nuclear Instruments and Methods in Physics Research Section A Accelerators Spectrometers Detectors and Associated Equipment*, 984:164653, 09 2020.

[71] J. Scifo, M. Behtouei, L. Faillace, M. Ferrario, A. Giribono, M. Migliorati, B. Spataro, G. Torrisi, and C. Vaccarezza. Beam Dynamics Studies in a Standing Wave Ka-band Linearizer. In *Proc. IPAC'21*, number 12 in International Particle Accelerator Conference, pages 857–859. JACoW Publishing, Geneva, Switzerland, 08 2021. https://doi.org/10.18429/JACoW-IPAC2021-MOPAB270.

[72] A. Castilla, R. Apsimon, G. Burt, X. Wu, A. Latina, X. Liu, I. Syratchev, W. Wuensch, B. Spataro, and A. W. Cross. Ka-band linearizer structure studies for a compact light source. *Phys. Rev. Accel. Beams*, 25:112001, Nov 2022.

[73] J. Scifo, A. Lorusso, E. Chiadroni, P. Cinquegrana, S. Dabagov, M. Danailov, A. Demidovich, M. Ferrario, D. Garzella, A. Giribono, D. Hampai, A. Perrone, and M. Trovò. Photoemission studies of yttrium photocathodes by using the visible radiation. *Phys. Rev. Accel. Beams*, 23:123401, Dec 2020.

[74] Jonathan Goodman and Jonathan Weare. Ensemble samplers with affine invariance. *Communications in Applied Mathematics and Computational Science*, 5(1):65–80, 2010. Publisher Copyright: © 2010 by Mathematical Sciences Publishers.

[75] Siddhartha Chib and Edward Greenberg. Understanding the metropolis-hastings algorithm. *The American Statistician*, 49(4):327–335, 1995.

[76] Daniel Foreman-Mackey, David W. Hogg, Dustin Lang, and Jonathan Goodman. emcee: The mcmc hammer. *Publications of the Astronomical Society of the Pacific*, 125(925):306, feb 2013.

[77] David Alesini, Antonio Battisti, Massimo Ferrario, Luca Foggetta, Valerio Lollo, Luca Ficcadenti, Valerio Pettinacci, Sean Custodio, Eylene Pirez, Pietro Musumeci, and Luigi Palumbo. New technology based on clamping for high gradient radio frequency photogun. *Phys. Rev. ST Accel. Beams*, 18:092001, Sep 2015.

[78] F. Cropp, L. Moos, A. Scheinker, A. Gilardi, D. Wang, S. Paiagua, C. Serrano, P. Musumeci, and D. Filippetto. Virtual-diagnostic-based time stamping for ultrafast electron diffraction. *Phys. Rev. Accel. Beams*, 26:052801, May 2023.

[79] Jessica Scifo, D. Alesini, Maria Pia Anania, M. Bellaveglia, Stefano Bellucci, Angelo Biagioni, Fabrizio Bisesto, Fabio Cardelli, Enrica Chiadroni, Alessandro Cianchi, Gemma Costa, D. Giovenale, Giampiero Di Pirro, R. Raddo, D. Dowell, Massimo Ferrario, Anna Giribono, Alice Lorusso, Federico Micciulla, and Fabio Villa. Nano-machining, surface analysis and emittance measurements of a copper photocathode at sparc_lab. *Nuclear Instruments and Methods in Physics Research Section A: Accelerators, Spectrometers, Detectors and Associated Equipment*, 909, 01 2018.

[80] Bas van der Geer. General particle tracer: A 3d code for accelerator and beam line design.

[81] Auralee Edelen, Nicole Neveu, Matthias Frey, Yannick Huber, Christopher Mayes, and Andreas Adelmann. Machine learning for orders of magnitude speedup in multiobjective optimization of particle accelerator systems. *Physical Review Accelerators and Beams*, 23(4):044601, 2020.

[82] Stephen P. Brooks and Andrew Gelman. General methods for monitoring convergence of iterative simulations. *Journal of Computational and Graphical Statistics*, 7(4):434–455, 1998.

[83] Andrew Gelman and Donald B. Rubin. Inference from Iterative Simulation Using Multiple Sequences. *Statistical Science*, 7(4):457 – 472, 1992.

[84] Bradley Efron, Trevor Hastie, Iain Johnstone, and Robert Tibshirani. Least angle regression. *The Annals of Statistics*, 32(2):407 – 499, 2004.

[85] Frederick William Cropp V. *High-Performance Accelerator Modeling: Toward Improving Controls and Diagnostics for High-Brightness Beams in Experiment.* PhD thesis, UCLA, Los Angeles (main), UCLA, 2023.

[86] A. H. Sommer. New Photoemissive Cathodes of High Sensitivity. *Review of Scientific Instruments*, 26(7):725–726, 07 1955.

[87] W. E. Spicer. Photoemissive, photoconductive, and optical absorption studies of alkali-antimony compounds. *Phys. Rev.*, 112:114–122, Oct 1958.

[88] L. Cultrera, S. Karkare, B. Lillard, A. Bartnik, I. Bazarov, B. Dunham, W. Schaff, and K. Smolenski. Growth and characterization of rugged sodium potassium antimonide photocathodes for high brilliance photoinjector. *Applied Physics Letters*, 103(10):103504, 09 2013.

[89] D. G. Fisher, A. F. McDonie, and A. H. Sommer. Band-bending effects in Na2KSb and K2CsSb photocathodes. *Journal of Applied Physics*, 45(1):487–488, 01 1974.

[90] Jared Maxson, Luca Cultrera, Colwyn Gulliford, and Ivan Bazarov. Measurement of the tradeoff between intrinsic emittance and quantum efficiency from a NaKSb photocathode near threshold. *Applied Physics Letters*, 106(23):234102, 06 2015.

[91] Lee A. DuBridge. A further experimental test of fowler's theory of photoelectric emission. *Phys. Rev.*, 39:108–118, Jan 1932.

[92] N. Shafqat et al. Commissioning of S-band Cavity Test Facility at Elettra for Conditioning of High Gradient Structures for the Fermi Linac Upgrade. In *Proc. 10th International Particle Accelerator Conference (IPAC'19), Melbourne, Australia, 19-24 May 2019*, number 10 in International Particle Accelerator Conference, pages 2846–2848, Geneva, Switzerland, Jun. 2019. JACoW Publishing. https://doi.org/10.18429/JACoW-IPAC2019-WEPRB021.

[93] Carlo Vicario, Simona Bettoni, Bolko Beutner, Marta Divall, E. Prat, Thomas Schietinger, A. Trisorio, and Christoph Hauri. Photocathode laser wavelength-tuning for thermal emittance and quantum efficiency studies. *FEL 2013: Proceedings of the 35th International Free-Electron Laser Conference*, pages 434–437, 01 2013.

[94] Michael Borland. User's manual for elegant. 10 2002.

[95] Tobias Persson, Helmut Burkhardt, Riccardo De Maria, Laurent Deniau, Eirik Høydalsvik, Andrea Latina, Piotr Skowroński, Rogelio Tomás García, and Léon van Riesen-Haupt. MAD-X for Future Accelerators. *JACoW*, IPAC2022:1858–1861, 2022.

[96] E. Esarey, C. B. Schroeder, and W. P. Leemans. Physics of laser-driven plasma-based electron accelerators. *Rev. Mod. Phys.*, 81:1229–1285, Aug 2009.

[97] J. B. Rosenzweig, B. Breizman, T. Katsouleas, and J. J. Su. Acceleration and focusing of electrons in two-dimensional nonlinear plasma wake fields. *Phys. Rev. A*, 44:R6189–R6192, Nov 1991.

[98] W. Lu, C. Huang, M. Zhou, W. B. Mori, and T. Katsouleas. Nonlinear theory for relativistic plasma wakefields in the blowout regime. *Phys. Rev. Lett.*, 96:165002, Apr 2006.

List of Figures

List of Tables

Appendix A

Beam dynamics simulations tools

While simple matrix-based calculations for particle accelerators, are useful in low-charge, straightforward, linear environments, these models tend to diverge from reality when nonlinear effects are present. For instance, in a space charge dominated regime, standard transfer matrices fail to predict the proper beam evolution because they neglect space charge effects. Similarly, higher-order nonlinearities, such as aberrations in magnetic electron lenses, are also ignored. Although higher-order transport tensors or linearized space charge matrices can be defined, calculating higher-order effects quickly becomes computationally challenging. Over the past decades, the increase in computational power, along with advancements in software, has provided the fields of accelerator physics and engineering with numerous sophisticated simulations and mathematical models. Modern modeling tools for particle accelerators are more accurate, versatile, and faster than ever before. These tools often utilize the following techniques:

- Advanced matrix-based codes: These use an approach similar to the aforementioned simple calculations but include higher-order effects.
- Particle tracking codes: These calculate the trajectories of particles in the electric and magnetic fields of an accelerator at each step.
- Particle-in-cell codes: These model the interaction of particles with electromagnetic fields, which are self-consistently calculated by solving Maxwell's equations for any geometry and medium.

Example codes include ELEGANT [94], MAD-X[95], ASTRA [21], Tstep [32], and General Particle Tracer [80]. In general, mathematical models that employ simplifications, such as linear transfer matrix models, execute quickly with modern computing power. However, the fidelity of these models to real beam-line behavior may degrade in the presence of nonlinear effects. On the other hand, computational models, while highly accurate, are often too slow for online operation, particularly when optimization is involved. Even offline, optimization problems can become computationally intensive, especially as the number of optimization parameters increases. The beam dynamics simulation tools used for this study are ASTRA and General Particle Tracer (GPT). The Astra (A Space Charge Tracking Algorithm) program package consists of the four parts:

- The program generator which may be used to generate an initial particle distribution.

- The program Astra which tracks the particles under the influence of external and internal fields.
- The graphic program fieldplot which is used to display electromagnetic fields of beam line elements and space charge fields of particle distributions.
- The graphic program postpro which is used to display phase space plots of particle distributions and allows a detailed analysis of the phase space distribution.
- The graphic program lineplot, which is used to display the beam size, emittance, bunch length etc. versus the longitudinal beam line position or versus a scanned parameter, respectively.

Astra is written in Fortran 90 and runs on different platforms. The main development platforms are LINUX and Windows. Using the elements available in this simulation code, a model of the accelerator can be created and its dynamics recalculated. The following discussion will describe how the various elements of the beamline were defined and how elements that the code has available were used to proceed with beam dynamics studies. The main parts that have been used for the study of electron beam dynamics are the Astra and Generated executables. A Matlab code written specifically for the case was created for the analysis of the results. In choosing among the various simulated codes available, the astra code was selected because besides further optimization studies, we take advantage of its interaction with the GIOTTO algorithm [33]. GIOTTO is a software based on a Genetic Algorithm (GA). When the parameters defining an acceleration machine beamline are strongly correlated non-linearly, GAs are a powerful tool to address these complexities. Such conditions typically arise due to space-charge effects, as seen in high-brightness e-beam photo-injectors. Let us now go ahead and describe how the injector elements, introduced in the previous chapter, are defined in ASTRA. The main elements of an injector are:

- gun
- gun solenoid
- linac booster

The generator program is used to generate the initial particle distribution. Within the input file the longitudinal, transverse distribution of the beam and the distribution the energy is defined. Other parameters such as, charge, spot size, length and initial energy are defined in the same file. Refer to the code manual for more in-depth information. The beamline is defined in another file that will then be recalled in the astra program. Each element is called with a specific namelist. For the gun and the booster sections, the &CAVITY namelist is used. In this section of the input the field map, the peak accelerating field in MV/m, the number of cells (in case of traveling wave structure), and the phase and frequency of the accelerating structure must be specified. An example of how these elements are defined is called in Fig A.1. Solenoids can also be defined with appropriate namelist, &SOLENOID. In this case, the peak magnetic field value, field map, and, corresponding center should be specified. In the input file can also be choose the types of output you want to obtain as well as the space charge routine, the manipulations you want to make on the initial distribution, and add whatever elements you want, e.g., quadrupoles and dipole. Again to go into detail, please refer to the manual. In the course of doctoral work, the code has been modeled to deal

with different situations, and in the following sections the versatility in dealing with any problem related to the dynamics of electron beams will be shown. So far this is a general description, as we analyze specific cases we will go into the details of the operations to be performed to correctly simulate each situation. General Particle Tracer (GPT), is a versatile and comprehensive simulation

```
&CAVITY
LOOP=F,
LEFIELD=T,
FILE_EFIELD='pmefield_David_ASTRA.txt','TWS_Xband.dat',4*'TWS_sparc_v2.dat'
NUE=2.856,11.424,4*2.856,
MAXE=120.000000,0.0,2.67E+01  , 2.10E+01  ,  25, 45.5,                !2.6924E+01
PHI(1)= 220.56 ,0,  38.07 , -66.43  ,  52.540,    112.150,          !66.8   !-11.582 !2.95397E+00  !-1.10
C_POS=0.00000000,1.25,1.44980800000,5.048808,7.552486,10.05616,
!C_POS=0.00000000,1.25,1.545979,5.028979,7.532695,10.036373,
C_NUMB=0,9,84,3*57,
/
!4.98494533
&SOLENOID
LOOP=F,
LBFIELD=T,
FILE_BFIELD='SOLENOID_A_3000G_2D_POISSON_ASTRA.txt','SABINA_TW.poi','SABINA_TW_2m.txt'
MAXB=0.2999 ,   0.0310  ,  0.0740,
!MAXB=0.3242 ,   0.0390  ,  0.0980/0.0920,
S_POS=0.20400000,2.9856,6.08494533,
/
```

Figure A.1: example of astra input file.

software used primarily in the field of accelerator physics. It is designed to model and analyze the behavior of charged particles in electromagnetic fields. Over the past decade, GPT has become a trusted tool in accelerator and beam-line design. Built on advanced 3D particle-tracking algorithms, it provides a robust platform for analyzing both linear and non-linear effects in charged-particle dynamics. A fifth-order Runge-Kutta driver with adaptive step-size control ensures high accuracy while minimizing computation time. GPT offers various space-charge models, from simplified 1D interactions to fully 3D point-to-point calculations, and includes representations of most standard beam-line components A.2. The GPT package includes the main executable for calculations, along with a suite of pre- and post-processing tools for data analysis and a graphical user interface for ease of use.

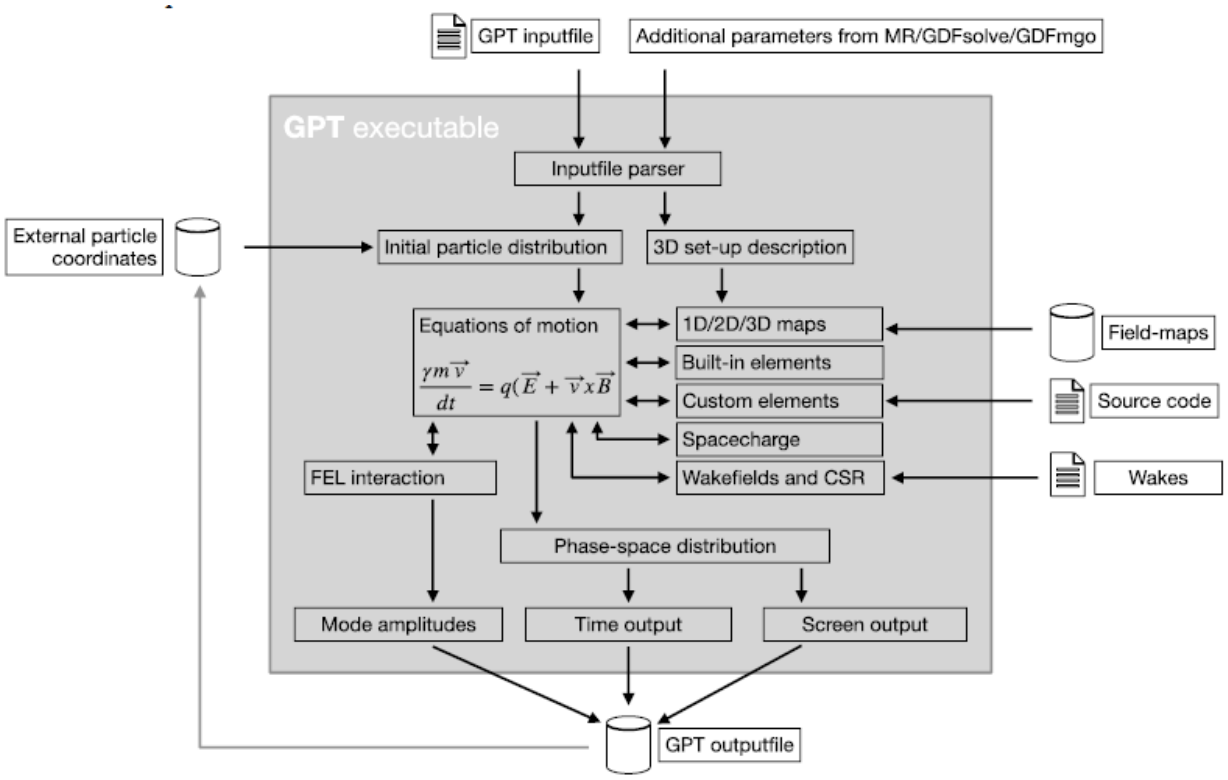

Figure A.2: GPT work space.

Appendix B

Matching conditions in plasma

We introduce a simplified model for the plasma and the resulting fields acting on the beam, allowing us to write an envelope equation for the accelerated beam [14]. In this section, we are interested in the case of external injection of particles into a plasma wave, in the so-called "bubble" regime, which can be excited by a short, intense laser pulse [96] or by a driving electron beam [97] with beam density n_b close to the plasma density n_0, such that $n_b > n_0$. With a highly simplified model of the plasma behind the driving pulse we consider a uniform, spherical ion distribution with particle density n_0. This model is justified by the fact that, in this regime, the fields are linear in both longitudinal and transverse directions—at least in the region of interest for particle acceleration, where the fields produced by a uniform ion distribution within a sphere of radius $R_{\text{sphere}} \approx \lambda_p/2$ resemble those produced by a real plasma. Here, $\lambda_p = 2\pi c\sqrt{\frac{\varepsilon_0 m_e}{(n_0 e^2)}}$ is the plasma wavelength. The field produced by the ions and experienced by a witness electron beam is purely electrostatic since the ions remain stationary in the laboratory frame on the relevant time scales. This field can be expressed as:

$$E_r = \frac{en_0}{3\varepsilon_0} r \tag{B.1}$$

where E_r exhibits radial symmetry. Some authors, e.g., [97], alternatively consider a uniform cylindrical column of ions producing a transverse field of the form $E_r = \frac{en_0}{2\varepsilon_0} r$. Due to the collective oscillation of plasma electrons, the ion sphere "virtually" moves along z at the speed β_d of the driving pulse, even though the source of the field remains stationary in the laboratory frame. Magnetic fields are also generated by the plasma electron displacement, but these fields have a negligible net effect on a relativistic beam, as shown in [98]. The accelerating field component increases linearly from the moving sphere center $z_c = \beta_d ct$:

$$E_z(\zeta) = \frac{en_0}{3\varepsilon_0}\zeta \tag{B.2}$$

where $\zeta = z - z_c$, with a maximum at the sphere edge $\zeta = \frac{\lambda_p}{2}$. The energy gained by a witness electron is given by $\gamma = \gamma_0 + \alpha L_{acc}$, where L_{acc} represents the acceleration length within the plasma, and $\alpha(\zeta) = \frac{eE_z(\zeta)}{mc^2} = \frac{1}{3}\left(\frac{2\pi c}{\lambda_p}\right)^2 \zeta$ is the normalized accelerating gradient. The energy spread accumulated by a finite-length bunch is then:

$$\frac{\delta\gamma}{\gamma} = \frac{\delta\alpha L_{acc}}{\gamma_0 + \alpha L_{acc}} \approx \frac{\delta\alpha}{\alpha} = \frac{\sigma_z}{\lambda_p} \tag{B.3}$$

which implies that ultra-short electron bunches are required to maintain the energy spread below 1%. This simplified model does not account for beam loading effects or beam slippage relative to the driving pulse. The transverse (focusing) field experienced at a distance x from the propagation axis is given by:

$$E_x = \frac{en_0}{3\varepsilon_0}x \tag{B.4}$$

This field is independent of ζ, and thus does not typically induce correlated emittance growth due to ion focusing. As shown, plasma fields require precise matching conditions to avoid emittance growth during propagation. The transverse beam dynamics can be described through the following envelope equation:

$$\ddot{\sigma}_x + \frac{\dot{\gamma}}{\gamma}\dot{\sigma}_x + \frac{k_p^2}{3\gamma}\sigma_x = \frac{\epsilon_n^2}{\gamma^2\sigma_x^3} + \frac{k_{0,sc}}{\gamma^3\sigma_x} \tag{B.5}$$

where $k_p = \sqrt{\frac{n_0 e^2}{\varepsilon_0 mc^2}}$ is the plasma wave number. An equilibrium solution for this equation has yet to be found, although simplifications allow for an approximate matching condition. Here, there are two focusing terms—the adiabatic damping and the ion focusing—and two defocusing terms, the emittance pressure and space charge effects. To compare the relative significance of the first two terms, we rewrite the previous equation using a transformed variable $\tilde{\sigma}_x = \gamma\sigma_x$, yielding:

$$\ddot{\tilde{\sigma}}_x + \left(\left(\frac{\dot{\gamma}}{2\gamma}\right)^2 + \frac{k_p^2}{3\gamma}\right)\tilde{\sigma}_x = \frac{\epsilon_n^2}{\tilde{\sigma}_x^3} + \frac{k_{0,sc}}{\gamma^3\tilde{\sigma}_x} \tag{B.6}$$

The beam is space-charge dominated when $\rho = \frac{k_{0,sc}\tilde{\sigma}_x^2}{\epsilon_n^2\gamma^2} \gg 1$, and ion-focusing dominated when $\eta = \frac{4\gamma k_p^2}{3\dot{\gamma}^2} \gg 1$. For typical parameters of a plasma accelerator— kA peak current, 1 µm normalized emittance, injection energy $\gamma_0 = 300$, and beam size of about 3 µm—we find $\rho < 1$ and $\eta > 1$. Consequently, the envelope equation can be reasonably approximated by:

$$\ddot{\sigma}_x + \frac{k_p^2}{3\gamma}\sigma_x = \frac{\epsilon_n^2}{\gamma^2\sigma_x^3} \tag{B.7}$$

where $\gamma(z) = \gamma_0 + \alpha z$. Seeking a particular solution of the form $\sigma_x = \gamma^{-1/4}\sigma_0$, we obtain:

$$\sigma_0 = \sqrt{\frac{\sqrt{2}\epsilon_n}{k_p}} \tag{B.8}$$

yielding the beam-plasma matching condition:

$$\sigma_x = \gamma^{-1/4}\sigma_0 = \sqrt[4]{\frac{2}{\gamma}}\sqrt{\frac{\epsilon_n}{k_p}} \tag{B.9}$$

Notice that the beam undergoes focusing as γ increases, with the beam density increasing and causing a significant perturbation of the plasma fields. One possible solution to mitigate this effect is to vary the plasma density along the channel, maintaining a constant beam envelope. It is interesting to consider the effect of a plasma density profile that decreases according to $n(z) = \frac{\gamma_0}{\gamma(z)}n_0$, leading to $k_p^2 = \frac{e^2 n_0}{\varepsilon_0 mc^2}\frac{\gamma_0}{\gamma} = \frac{\gamma_0}{\gamma}k_{p,0}^2$. In this case, the envelope equation (58) without space charge effects

becomes:

$$\ddot{\sigma}_x + \frac{\dot{\gamma}}{\gamma}\dot{\sigma}_x + \frac{\gamma_0 k_{p,0}^2}{3\gamma^2}\sigma_x = \frac{\epsilon_n^2}{\gamma^2\sigma_x^3} \tag{B.10}$$

which admits a constant equilibrium solution:

$$\sigma_x = \sqrt[4]{\frac{2}{\gamma_0}}\sqrt{\frac{\epsilon_n}{k_{0,p}}} \tag{B.11}$$

On the other hand, before injection into the plasma accelerator, the beam must be focused to the matching spot given by (64) to prevent envelope oscillations that may cause emittance growth and enhanced betatron radiation emission. It has been proposed to shape the plasma density profile to gently capture the beam using the increasing ion focusing effect. For example, by varying the plasma density as $n(z) = \frac{\gamma(z)}{\gamma_0} n_0$ at the entrance of the plasma column, the envelope equation (58) can be written as:

$$\ddot{\sigma}_x + \frac{k_{p,0}^2}{3\gamma_0}\sigma_x = \frac{\epsilon_n^2}{\gamma^2\sigma_x^3} \tag{B.12}$$

with $k_p^2 = \frac{e^2 n_0}{\varepsilon_0 mc^2}\frac{\gamma}{\gamma_0} = \frac{\gamma}{\gamma_0}k_{p,0}^2$. This equation has a particular solution assuming that $\ddot{\gamma}$ is negligible:

$$\sigma_x = \sqrt[4]{2\gamma_0}\sqrt{\frac{\epsilon_n}{\gamma k_{p,0}}} \tag{B.13}$$

showing that with a proper choice of initial plasma density, the beam envelope can be gently matched to the accelerating plasma channel.